

636242.
3182922
TR diss 2609

**TR diss
2609**

**Crosswell Seismic
Tomography and Migration**

Proefschrift

ter verkrijging van de graad van doctor
aan de Technische Universiteit Delft,
op gezag van de Rector Magnificus,
Prof. ir. K.F. Wakker
in het openbaar te verdedigen
ten overstaan van een commissie,
door het College van Dekanen aangewezen,
op woensdag 13 september 1995 te 16:00 uur
door

Erwin Johannes Martinus GILING

natuurkundig ingenieur
geboren te Den Burg, Texel



Dit proefschrift is goedgekeurd door de promotor:

Prof. dr. ir. A. J. Berkhout

Toegevoegd promotor:

Dr. ir. C. P. A. Wapenaar

Promotiecommissie:

Prof. dr. ir. H. Blok (*TU-Delft, Electrotechniek*)

Prof. dr. ir. J. T. Fokkema (*TU-Delft, Mijnbouwkunde*)

Prof. ir. M. Peeters (*TU-Delft, Mijnbouwkunde*)

Dr. ir. A. J. W. Duijndam (*TU-Delft, Mijnbouwkunde*)

Dr. ir. G. Blacquière (*Technisch Fysische Dienst TNO TU-Delft*)

Copyright ©1995, by E. J. M. Giling, TNO Institute of Applied Physics, Delft, The Netherlands.

All rights reserved. No part of this publication may be reproduced, stored in a retrieval system or transmitted in any form or by any means, electronic, mechanical, photocopying, recording or otherwise, without the prior written permission of the author E. J. M. Giling, TNO Institute of Applied Physics, P.O. Box 155, 2600 AD Delft, The Netherlands.

CIP-DATA KONINKLIJKE BIBLIOTHEEK, DEN HAAG

Giling, Erwin Johannes Martinus

Crosswell seismic tomography and migration / Erwin

Johannes Martinus Giling. - [S.l. : s.n.]. - III.

Thesis Technische Universiteit Delft. - With ref. - With
summary in Dutch.

ISBN 90-9008620-X

Subject headings: seismology / tomography / wave
propagation.

SUPPORT

The research for this thesis has been financially supported by TNO Insitute of Applied Physics.

Typesetting system: L^AT_EX2e

Cover: "Modeled P- (front) and S- (back) snapshots of crosswell elastic waves."

Printed in The Netherlands by: Delft University Press.

aan mijn Ouders



Contents

1	Introduction	1
1.1	The seismic method	1
1.1.1	Probing the earth	1
1.1.2	A classification of seismic methods	1
1.2	Crosswell seismic profiling	5
1.2.1	Introduction	5
1.2.2	Field application examples	6
1.2.3	Properties and representation of crosswell data	6
1.2.4	The inverse problem: extracting the information	9
1.3	Objectives of this thesis	12
2	Macro model estimation	15
2.1	Introduction	15
2.2	The principles of general iterative nonlinear inversion	16
2.2.1	Problem formulation	16
2.2.2	Methods for minimization	19
2.2.3	Statistical inversion: the Bayesian approach	22
2.2.4	Concluding remarks on nonlinear inversion	27
2.3	Traditional cell-based travelttime tomography	28
2.3.1	Nonlinear cell-based travelttime inversion	28
2.3.2	Linear Bayesian inversion	32
2.3.3	Inversion examples for linear cell models	33

2.4	Sparse macro velocity model based traveltine tomography	38
2.4.1	Forward macro model representation	39
2.4.2	Ray-tracing	40
2.4.3	Nonlinear optimization and inversion	42
2.4.4	Nonlinear model driven inversion examples	42
3	Crosswell migration using wavefield extrapolation	47
3.1	Representation of crosswell seismic data	47
3.1.1	Conceptual model	47
3.1.2	One-way wave equation	48
3.1.3	One-way representation	51
3.1.4	Practical aspects of the representation	55
3.1.5	Matrix notation	56
3.2	The inverse problem: practical implementation of crosswell migration	57
3.2.1	Migration of surface data revisited	58
3.2.2	Conventional crosswell migration approach	60
3.2.3	Alternative approach to crosswell migration	63
3.2.4	Implementation of the deconvolution step	65
3.2.5	Steep-dip example	67
3.3	Spatial resolution - surface data versus crosswell data	68
3.4	Illumination aspects	73
3.5	Concluding remarks	76
4	Synthetic data examples	79
4.1	Horizontally layered medium	79
4.1.1	Model and acquisition	79
4.1.2	Pre-processing	81
4.1.3	Migration	83
4.2	AMOCO synthetic data set	86
4.2.1	Model and acquisition	87
4.2.2	Pre-processing	87

4.2.3 Migration	89
5 Field data example	95
5.1 Data acquisition	95
5.2 Pre-processing	97
5.3 Macro model estimation	100
5.4 Migration	101
5.5 Discussion of the results	106
A Pre-processing of crosswell data	109
A.1 Sources of noise	109
A.2 Approach taken in this thesis	110
A.2.1 Energy balancing	110
A.2.2 The picking problem	112
A.2.3 Direct wave removal	112
B The common focus point concept	113
B.1 Crosswell migration by double focussing	113
B.2 Examples	115
B.3 Concluding remarks	119
Bibliography	120
Acknowledgments	127
Summary	129
Samenvatting	131
Curriculum vitae	135

Chapter 1

Introduction

1.1 The seismic method

1.1.1 Probing the earth

Since the beginning of the 20th century, the interest in the earth's interior has been increased significantly. In the relatively shallow part of the earth's crust, down to a few kilometers, hydrocarbons such as coal, oil and gas can be found, on which our current society heavily depends. Also, knowledge about the crust itself, of which the thickness ranges between 8 to 45 kilometers, is an important source in the prediction of earthquakes. Currently, there is only one method that is used to explore the earth from its shallowest layers to the core itself: *the seismic method*.

The seismic method uses elastic waves to probe the subsurface. These waves are *emitted* into the earth by a seismic source, after which they *propagate* to receivers, where they are detected. During their propagation, the waves *interact* with inhomogeneities which may cause reflections and scattering. Thus, the detected waves contain *information* about the earth along the path the waves have traveled. The main objective of the seismic method is to extract this information from the seismic measurements and to present it in terms of geological structure and material properties.

1.1.2 A classification of seismic methods

An important characteristic of seismic wave propagation is that waves with higher frequencies carry information on finer subsurface details than waves with lower frequencies. Therefore, it is always attempted to use frequencies as high as possible. We also know that in the earth higher frequency waves are more attenuated than lower frequency waves. Generalizing, this means that if the distance over which the waves travel is decreased, higher frequencies may be used. Following Berkhout (1984b), on the basis of signal bandwidth, and thus on resolution and the length of the wave propagation paths, a classification between different seismic methods can be

made. In this thesis we will mainly focus on the methods that are of importance to the oil and gas industry. An indication of the frequency bands used in the discussed methods is depicted in Figure 1.1.

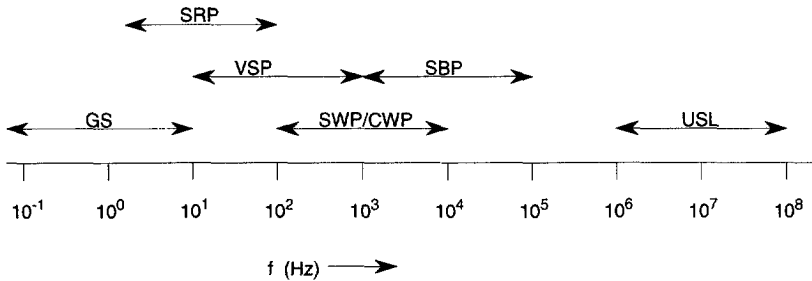


Fig. 1.1 The approximate frequency bands used in seismology methods. GS: global seismology, SRP: surface reflection profiling, VSP: vertical seismic profiling, SWP: single-well profiling, CWP: crosswell profiling, SBP: (sub) bottom profiling. USL: ultrasonic logging.

Global seismology

The science that is involved in the investigation of the deep parts of the earth using seismic waves is called *global seismology*, *whole-earth seismology* or *deep-earth seismology*. For the generation of seismic waves, the method depends on natural phenomena like earthquakes. Earthquakes are able to produce the large amount of seismic energy necessary to successfully detect the waves after they have traveled, for example, through the core of the earth. Because of the large distances involved, these seismic waves have a low frequency content (up to about 10 Hz). Deep-earth seismology is not particularly useful for the oil and gas industry, so it will not be discussed further. The reason to mention global seismology here is that some solution methods developed in this field are also useful to other seismic methods (see e.g. Nolet (1987)).

Seismic exploration

The class of seismology methods using seismic waves to investigate the more shallow part of the earth's crust (say up to 5 kilometers) is called *seismic exploration*. For the oil and gas industry, which is of primary interest in this thesis, the main goal of seismic exploration is to find new hydrocarbon reservoirs and to accurately map existing reserves. In seismic exploration artificial sources are used, which convert electrical, chemical or mechanical energy into seismic waves: explosive sources, vibrators or piezo-electric transducers. In the most popular seismic exploration technique both sources and detectors are placed near or at the surface, at land or in marine environments. This is referred to as *surface reflection profiling* (SRP), or the *surface seismic reflection method*.

Figure 1.2 shows an artist's impression of the acquisition of SRP data on land. In essence the

seismic waves are *emitted* into the subsurface, they *propagate downward* and then *reflect* on layer boundaries. Next, these reflected waves *propagate upward* and are *detected* by geophones at the surface, yielding recorded seismic signals. From these signals, properties of the subsurface can be extracted by using dedicated seismic processing techniques. Note that both the horizontal and vertical distance in the figure may in practice span several kilometers. A typical signal frequency range that is used is 10 to 100 Hz, where waves reflected on the deeper layers exhibit lower frequency content than waves reflected in the more shallow parts of the subsurface, because they traveled over larger distances. In land data the presence of a weathered top layer is a limiting factor. Weathered soil attenuates the high frequencies more than consolidated rock.

If we want to know more about a potential reservoir, the next obvious step is to drill a hole and investigate it from nearby. The existence of a borehole allows the seismic method to be applied with sources or detectors *in* the borehole, such that extra information can be obtained in the neighborhood of the borehole, particularly in the *target zone*. The target zone is the area where oil and gas reservoirs are found or expected to exist. Although seismic techniques that employ sources or receivers in boreholes are commonly captured under the heading seismic *exploration*, in general their goal is to help the reservoir engineers in monitoring and mapping *existing* reservoirs. Thus, we could refer to the following three seismic methods as “reservoir seismology”, considering it to be a subset of seismic exploration.

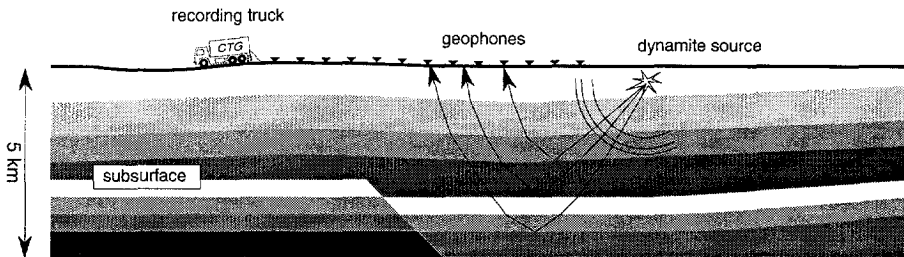


Fig. 1.2 Artist's impression of seismic surface data acquisition on land: emission, downward propagation, reflection, upward propagation and detection.

Vertical seismic profiling

Vertical seismic profiling (VSP) is a technique where sources are placed at the surface and receivers in a borehole. The sources may be buried beneath the weathered layer and the receivers may be relatively well coupled to the surrounding formation. This configuration allows for higher frequencies to be used, say up to 1 kHz, again depending on the distances involved. A complementary configuration is obtained by placing the sources in the well and receivers at the surface, called *reverse-VSP* (RVSP).

Single well profiling

It is also possible to place both sources and receivers in the borehole, called *single well profiling* or *borehole reflection profiling*. For the near-borehole area this technique actually is called "sonic logging", with a frequency band of about 5-15 kHz. For the application of profiling the near-borehole area over larger distances (say up to 100 m) this is an emerging technique, for which some practical problems are not fully solved yet. If we want to have independent source and receiver positions, two devices must be lowered and positioned in one narrow borehole at the same time. Furthermore, special tools must be developed, because the usual sources easily excite the so called "tube-wave", which is a relatively strong wave that travels up and down in fluid-filled boreholes. The tube-wave may totally mask the reflected seismic waves coming in from outside the borehole. Recent developments are, however, promising. Chen and Miller (1994) report a new borehole tool which uses a frequency band of 200 Hz-1.5 kHz.

Crosswell seismic profiling

In areas with more than one borehole available, it is possible to put the sources into one borehole, and the receivers into another. This configuration, which is the main topic of this thesis, is called *crosswell seismic profiling* or *crosswell seismology*¹. As both sources and receivers can be positioned near the target zone and beneath the attenuating shallow section, it is possible to use relatively high frequencies. Seismic waves with frequencies up to several kHz can successfully be detected. Again this depends on the distance between the boreholes, which usually measures in the order of 100 m, and the local geology. For smaller distances, a maximum frequency of several kHz is feasible, in highly ideal areas the use of frequencies up to 10 kHz has been reported. Crosswell seismic profiling will be further discussed in section 1.2, below.

Sub-bottom and ear-surface profiling

To measure the depth of the sea-floor and characterize its shallow layers, called (*sub*)-*bottom profiling*, sonar-like methods can be used. These employ a frequency range from 1 kHz up to 100 kHz. In seismic exploration, sonar-like tools have also been successfully applied to near-surface seismic profiling on land. The near-surface is however not of primary interest to the oil and gas industry.

Ultrasonic logging

Ultrasonic logging and inspection methods are used to image the relatively near borehole region, and to inspect borehole walls (e.g. *sonic logging*). The length of the propagation paths are relatively small. Frequencies up to 10 MHz may be used, yielding highly detailed information. The elastic waves are generated and detected by ultrasound transducers, which may be positioned in a reflection or in a transmission configuration. Note that the former resembles the

¹Equivalent but less used terms are "well-to-well", "borehole-to-borehole" and "cross-borehole" seismology.

surface seismic reflection situation, while the latter has similarities with the crosswell method.

1.2 Crosswell seismic profiling

1.2.1 Introduction

We will now focus on the main subject of this thesis: *crosswell seismic profiling*. However, as most exploration geophysicists are more familiar with the properties of surface seismic data, comparisons with the surface seismic situation will be made where appropriate throughout this thesis.

Because of the potential to get high resolution information from the target zone, crosswell seismic profiling is of special interest to reservoir geophysicists. In addition, there are applications in the fields of geotechnical and civil engineering, and mining. If there are two adjacent boreholes available, crosswell seismic profiling can be attempted. The information that can be obtained are estimates on parameters like wave propagation velocity, attenuation, acoustic impedance and Poisson's ratio. Furthermore, structural information can be obtained such as the position of faults and lithological boundaries.

The first crosswell measurements with the objective to get information on the interwell space were carried out in the early 1960's. Geyer (1993) revisits a survey conducted in 1961, where analogue processing techniques were used. In the early 1970's Bois et al. (1972) carried out crosswell experiments to obtain the velocity structure between two wells. With the increasing price-performance ratio of digital computers in the 1980's, crosswell inversion methods took off and peaked in the first years of the 1990's. Currently, the interest in crosswell applications has decreased somewhat, because of the high expenses involved. The main disadvantage of crosswell surveying are the high costs of shutting down one or two producing wells to conduct a crosswell survey. However, it is expected that when oil production in marginal fields becomes more attractive, the use of special techniques like enhanced oil recovery (EOR) will become more popular. Especially for EOR programs crosswell seismic profiling can be an important tool.

In the remainder of this section crosswell seismic profiling will be illustrated by presenting some field applications as found in the geophysical literature. Then, we will look in more detail at the properties and information content of crosswell data. Using these properties, the different approaches to crosswell parameter estimation and inversion ("extracting the information") will be discussed briefly.

Note that there is a vast amount of literature available on the theory and application of crosswell seismic profiling. In this thesis it is attempted to give the most relevant references; the bibliography list is not claimed to be complete.

1.2.2 Field application examples

Over the last 15 years, a number of field experiments have been conducted that show the potential and importance of crosswell surveying for reservoir characterization and other engineering applications. In this section the most important applications of crosswell seismology are addressed and some references are given. Note that many case studies have only been presented at geophysical meetings; they have never officially been published.

A major application is the detection and mapping of faults and fracture zones, which is important with respect to fluid flow in a reservoir (Wong et al. (1987), Harris et al. (1990), Tura et al. (1992, 1994)). In the field of (atomic) waste disposal, the presence of fractured rock is also important and can be investigated by crosswell surveying (Wong et al. (1983), Bregman et al. (1989a), Jung et al. (1991)).

For enhanced oil recovery (EOR) projects, crosswell seismic profiling has successfully been used to monitor the propagation of flood fronts. By repeating the experiments, the propagation of the flood front can even be monitored over time (Bregman et al. (1989b), Justice (1989), Brzostowski and McMechan (1991), Paulsson et al. (1992), Justice et al. (1993), Wilt et al. (1994)).

With crosswell analysis, the near surface velocity is studied in order to improve the quality of surface seismic experiments (e.g. Lines and LaFehr (1989)).

Application of crosswell seismology in (coal) mining can assist in the mapping of existing reserves. Furthermore, mapping of geological structures such as faults and cavities may assist in improving the safety in mining (Hawkins et al. (1982), Cotten and Geldmacher (1990), Findlay et al. (1991), Friedel et al. (1992)).

In addition, several other more general case studies can be found in recent literature with applications to reservoir characterization and monitoring (Shima and Imamura (1991), Harris et al. (1992), Parra and Bangs (1992), Pratt et al. (1992), Justice et al. (1992), Lazaratos et al. (1993), Vassiliou et al. (1994a), among others).

1.2.3 Properties and representation of crosswell data

This thesis focuses on the inverse problem, which aims at the estimation of the subsurface parameters from measured crosswell seismic data. But, in order to establish a suitable representation from which to obtain an inversion scheme, we first have to fully understand the characteristics of crosswell acquisition, crosswell wave propagation, and scattering.

At the left of Figure 1.3 a crosswell acquisition experiment is visualized. At the right, an example of a crosswell (synthetic) seismic shot record is shown. Using this figure, the most important aspects of crosswell data will now briefly be discussed. Again, note the scale of the crosswell experiment. In Figure 1.3, the width and depth are in the order of a few hundred meters, while for surface seismic profiling (Figure 1.2), the width and depth may be in the order of several

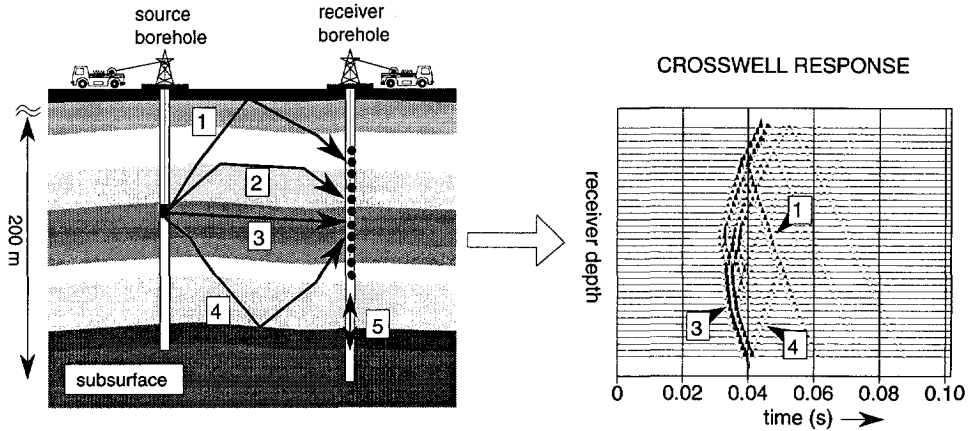


Fig. 1.3 Left: Artist's impression of crosswell seismic data acquisition and wave propagation. Right: Example of crosswell seismic signals. The main events are indicated. For further explanation, see text.

kilometers.

The source

As shown in Figure 1.3 a downhole seismic source, which emits seismic energy into the subsurface, is lowered into the left borehole. In the industry, a number of source types are used, which can be categorized into *impulsive* sources and *controlled frequency* sources. In general, both pressure waves (P) and shear waves (S) are induced into the formation. A desirable property of the emitted source wavefield is that it is the same over all shots (repeatability). In this respect, the coupling of the source with the surrounding medium is an important issue. Commonly the source is considered to be a point source, but in some situations tube waves may exist in the source borehole that re-emit seismic energy into the subsurface away from the source, causing a complex radiation pattern. Interface waves, propagating on the boundary of the casing and the surrounding medium or borehole fluid, are another cause of non-localized sources of seismic energy. In this thesis the assumption of point sources is adopted. Further discussion of the source properties are beyond the scope of this thesis. An overview on downhole seismic sources and their properties can, for example, be found in Hardage (1992).

Wave propagation and scattering

Although the emitted wavefields are full elastic, which means that for example P reflections, S reflections, and P-S converted waves may exist, in this thesis the focus is on the scalar (acoustic) representation of the crosswell wavefield. With the proper sources and receivers, in some ideal cases both the primary P and S wavefields can be taken into account. Because of the crosswell

acquisition configuration, these wavefields may be separable by applying a simple time window (Pratt and Gouly (1991), Hardage (1992-page 20), Lazaratos et al. (1994)). In comparison, for surface data the S reflections from shallow reflectors are likely to coincide with the P reflections from deeper layers. After separation of the crosswell data into P and S waves, it is possible to treat both wave types separately, using a scalar representation. When using a non-clamped impulsive type of source in a fluid-filled borehole, the P wavefield plays a more important role than the S wavefield. In such cases, the S wavefield may be neglected altogether.

At the left of Figure 1.3, the most important wave-types and their corresponding paths are indicated. From top to bottom:

- (1) reflected waves (up-down)
- (2) refracted waves (head-waves) and interface waves
- (3) direct waves
- (4) reflected waves (down-up)
- (5) tube waves in the receiver borehole

In addition, detailed scattering of waves may take place, defined as the interaction of waves with inhomogeneities smaller than the wavelength. The wavepaths for scattered waves are comparable with (1) and (4). Note that in (elastic) wave theory, "reflection" is commonly encompassed by the term "scattering". An important property of crosswell profiling is that, in contrary to the surface seismic method, primary waves may reflect both "down-up" and "up-down" at each interface.

At the right of Figure 1.3, an example of a crosswell shot record is shown. The most important waves, which are the direct wave (3) and the primary reflected waves (1,4), are indicated. Actually, this modeled shot record contains P waves only, and no tube waves. Note the relatively strong amplitude of the direct wave.

In general, crosswell acquisition is performed with near vertical boreholes in a near horizontally layered medium. This causes high-angle ("striking") reflected waves. Post-critical angle dependent reflection effects are thus more likely to exist in crosswell situations than for surface seismic profiling. In thin low-velocity layers such as coal seams, guided wave events may be present. In some cases, these guided waves may even be used to check for crosswell continuity (Krohn (1992)).

Anisotropy is more important for crosswell wave propagation than it is for surface reflection wave propagation. Even if the constituents of the subsurface itself are not inherently anisotropic, waves that travel parallel to a pack of thin layers may exhibit different net wave propagation velocities than waves that travel more perpendicular to the layers. Another important source of anisotropy is cracked rock, which is often found in reservoirs (Crampin (1984), Lou and Crampin (1993)). A number of authors have confirmed the presence of anisotropy in certain crosswell datasets (e.g. Vassiliou et al. (1994b), Harris et al. (1994)) and others derived cross-

well processing schemes to take anisotropy into account (Carrion et al. (1992), Lines (1992), Michelena et al. (1993), Pratt et al. (1993)). But introducing anisotropy into the representation of crosswell wave propagation means that more parameters are needed. It is possible that the effects of anisotropy are relatively small. In that case, with respect to a possible “anisotropic inversion” scheme, the maximum overall accuracy on the estimated parameters is decreased (Lines (1992)). In this thesis, the effects of anisotropic wave propagation are not explicitly taken into account. In Chapter 5, the presence of anisotropy in a real crosswell dataset will be addressed.

The receivers

In the receiver borehole, the waves are detected by an array of receivers. These may be simple hydrophones, or (clamped) multi-component devices. A desirable characteristic for downhole receivers is the insensitivity to tube-waves induced in the receiver borehole. These tube-waves are commonly observed in crosswell datasets. In this thesis it is assumed that the receivers are point receivers.

Geometry issues

In the case of two vertical boreholes in a 2D inhomogeneous subsurface, the waves travel along the vertical plane spanned by the boreholes if the subsurface is invariant along the direction perpendicular to this plane. Thus a 2D slice of the earth is sampled. If the subsurface is truly 3D inhomogeneous, out of plane reflected and scattered waves are likely to exist. Using only two boreholes, there is no way of knowing exactly how the waves have traveled through the subsurface. This is an inherent limitation of crosswell techniques. In certain situations, the interpretation of the data may be incorrect due to out of plane wave propagation effects (e.g. Mufti (1992)). In addition, the boreholes may also deviate from the assumed vertical, while accurate measures on the exact position of sources and receivers are not always available. Note the correspondence with the surface statics problem. Bregman et al. (1989a) have tried to estimate the borehole deviations from the data itself. To eliminate some uncertainty, it is possible to acquire data using more than two boreholes. However, compared to the possible 3D surface seismic coverage, crosswell data acquisition is far more constrained. In this thesis the 2D situation with two vertical boreholes is assumed.

1.2.4 The inverse problem: extracting the information

In this section a concise overview on different approaches to crosswell parameter estimation and inversion is presented.

Tomography and inversion

The word tomography has its origins in the Greek word “tome”, meaning “cut” or “slice”. Tomography literally means “graphing” (imaging) by constructing slices of an object. Tomogra-

phy methods originate from the medical practice, where “computerized tomography” (CT) is used to image slices of the human body using X-ray attenuation, nuclear resonance or ultrasound (see e.g. Kak (1979)). Tomography encompasses a range of inversion methods that use a line integral through an object over a certain parameter to explain the data.

In seismic crosswell tomography, two subsets of the data are used separately: the direct wave and the scattered waves. The amplitude of the direct wave yields information on the attenuation, the phase of the direct wave yields information on the propagation velocity. In particular, the first arrival *traveltime* is often used. A tomographic problem is obtained by expressing traveltimes as the integral over the slowness ($1/\text{velocity}$) along the ray-paths that connect sources and receivers. The measured traveltimes are used to obtain an estimate on (slowness) parameters by using traveltime inversion. This *traveltime tomography* method has become very popular for the inversion of crosswell seismic traveltime data. For a comprehensive overview on approaches to traveltime tomography see Worthington (1984).

Traveltime tomography uses ray-theory, which is a high frequency approximation. This limits the resolution that can be obtained (Lo et al. (1988), Williamson (1991)). The problems of non-uniqueness, nonlinearity and computational efficiency are inherent to traveltime tomography, and a number of different approaches have been taken. This resulted in the development and application of a range of algorithms which combine fast and stabilized matrix inversion solvers with fast forward ray-tracers (Dines and Lytle (1979), Bregman et al. (1989a), Berryman (1990), Phillips and Fehler (1991)). Traveltime tomography will be further discussed in Chapter 2.

A main disadvantage of traveltime tomography is its low resolution. By using methods that employ the second subset of the crosswell data, namely the scattered waves, higher resolution images of the interwell space can be obtained². In the 1980s, so called “filtered diffraction tomography” was introduced (Devaney (1982, 1984)). Diffraction tomography aims at solving for the wave propagation velocities using the scattered waves. It is based on a back-propagation of wavefields into the subsurface, using the “Fourier diffraction” theorem. Algorithms for surface, VSP and crosswell data have been developed (Wu and Toksoz (1987), Harris (1987)). The main advantage of diffraction tomography algorithms is that they are computationally fast, as the discrete fast Fourier transform can be utilized. The main disadvantage of these algorithms is that a constant background model is assumed. Only a first order perturbation from that background is computed using a Born or Rytov approximation. Experiments have been carried out to validate the Born and Rytov assumptions, using synthetic and ultrasonic data (e.g. Pratt and Worthington (1988)). It is now common knowledge that the constant background assumption certainly holds for weak contrasts, which are present in medical X-ray tomography and medical ultrasonic diffraction tomography, but yields unsatisfactory results when applied to seismic

²In fact, the traveltime of scattered waves could also be picked and used in a traveltime inversion procedure, but this approach is more commonly found in surface data applications (Bishop et al. (1985), Chiu and Stewart (1987)).

data.

The difference between tomographic imaging and inversion is not a strict one. Some inversion methods which do also yield estimates of the velocity distribution and adopt high frequency approximations, could be referred to as “tomographic”. With the use of the term “tomography” for the inversion of reflected and scattered waves, the meaning of “tomography” is stretched beyond that of its original meaning: the inversion of (X-ray, seismic) *transmission* measurements. Summarized: tomography is an inversion technique, and seismic inversion methods yielding (velocity) images of the subsurface may be called tomographic.

Migration

Migration originally means the construction of an image of the earth by moving reflections to their correct position. Traditionally, migration was performed graphically, by hand, later evolving into digital methods like the diffraction stack, which is now called the classical migration approach. For a comprehensive discussion on a generalization of the classical diffraction stack, and synthetic examples for both surface, borehole and combined data see Miller et al. (1987). Claerbout (1971) introduced the concepts of (inverse) wave propagation and the zero-time imaging condition. Berkhout and Van Wulfften Palthe (1979) introduced migration in terms of spatial deconvolution, showing migration as a process to improve the spatial resolution by zero phasing. Since then, new migration techniques have been developed using forward and inverse wave extrapolation based on the wave equation. Contrary to tomography or inversion, migration aims at resolving the *reflectivity* of the subsurface. For a comparison of migration and inversion see Berkhout (1984a) and Wapenaar (1995a).

Wave equation migration methods can be divided into two categories. The first approach uses the *two-way* wave equation (e.g. Beylkin (1985), Bleistein (1987)). Migration techniques under this approach are commonly called “Kirchhoff migration”. For application of Kirchhoff migration in the crosswell seismic context see Findlay et al. (1991), Gray and Lines (1992). In two-way techniques, the resolved angle dependent reflectivity depends on the acquisition geometry. In the second approach, which will be adopted in this thesis, *one-way* wave theory is used, as introduced by Claerbout (1971). Berkhout (1982) derived a wave-equation migration approach based on one-way wave theory. In this approach migration is defined as a process to estimate reflectivity by removing propagation effects (up and down). Furthermore, angle dependent reflectivity is defined as an *intrinsic* medium property, which is independent of the acquisition geometry, such in contrast to the two-way techniques. For a comparison of two-way and one-way approaches, see Wapenaar (1993). In Chapter 3 of this thesis, one-way wave theory is extended to the crosswell transmission situation.

Another approach to crosswell wave equation migration is “reverse time migration”, in which wavefields are extrapolated using two-way finite-difference techniques. For crosswell applications see Hu et al. (1988), Zhu and McMechan (1988). This being a two-way technique too, this

method is not further discussed here.

Stacking methods

An often used method for crosswell wavefield imaging is an adaption of the VSP-CDP (vertical seismic profile to common depth point) mapping method. It is not a tomographic nor a migration method, but based on standard VSP stacking techniques. These are related to the NMO (normal moveout) + CDP stacking methods used for surface data processing. For crosswell purposes, the name XSP-CDP (crosswell seismic profile to common depth point) mapping has been proposed. The algorithm maps every data point to a possible reflection point based on reflection point locations and traveltimes calculated by ray-tracing. The disadvantages of the method are that a horizontally layered medium is assumed, and the amplitudes of the reflected waves are not properly taken into account. For a description of the method see Stewart (1991), a case study using XSP-CDP mapping as the primary imaging tool is presented by Lazaratos et al. (1993).

Combining traveltome tomography with migration

Wave-equation based migration methods need a *macro velocity model*. The macro velocity model describes the *trend* of the velocity distribution. As has already been indicated above, traveltome tomography using direct wave traveltimes yields a low resolution result. But, for the macro velocity model we do not need fine details. Thus, the macro velocity model can conveniently be estimated using traveltome tomography techniques. Finally, the migration step will resolve the *detail* of the subsurface.

Comparing again surface data processing with crosswell processing, it must be realized that the crosswell macro velocity model may contain more detail than a final migrated section obtained from surface data. In this thesis, the term "macro velocity model" refers to the *crosswell* case, and must not be confused with the surface data macro velocity model.

1.3 Objectives of this thesis

For the processing of surface seismic data, the following three steps are used. These steps are equally applicable to crosswell data:

- (1) pre-processing
- (2) reflectivity imaging
- (3) a. structural interpretation
 b. lithologic characterization

In the pre-processing step (1) the noise in the data is suppressed. This includes data not properly accounted for in later steps and effects such as irregular source and receiver coupling. Then, the

data is processed (2), and an image of the subsurface is obtained in terms of reflectivity. From this image, structural features can be identified, such as the position of reflectors and faults (3a). Finally, using both structural information and the amplitudes of imaged events (i.e. angle dependent reflectivity), a lithologic characterization of the subsurface is obtained (3b), for example in terms of rock and pore parameters.

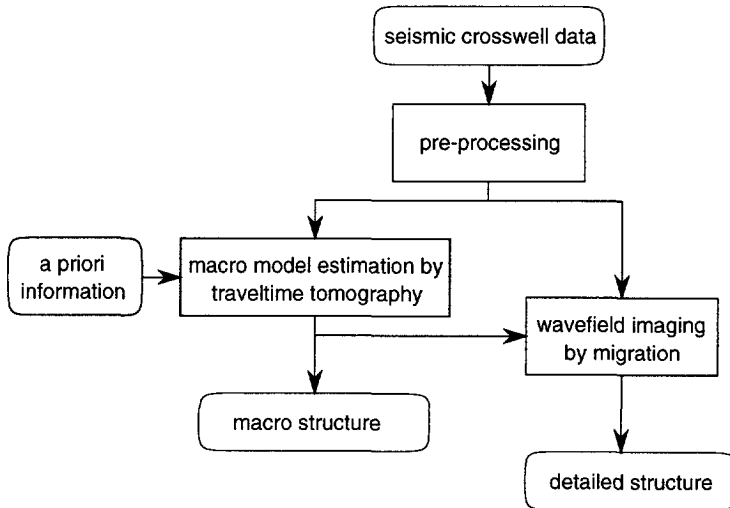


Fig. 1.4 The approach to crosswell seismic processing taken in this thesis

This thesis focuses on the third step. The primary objective of this thesis is *to develop an improved processing scheme for the transformation of crosswell seismic data into a structural model of the subsurface.*

A two-step approach is taken, consisting of *macro velocity model estimation* (presented in Chapter 2) followed by *migration* (presented in Chapter 3). This is visualized in Figure 1.4. For the macro model estimation step a nonlinear travelttime inversion method is proposed. To obtain an accurate macro velocity model, it is important to use all a priori knowledge that is available. This includes information from well-logs, geology, and surface seismic exploration experiments. Therefore, a Bayesian approach is taken, which integrates a priori information into the inversion in a statistically justified way. Furthermore, an important choice is how to parameterize the forward model. In Chapter 2 a geologically oriented parameterization approach is presented, which reduces the number of parameters and improves the accuracy.

The migration approach builds on one-way true-amplitude wave equation extrapolation techniques which have proved to be successful for surface seismic migration. Similar to migration of surface data, the objective in the migration step is to get an estimate for the crosswell subsurface reflectivity using an efficient and accurate processing scheme. Finally, a detailed structural

image of the interwell subsurface is obtained. Application of the method to synthetic data can be found in Chapter 4, and a real data application can be found in Chapter 5.

Macro model estimation

2.1 Introduction

In Chapter 1 it has been explained that after pre-processing, the next step in the proposed crosswell inversion and imaging scheme is the estimation of a macro velocity model. This model is then used as a background model in the subsequent wavefield imaging step (see Chapter 3). This chapter is about the estimation of such a crosswell macro velocity model from measured traveltimes. An important difference between the surface seismic reflection and crosswell methods is that in the latter the direct waves have traveled through the whole subsurface region between the two boreholes. Thus, the direct waves contain information on the most interesting regions. In this chapter picked direct wave arrival times are used for the estimation of a macro velocity model. The picking problem is briefly discussed in Appendix A.

All seismic traveltime inversion methods start with the following continuous forward model:

$$T = \int_h s(x, y, z) dh. \quad (2.1)$$

In this equation, T is the traveltime of a seismic wave traveling along curve h (a ray) from one source to one receiver. Equation (2.1) expresses that to find the traveltime of the ray an integration over the raypath h in the subsurface must be carried out, integrating over the slowness field. The slowness s is defined as the inverse of the wave propagation velocity c : $s(x, y, z) = 1/c(x, y, z)$. The direct wave (or “shortest path” or “Fermat minimum time”) ray-path of the seismic wave can for example be computed by means of ray-tracing. Note that using the slowness is preferred to using the propagation velocity because the traveltime is linear in the slowness parameter. It is well known that for parameter estimation problems it is always advantageous to choose the model as linear as possible.

When given a set of traveltime measurements, the objective of a traveltime tomography procedure is to solve equation (2.1) for the slowness field. In formulating such an inversion scheme, the two most important issues to be considered are:

- **Forward model:** The parameterization of the subsurface velocity (or slowness) field and the computation of synthetic traveltimes.
- **Inversion:** The estimation of the parameters from the traveltimes by matching the modeled traveltimes with the measured traveltimes.

In this chapter first the general theory on nonlinear inversion is revisited. Use is made of Bayesian inversion theory, which actually is applicable to a wide range of seismic problems. Then, two specific forward model representations with corresponding solutions to the inverse problem are discussed. In the first approach, traveltime inversion using a parameterization based on a traditional “cell” discretization is discussed. The low accuracy of this method for typical seismic problems is demonstrated. It will be shown that the application of Bayesian inversion theory improves the results, but is still not satisfactory. Therefore, in the second approach a different kind of parameterization for the slowness field is introduced. This parameterization is related to the geological properties of the subsurface. It will be shown that with this method more accurate estimates can be obtained than with the cell-based method.

2.2 The principles of general iterative nonlinear inversion

2.2.1 Problem formulation

Let data vector \mathbf{d} contain discrete measured data and let a forward model representation be given by the nonlinear vector function $\mathbf{g}(\mathbf{x})$ where \mathbf{x} is a parameter vector. The objective of the inversion is to search for a vector \mathbf{x} such that the residual data difference vector (or error vector) $\Delta\mathbf{d}$ defined by

$$\Delta\mathbf{d} = \mathbf{d} - \mathbf{g}(\mathbf{x}) \quad (2.2)$$

is minimized with respect to a certain norm L . Thus, the approach is to solve the parameter estimation problem by using data fitting. Several norms that are commonly used are absolute value or linear (L_1), Euclidean (L_2), quasi linear (L_p with $1 < p < 2$) or minimax (L_∞). For example, the *least squares* objective function is defined as

$$F(\mathbf{x}) = \|\Delta\mathbf{d}\|_2^2 = (\mathbf{d} - \mathbf{g}(\mathbf{x}))^T (\mathbf{d} - \mathbf{g}(\mathbf{x})) \quad (2.3)$$

where the Euclidean norm has been chosen. The solution of the problem is now given by the value of the parameters in the global minimum of the objective function F .

A general solution to the nonlinear optimization problem is the iterative approach. It is visualized in Figure 2.1. Let \mathbf{x}_k be a vector containing the parameters of the forward model, with \mathbf{x}_0 the initial model parameter vector. For each k , the data mismatch vector $\Delta\mathbf{d}_k$ is computed using

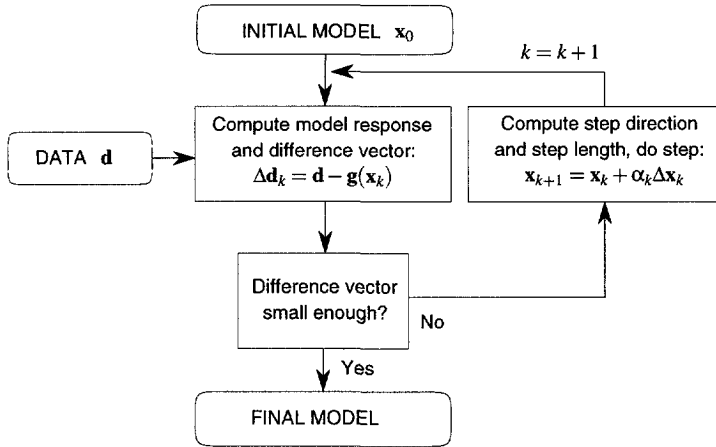


Fig. 2.1 Flow of a general nonlinear iterative inversion procedure.

the forward model $\mathbf{g}(\mathbf{x}_k)$. A particular method is used to compute a parameter update vector with direction $\Delta\mathbf{x}_k$ and step length α_k . With this update a new parameter vector is constructed:

$$\mathbf{x}_{k+1} = \mathbf{x}_k + \alpha_k \Delta\mathbf{x}_k \quad (2.4)$$

The next mismatch $\Delta\mathbf{d}_{k+1}$ is computed from $\mathbf{g}(\mathbf{x}_{k+1})$ and so on. If the norm of the difference vector $\|\Delta\mathbf{d}_{k+1}\|_L$ is small enough and convergence is observed, the iteration process is stopped. Ideally, the elements of the mismatch vector become zero to machine precision. But, three important practical aspects must be taken into account:

Non-Uniqueness - Although a typical seismic inversion problem involves more data points than unknowns, the system is commonly still underdetermined (ill-posed) because there are less independent equations than unknowns. This means that no information may be present in the data on a particular parameter, or on combinations of parameters. Thus, multiple parameter vectors may exist that yield the same norm of the data difference vector and which are all to be considered as “the” optimum solution. This corresponds to the existence of flat “valleys” in the parameter space. Note that apart from mathematical dependence, equations can become numerically dependent due to the limited numerical precision during the computations. In the underdetermined case the choice of the model update vector $\Delta\mathbf{x}_k$ is not unique either. Existing inversion algorithms differ in the way they handle this non-uniqueness and thus in the way the vectors $\Delta\mathbf{x}_k$ are chosen in the iterations.

Noise - On the other hand, the noise on the data may cause dependent equations to become independent. Thus, when more data points than parameters are present, the system of equations may actually have more independent equations than unknowns and may be called “overdetermined”.

For example, consider the linear system of equations

$$\begin{aligned} a + 3b &= d_1 \\ 2a + 6b &= d_2 \\ 3a + 9b &= d_3 \end{aligned} \tag{2.5}$$

In a noise-free situation, suppose that the “data” is given by $d_1 = 1$, $d_2 = 2$, $d_3 = 3$. Hence, the equations are dependent, the problem is ill-posed, and there is no unique solution. In a “noisy” situation we could have $d_1 = 1.05$, $d_2 = 2.10$, $d_3 = 2.90$ in which case a unique solution actually exists. If $d_1 = 1.05$, $d_2 = 2.20$, $d_3 = 2.90$, the system is overdetermined. Thus, mathematically and numerically the term “overdetermined” is correct, but it is confusing to use it in the seismic inversion context because, as has been argued above, a typical seismic inversion problem is underdetermined in the sense that it is ill-posed without considering the noise on the data. The terms “inconsistent” or “conflicting” are more appropriate. Due to the noise on the data, the forward model $\mathbf{g}(\mathbf{x})$ can never predict the data exactly and the data difference vector will never vanish.

Local minima - Because of the nonlinearities that may be present, the existence of multiple minima can be expected. It is not guaranteed at all that an algorithm converges to the global minimum of the norm of the data difference vector. It is more likely that the algorithm gets stuck in a *local* minimum. Furthermore, the local minimum that is finally reached depends on the initially chosen model.

With these aspects in mind, for the inversion a minimization approach must be developed which can deal with the non-uniqueness, which is robust with respect to noise and which can handle nonlinearities. With respect to the L_2 norm, it must be realized that if outliers are present (when some elements of $\Delta \mathbf{d}$ have a relatively large value), these will have a relatively strong influence on the value of the objective function, since the differences are squared. If outliers can not be identified and removed, the L_1 or L_p (with $1 < p < 2$) norms may be more appropriate, since then all differences have a more equal influence on the final results.

Defining the solution as the minimum of objective function (2.3) does not take statistical properties of the data into account. If measurement errors can be assigned to data values by means of standard deviations, it is customary to weight the data differences with the inverse of their respective standard deviations. Let \mathbf{C}_d be a diagonal matrix with data variances on its diagonal. Equation 2.2 is scaled with the data standard deviations by multiplying with $\mathbf{C}_d^{-1/2}$. This yields the *weighted least-squares* objective function F' :

$$F'(\mathbf{x}) = \|\Delta \mathbf{d}'\|_2^2 = (\mathbf{d} - \mathbf{g}(\mathbf{x}))^T \mathbf{C}_d^{-1} (\mathbf{d} - \mathbf{g}(\mathbf{x})). \tag{2.6}$$

Now data with the lowest standard deviations has the strongest influence on the objective function. Moreover, when using the minimum of equation 2.6, it is possible to compute a covariance

matrix of the estimated parameters. This is caused by the fact that the L_2 norm is closely related to a Gaussian distribution. The *statistical approach* is discussed in section 2.2.3.

2.2.2 Methods for minimization

General considerations

Iterative nonlinear minimization algorithms differ in the way the step $\Delta \mathbf{x}$ is calculated in each iteration. New parameter values are calculated based on a Taylor expansion around the last calculated parameter values¹. A second order expansion of the objective function F is given by

$$F(\mathbf{x}_{k+1}) = F(\mathbf{x}_k + \Delta \mathbf{x}) \approx F(\mathbf{x}_k) + \mathbf{q}_k^T \Delta \mathbf{x}_k + \frac{1}{2} \Delta \mathbf{x}_k^T \mathbf{H}_k \Delta \mathbf{x}_k \quad (2.7)$$

where vector \mathbf{q} contains the first order derivatives of F , and \mathbf{H} is the Hessian matrix containing the second order derivatives of F . The objective function and its first order derivatives must be continuous. Minimization algorithms in general use a minimum of two terms (function value + first order derivatives) and a maximum of three terms (including the Hessian) of the expansion. Using derivatives of higher order than two is computationally infeasible for typical seismic problems.

Based on the highest order of derivatives that are explicitly used, a division into three classes can be made:

1. The first class does not need explicit derivatives of the objective function. An approximation to the first order derivatives of the objective function is computed by only using values of the objective function itself. Non derivative methods are suited for problems for which it is too expensive to compute analytical first order derivatives. For large scale problems, conjugate gradient algorithms exist that do not need derivatives. In the seismic travelttime tomography context fast algebraic reconstruction techniques have been developed to solve large systems of linear equations. These solvers do not need large matrix storage space for the computation of the search direction.
2. The second class explicitly uses the first order derivatives of the objective function. This approach is more robust compared to using an approximation, but may be computationally more expensive. In general these methods have linear convergence properties, meaning that, roughly speaking, after each iteration we have one extra correct digit of the solution. Examples of first order derivative methods are steepest descent and Gauss-Newton. The Gauss-Newton method is especially developed for least-squares problems and can have quadratic convergence properties near the minimum (see below). This means that

¹Note that in this thesis only a local optimization approach is considered. Global methods, such as Monte-Carlo methods, are not discussed.

the number of correct digits approximately doubles after each iteration. Quasi-Newton methods use the change of the first order derivatives to update an approximation of the Hessian after each iteration. They can have quadratic convergence without needing a Hessian to be computed explicitly.

3. If also the second order derivatives (Hessian) are explicitly used the convergence rate may increase up to quadratic convergence. However, a full Hessian is, in general, expensive to compute. Therefore, the Quasi-Newton method is often preferred because it can achieve quadratic convergence while circumventing the calculation of a full Hessian. A Newton method is an example of a method which explicitly utilizes the Hessian, and has quadratic convergence properties.

Newton optimization methods generate the search direction $\Delta \mathbf{x}_k$ using the full second order Taylor approximation of the objective function F around \mathbf{x}_k (equation (2.7)). If the point \mathbf{x}_{k+1} is a minimum of F the first order derivative of F must vanish:

$$\mathbf{q}_{k+1} \approx \mathbf{q}_k + \mathbf{H}_k \Delta \mathbf{x}_k = 0 \quad (2.8)$$

and the right hand side of equation (2.7) is minimized by

$$\Delta \mathbf{x}_k = -\mathbf{H}_k^{-1} \mathbf{q}_k. \quad (2.9)$$

After determination of the step direction, the step length α_k is computed by a search along the "line" $\Delta \mathbf{x}_k$ of the objective function until it is at a minimum. For quadratic functions, equations (2.7)-(2.9) are exact and the minimum of the objective function is reached in one step with unit step length $\alpha = 1$.

A problem with the Newton method is that the Hessian may become singular which means that its inverse does not exist. This means that there is no well-defined minimum either. Solutions to this problem lead to the so called "modified Newton" methods, in which the Hessian is modified in such a way that it is positive definite. For a thorough overview and discussion on practical minimization methods see Gill et al. (1981).

Minimization for least squares problems

As already indicated a method especially developed for least squares problems is the Gauss-Newton method. This method may have quadratic convergence near the minimum of a least squares sum without needing an expensive Hessian to be computed. Bishop et al. (1985) use the method for tomographic travelttime inversion of surface data. For notational convenience objective function (2.3) will be used in this section. It is often found in the literature where statistical properties of the data are not taken into account. But the following discussion also applies to equation (2.6) by multiplying all occurrences of $\mathbf{g}(\mathbf{x})$, the Jacobian of $\mathbf{g}(\mathbf{x})$ and \mathbf{d} with

$\underline{C}_d^{-1/2}$. Note that if \underline{C}_d is a diagonal matrix with equal valued elements (i.e. $\underline{C}_d = \sigma^2 \underline{I}$ with \underline{I} the unit matrix) the values of the parameters in the local minimum of equation (2.3) is the same as in the local minimum of equation (2.6).

The gradient \mathbf{q} of the objective function (2.3) is given by

$$\mathbf{q} = -\underline{\mathbf{J}}^T \Delta \mathbf{d} \quad (2.10)$$

with matrix $\underline{\mathbf{J}}$ the Jacobian of the forward model $\mathbf{g}(\mathbf{x})$ with elements J_{ij} given by

$$J_{ij} = \partial g_i / \partial x_j \quad (2.11)$$

The Hessian $\underline{\mathbf{H}}$ is given by

$$\underline{\mathbf{H}} = \underline{\mathbf{J}}^T \underline{\mathbf{J}} - \sum_i^m \Delta d_i \underline{\mathbf{T}}_i \quad (2.12)$$

with i running over all m elements of $\Delta \mathbf{d}$ and $\underline{\mathbf{T}}_i$ the Hessian matrix of element i of vector $\mathbf{g}(\mathbf{x})$ (i.e. $g_i(\mathbf{x})$). If the Hessian of \mathbf{g} is small (near-linear model) or if the data residual is small (near the minimum of F) a good approximation of the Hessian $\underline{\mathbf{H}}$ is $\underline{\mathbf{H}} = \underline{\mathbf{J}}^T \underline{\mathbf{J}}$. In this case the Hessian can be computed from the Jacobian matrix. Using this approximation and (2.10) in the Newton update (2.9) gives the Gauss-Newton update:

$$\Delta \mathbf{x}_k = [\underline{\mathbf{J}}_k^T \underline{\mathbf{J}}_k]^{-1} \underline{\mathbf{J}}_k^T \Delta \mathbf{d}_k. \quad (2.13)$$

Note that this is a least squares solution of the problem

$$\underline{\mathbf{J}}_k \Delta \mathbf{x}_k = \Delta \mathbf{d}_k \quad (2.14)$$

if $\underline{\mathbf{J}}_k$ is assumed to be independent of $\Delta \mathbf{x}_k$. In case of a linear model equation (2.13) gives the exact solution in one step with unit length $\alpha = 1$. But as was the case with the Newton method, $\underline{\mathbf{J}}_k^T \underline{\mathbf{J}}_k$ is often not invertible or it is very poorly conditioned due to the non-uniqueness of the problem. Commonly, a damping term is introduced, leading to a damped least squares solution (see next section).

The Quasi-Newton update is obtained by taking for the Hessian

$$\underline{\mathbf{H}} = \underline{\mathbf{J}}^T \underline{\mathbf{J}} - \sum_i^m \Delta d_i \underline{\mathbf{B}}_i \quad (2.15)$$

with $\underline{\mathbf{B}}_i$ a numerical approximation to the Hessian $\underline{\mathbf{T}}_i$. Matrix $\underline{\mathbf{B}}_i$ is updated after each iteration with some updating formula. This updating formula uses information on the change of the Jacobian $\underline{\mathbf{J}}$ of the forward model and also ensures that the Hessian $\underline{\mathbf{H}}$ is positive definite.

Damped least squares solutions

Special damped least squares solvers have been developed to solve the kind of problems involving underdetermined systems of equations like equation (2.13). Instead of inverting the matrix $\underline{\mathbf{J}}^T \underline{\mathbf{J}}$ the following system is solved:

$$[\underline{\mathbf{J}}_k^T \underline{\mathbf{J}}_k + \beta \underline{\mathbf{V}}_k^{-1}] \Delta \mathbf{x}_k = \underline{\mathbf{J}}_k^T \Delta \mathbf{d}_k \quad (2.16)$$

The matrix $\beta \underline{\mathbf{V}}_k^{-1}$ is the damping term, for example derived from statistical properties of the noise in the data. The solution of equation (2.16) is called the damped least squares solution of equation (2.14). It can be shown that if the subsequent iterations of the nonlinear inversion procedure converge using the update from (2.16), the gradient of the objective function $\underline{\mathbf{J}}^T \Delta \mathbf{d}$ vanishes, irrespective of the damping term $\beta \underline{\mathbf{V}}_k^{-1}$. Thus a local minimum is reached. However, the initial model and the damping term influence the rate of convergence and they also may have influence on which local minimum is finally reached.

A cross-hole seismology example of the application of the damped least squares solution can be found in Bregman et al. (1989a), where the damping term is taken as $\kappa^2 \underline{\mathbf{I}}$, with $\underline{\mathbf{I}}$ a unit matrix. It is explained that κ determines the level of eigenvalues allowed to contribute to the solution, without explicitly computing a singular value decomposition. Taking the damping term as $\kappa^2 \underline{\mathbf{I}}$ is referred to as a Levenberg-Marquardt method.

It is important to realize that the usage of a damped least squares approach with an arbitrary “rule of thumb” damping term results in a smoothing of the solution that is also arbitrary. For example in traveltimes tomography methods, if the damping term is taken too high, the results look very clean and smooth. However, they are not based on a theoretical basis. It is also difficult to interpret the results of a highly damped solution. If the damping is taken too low, eigenvectors corresponding to low eigenvalues from underdetermined directions in the parameter space will contaminate the solution with numerical noise effects. Thus, a damping term must at least be based on the statistical noise properties of the data.

Introducing damping means introducing a priori information into the solution. The next section shows how a theoretical basis can be established by explicitly introducing a priori information into the (traveltimes) inversion procedure.

2.2.3 Statistical inversion: the Bayesian approach

Instead of one solution, the Bayesian approach yields a probability density function (“pdf”) describing the possible values of the a posteriori parameters in a statistical sense. Different levels of confidence can be assigned to the data and the a priori information. The probability is interpreted as a “degree of belief”. From the a posteriori pdf, conclusions can be drawn on the accuracy, mutual correlation and resolvability of the parameters. These are related to the final spatial resolution that can be obtained. The original Bayesian interpretation is made by Thomas

Bayes and was published posthumously (Bayes (1763)). In this thesis, a summary of Bayesian inversion theory is presented. Detailed discussions on the application of Bayesian theory in seismic inversion can be found in Tarantola (1987) and Duijndam (1988a, 1988b).

Choosing the type of the error distributions

For statistical parameter estimation problems an important and often raised question is: what can be assumed for the error distributions on the data (noise) and the a priori information? There are strong arguments in favor of a Gaussian pdf (a normal distribution). Given the mean and covariance, a Gaussian pdf has the least informational content as determined by Shannon's information measure (Shannon (1948)). This means that using the mean and the covariance, by choosing the Gaussian pdf we do not use more information than we legitimately know. Furthermore, the Gaussian distribution is mathematically attractive, it resembles the behavior in distribution of many physical processes in nature and it follows from the central limit theorem.

Because of its exponential behavior, the Gaussian distribution is relatively wide around the mean and quickly goes to zero away from the mean. For the Gaussian distribution, the interval of $(m - \sigma, m + \sigma)$ with m the mean and σ the standard deviation corresponds to a 67% confidence interval, and $(m - 2\sigma, m + 2\sigma)$ corresponds to a 95% confidence interval. These observations come close to how we like to describe the (subjective) confidence of a parameter.

For these reasons, in this research the Gaussian distribution is used for describing the uncertainty on the a priori parameters and for the influence of noise on the data. The Gaussian distribution is combined with hard constraints in regions where the pdf is zero. For example, velocities can not be negatively valued and thus the pdf for a velocity parameter is set to zero for values less or equal than zero.

Bayes' rule and the point estimate

Suppose that the state of information on the parameters and the data is given by the pdf $p(\mathbf{x}, \mathbf{y})$, where \mathbf{x} is the vector with the parameters and vector \mathbf{y} contains discretized data. Then the state of information on the parameters given the data \mathbf{y} is described by the conditional pdf

$$p(\mathbf{x}|\mathbf{y}) = \frac{p(\mathbf{x}, \mathbf{y})}{p(\mathbf{y})}. \quad (2.17)$$

A similar relation can be stated for $p(\mathbf{y}|\mathbf{x})$ as

$$p(\mathbf{y}|\mathbf{x}) = \frac{p(\mathbf{x}, \mathbf{y})}{p(\mathbf{x})}, \quad (2.18)$$

and using equation (2.18) in equation (2.17) Bayes' rule is obtained:

$$p(\mathbf{x}|\mathbf{y}) = \frac{p(\mathbf{y}|\mathbf{x})p(\mathbf{x})}{p(\mathbf{y})}. \quad (2.19)$$

The pdf $p(\mathbf{x}|\mathbf{y})$ is called the *a posteriori* pdf. The function $p(\mathbf{y}|\mathbf{x})$ is the conditional pdf of \mathbf{y} given \mathbf{x} . It contains the theoretical relations between parameters and data including the noise properties. The function $p(\mathbf{x})$ is the marginal pdf of $p(\mathbf{x}|\mathbf{y})$ for \mathbf{x} . It is the probability density function for the parameters when the data is not taken into account. Thus, it describes the *a priori* information of the parameters. Pdf $p(\mathbf{y})$ is the pdf of the data when nothing is assumed on the parameters. It can be seen as a constant normalization factor.

Actually, $p(\mathbf{x}|\mathbf{y})$ is the solution to the inverse problem. It contains all information on the parameters given the measurements. But in practice it is often impossible to compute a pdf over the whole parameter space. Therefore a point estimate is used, for which the maximum of the pdf is an often used probability. This point estimate is interpreted as the most likely value of the parameters given the data, theory and a priori parameters. Two point estimates are discussed here. The first is the maximum of the pdf when no a priori information is taken into account, and is called the Maximum Likelihood Estimate (MLE). In the second, the a priori information is taken into account, and then the Maximum of the A posteriori Probability density function (MAP) is taken.

Define a forward model according to

$$\mathbf{y} = \mathbf{g}(\mathbf{x}) + \mathbf{n} \quad (2.20)$$

where $\mathbf{g}(\mathbf{x})$ is the forward (nonlinear) model to calculate the synthetic data from, and vector \mathbf{n} contains the errors in the theory and the noise on the data. When \mathbf{n} is independent of $\mathbf{g}(\mathbf{x})$ and has a pdf p_n , for the probability of the data given the parameters it follows that

$$p(\mathbf{y}|\mathbf{x}) = p_n(\mathbf{y} - \mathbf{g}(\mathbf{x})). \quad (2.21)$$

Now let the result of some measurement be denoted by a vector of numbers \mathbf{d} . If $\mathbf{y} = \mathbf{d}$ is substituted in equation (2.21) then the result, interpreted as a function of \mathbf{x} is called the *likelihood function* $l(\mathbf{x})$:

$$l(\mathbf{x}) = p(\mathbf{y} = \mathbf{d}|\mathbf{x}) = p_n(\mathbf{d} - \mathbf{g}(\mathbf{x})) \quad (2.22)$$

where equation (2.20) is used. If a Gaussian distribution is chosen for the description of the noise on the data, then

$$p_n(\mathbf{n}) = \frac{1}{(2\pi)^{n/2} |\mathbf{C}_n|^{1/2}} \exp\left\{-\frac{1}{2} \mathbf{n}^T \mathbf{C}_n^{-1} \mathbf{n}\right\} \quad (2.23)$$

with zero mean and covariance \mathbf{C}_n . Then the likelihood function follows from equation (2.22) as

$$p(\mathbf{y} = \mathbf{d}|\mathbf{x}) = \text{constant} \cdot \exp\left\{-\frac{1}{2} \{(\mathbf{d} - \mathbf{g}(\mathbf{x}))^T \mathbf{C}_n^{-1} (\mathbf{d} - \mathbf{g}(\mathbf{x}))\}\right\}. \quad (2.24)$$

The Maximum Likelihood Estimation (MLE) point estimate is defined as the value the parameters have when the likelihood function is maximized. This means that the exponent of equation (2.24) must be minimized. Defining the objective function

$$2F_{MLE}(\mathbf{x}) = (\mathbf{d} - \mathbf{g}(\mathbf{x}))^T \mathbf{C}_n^{-1} (\mathbf{d} - \mathbf{g}(\mathbf{x})), \quad (2.25)$$

the MLE point estimate can be computed by minimizing F_{MLE} . This is a weighted nonlinear least squares or L_2 norm. It yields exactly the same point estimate as was found in the previous section (see equation (2.6)), but now it is derived from a statistical point of view.

Now the a priori knowledge is introduced. When choosing a pdf for the a priori data, the same arguments as were used for the choice of the pdf for the noise apply. Therefore the a priori pdf is assumed to have a Gaussian probability density function, with mean \mathbf{x}^a and covariance matrix \mathbf{C}_x :

$$p(\mathbf{x}) = \frac{1}{(2\pi)^{n/2} |\mathbf{C}_x|^{1/2}} \exp\left\{-\frac{1}{2}(\mathbf{x}^a - \mathbf{x})^T \mathbf{C}_x^{-1} (\mathbf{x}^a - \mathbf{x})\right\} \quad (2.26)$$

where the values of the a priori parameters are given by vector \mathbf{x}^a . The maximum of the a posteriori objective function (equation (2.17)) is computed by maximizing the product of $p(\mathbf{x})$ and $p(\mathbf{y} = \mathbf{d}|\mathbf{x})$ (equation (2.24)). This procedure is referred to as MAP (Maximum of A posteriori Probability density function) estimation. It is equivalent to minimizing the sum of the two exponents of this product, as given by the minimum of the objective function F :

$$2F(\mathbf{x}) = (\mathbf{d} - \mathbf{g}(\mathbf{x}))^T \mathbf{C}_n^{-1} (\mathbf{d} - \mathbf{g}(\mathbf{x})) + (\mathbf{x}^a - \mathbf{x})^T \mathbf{C}_x^{-1} (\mathbf{x}^a - \mathbf{x}) \quad (2.27)$$

which again is a weighted nonlinear least squares norm.

The a posteriori covariance matrix

In general the covariance matrix is computed by integration over the whole parameter space. In practice this is not feasible. Fortunately a good approximation is possible when the forward model is (nearly) linear in the maximum of the pdf $p(\mathbf{x}|\mathbf{y})$. In the minimum of the objective function F the gradient of F vanishes and a second order Taylor approximation around the minimum is given by

$$F(\mathbf{x}) \approx F(\hat{\mathbf{x}}) + \frac{1}{2}(\mathbf{x} - \hat{\mathbf{x}})^T \mathbf{H}(\mathbf{x} - \hat{\mathbf{x}}), \quad (2.28)$$

where $\Delta\mathbf{x} = \mathbf{x} - \hat{\mathbf{x}}$ and \mathbf{H} is the Hessian of F . If the objective function is defined as the negative logarithm of the a posteriori pdf, $F(\mathbf{x}) = -\ln(p(\mathbf{x}|\mathbf{y}))$, it follows that

$$p(\mathbf{x}|\mathbf{y}) \approx p(\hat{\mathbf{x}}|\mathbf{y}) \exp\left\{-\frac{1}{2}(\mathbf{x} - \hat{\mathbf{x}})^T \mathbf{H}(\mathbf{x} - \hat{\mathbf{x}})\right\}. \quad (2.29)$$

Thus the a posteriori pdf looks like a Gaussian distribution with mean $\mathbf{x} = \hat{\mathbf{x}}$ and covariance matrix $\mathbf{C}_{\hat{\mathbf{x}}} = \mathbf{H}^{-1}$. This holds true irrespective of the distribution involved for noise and a priori

information, provided of course that approximation (2.28) holds. For linear models and Gaussian assumptions, (2.28) and (2.29) are exact.

For the calculation of the Hessian of F , equation (2.27) can be rewritten as

$$2F(\mathbf{x}) = \sum_i e_i^2 = \mathbf{e}^T \mathbf{e} \quad (2.30)$$

where the residual vector \mathbf{e} is given by

$$\mathbf{e} = \begin{bmatrix} \underline{\mathbf{C}}_n^{-1/2}(\mathbf{d} - \mathbf{g}(\mathbf{x})) \\ \underline{\mathbf{C}}_x^{-1/2}(\mathbf{x}^a - \mathbf{x}) \end{bmatrix}. \quad (2.31)$$

It expresses that the data and parameter mismatches are weighted by their uncertainties. The gradient \mathbf{q} of F is given by

$$\mathbf{q} = \underline{\mathbf{J}}^T \mathbf{e}, \quad (2.32)$$

where $\underline{\mathbf{J}}$ is the Jacobian matrix of \mathbf{e} :

$$J_{ij} = \frac{\partial e_i}{\partial x_j}. \quad (2.33)$$

Finally, the Hessian of F is given by

$$\underline{\mathbf{H}} = \underline{\mathbf{J}}^T \underline{\mathbf{J}} + \sum_{i=1}^m e_i \underline{\mathbf{T}}_i, \quad (2.34)$$

where m is the number of elements of \mathbf{e} and $\underline{\mathbf{T}}_i$ is the Hessian of e_i^2 . For low residuals e_i and/or for quasi-linear problems, in which the $\underline{\mathbf{T}}_i$ matrices contain low values, the Hessian can be approximated by:

$$\underline{\mathbf{H}} \approx \underline{\mathbf{J}}^T \underline{\mathbf{J}}. \quad (2.35)$$

This expression is exact for linear models. Using equation (2.35) the a posteriori covariance matrix as is used in this thesis for Bayesian inversion follows according to:

$$\underline{\mathbf{C}}_{\hat{\mathbf{x}}} = \underline{\mathbf{H}}^{-1} \approx (\underline{\mathbf{J}}^T \underline{\mathbf{J}})^{-1} = \left[\underline{\mathbf{J}}^T \underline{\mathbf{C}}_n^{-1} \underline{\mathbf{J}} + \underline{\mathbf{C}}_x^{-1} \right]^{-1}, \quad (2.36)$$

with $\underline{\mathbf{J}}'$ the Jacobian of the unscaled forward model $\mathbf{g}(\mathbf{x})$ (i.e. equation (2.11)). If MLE estimation is used, then the corresponding covariance matrix follows from equation (2.36) by putting the matrix $\underline{\mathbf{C}}_x^{-1}$ to zero:

$$\underline{\mathbf{C}}_{\hat{\mathbf{x}}_{MLE}} = \left[\underline{\mathbf{J}}'^T \underline{\mathbf{C}}_n^{-1} \underline{\mathbf{J}}' \right]^{-1}. \quad (2.37)$$

²Note that with respect to the notation the symbols for the Jacobian $\underline{\mathbf{J}}$ and Hessian $\underline{\mathbf{H}}$ of the *objective* function do not have the same meaning as the ones in the section on minimization (i.e. equations (2.10)-(2.16)), where the first order derivatives are those of the *forward model* $\mathbf{g}(\mathbf{x})$. Derivatives of the forward model will be indicated by a prime (') from here on.

This can be seen as assuming that all a priori values of the parameters are equally likely, by putting $\underline{\mathbf{C}}_x^{-1}$ in (2.36) and (2.26) to zero.

A closer look at the equations for MLE and MAP inversion reveals the meaning of a scaling with $\underline{\mathbf{C}}_n^{-1}$: data mismatches corresponding to data with high variance (which are found on the diagonal of $\underline{\mathbf{C}}_n$) have less influence on the objective function than data mismatches corresponding to data with low variance. Furthermore, for the MAP estimator, a priori knowledge which is known with high accuracy influences the objective function most in comparison to a priori knowledge that is not known accurately. This is due to a similar scaling with the inverse of the a posteriori covariance matrix $\underline{\mathbf{C}}_x^{-1}$.

From the a posteriori covariance matrix, a correlation matrix can be computed, obtained by dividing all rows and columns of the covariance matrix by the standard deviation of the parameter corresponding to that particular row/column. This will result in unit values on the diagonal. The other values are an indication of the correlation between the parameters.

A more detailed analysis can be performed by using a singular value decomposition on the covariance matrix. From the singular values and eigenvectors the directions in the parameter space along which the problem is well resolved or ill resolved can be identified. For examples in the context of seismic exploration see Duijndam (1988b) and Scheffers (1993).

2.2.4 Concluding remarks on nonlinear inversion

Since seismic problems are commonly underdetermined, solving them using a Maximum Likelihood estimator is bound to fail. It is possible to try to minimize expression (2.6)/(2.25) for example by using a Gauss-Newton algorithm. But most probably the computations will fail because of numerical overflow or they will give highly erroneous results. Thus, some kind of stabilization must always be used. The damped least squares and the Bayesian approach both overcome these stability problems. Comparing these two methods, it can be argued that Bayesian inversion is preferred. If the Bayesian approach is used, the Jacobian of the objective function is given by (see equation (2.33)):

$$\underline{\mathbf{J}} = \begin{pmatrix} -\underline{\mathbf{C}}_n^{-1/2} \underline{\mathbf{J}}' \\ \underline{\mathbf{C}}_x^{-1/2} \end{pmatrix}. \quad (2.38)$$

The update of the parameters for the next iteration of the inversion is computed by solving update equation (2.13) with the new Jacobian $\underline{\mathbf{J}}$ of equation (2.38) and a residual vector \mathbf{e} according to (2.31) instead of $\Delta \mathbf{d}$:

$$\underline{\mathbf{J}}_k^T \underline{\mathbf{J}}_k \Delta \mathbf{x}_k = -\underline{\mathbf{J}}_k^T \Delta \mathbf{e}_k \quad (2.39)$$

or, written out explicitly, using (2.38):

$$[\underline{\mathbf{J}}_k^T \underline{\mathbf{C}}_n^{-1} \underline{\mathbf{J}}_k + \underline{\mathbf{C}}_x^{-1}] \Delta \mathbf{x}_k = \underline{\mathbf{J}}_k^T \underline{\mathbf{C}}_n^{-1} \Delta \mathbf{d}_k + \underline{\mathbf{C}}_x^{-1} (\mathbf{x}^a - \mathbf{x}_k). \quad (2.40)$$

Equation (2.40) can directly be compared to the damped least squares equation (2.16). It is concluded that Bayesian inversion is not the same as damped least squares inversion. Indeed, for the matrix inversion operation a better stability is achieved by introducing the inverse covariance matrix of the a priori parameters \underline{C}_x^{-1} in the left hand side of equation (2.40). It is a statistically justified way to limit the singular values of the inverse matrix in the equation by setting the damping term $\beta \underline{V}_k^{-1}$ to \underline{C}_x^{-1} . But the second term on the right hand side of (2.40) is not present in the damped least squares solution. This term will dominate the search direction along directions in the parameter space on which there is no information in the data.

It is also important to note that for a nonlinear forward model the local minima found by the iterative process using update formula (2.40) can differ from those found by using equation (2.16) with $\beta \underline{V}_k^{-1} = \underline{C}_x^{-1}$. If with (2.40) an initial model is chosen and for example one parameter is ill resolved (near zero values in the Jacobian), the value of that parameter tends to converge to its a priori value. For the damped least squares solution, the values of the parameters are limited after each iteration, but the final value of an ill-resolved parameter depends on the (possibly arbitrary) damping term, and the number of iterations used.

Expression (2.40) again shows the trade off between the influence of the data and the influence of the a priori information. If the a priori information is very weak, \underline{C}_x^{-1} will be small and the search for a minimum will follow the directions determined by the data and vice versa. In practice \underline{C}_x^{-1} must be large enough to stabilize the matrix inversion needed to compute $\Delta \underline{x}_k$.

2.3 Traditional cell-based traveltimes tomography

In this section traditionally used *cell-based* inversion procedures are investigated using the inversion theory outlined in the previous section. Because of the underdetermination of the problem, traditionally some kind of damping or regularization is applied, which smoothes the results. In this thesis the traditional method is extended to include Bayesian inversion theory, as proposed by Vos et al. (1990). The purpose here is to show that, even with Bayesian inversion, the accuracy of cell-based inversions is not satisfactory for typical seismic problems. This is why a new approach to the parameterization of the model is proposed in section 2.4 of this thesis.

2.3.1 Nonlinear cell-based traveltimes inversion

Crosswell traveltimes tomography aims at inverting first arrival traveltimes picks into a subsurface model. A cell-based traveltimes inversion approach is taken if the medium in-between the boreholes is divided into a number of (square) cells. Each cell has a specific slowness or velocity value. In the inversion process, traveltimes picked from field data are matched with synthetic traveltimes to compute an estimate of the parameters. To compute the synthetic traveltimes of waves traveling from sources to receivers, a ray-tracing algorithm can be used. This is illus-

trated in Figure 2.2 for a 10x15 subsurface model with square cells. For a general inhomogeneous medium, the rays are curved.

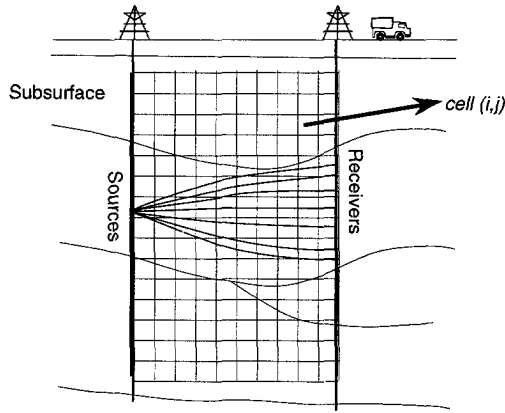


Fig. 2.2 Illustration of ray-tracing through a classical cell subsurface model with a parameterization of the subsurface into a matrix of 10x15 square cells. Rays are shot from the sources in the left borehole to receivers (geophones) in the right borehole.

As there are only two boreholes, the problem is two-dimensional. Let the slowness in a cell be given by $s_{i,j}$, with i the cell number in depth and j the cell number along the horizontal direction. The first arrival traveltimes t_k for a shot-receiver combination k (ray number k) is given by the discrete formula

$$t_k = \sum_{i,j} \Delta h_{k,i,j} s_{i,j} \quad (2.41)$$

where $\Delta h_{k,i,j}$ is the distance traveled in cell (i,j) for ray k . If all the slowness parameters are put into one parameter vector \mathbf{x} and all traveltimes are described by the vector function \mathbf{g} , then (2.41) can be written as a matrix-vector equation:

$$\mathbf{g}(\mathbf{x}) = \underline{\mathbf{A}}(\mathbf{x})\mathbf{x} \quad (2.42)$$

where matrix $\underline{\mathbf{A}}$ contains the distances $\Delta h_{k,i,j}$ and depends on the raypaths through the subsurface model.

Equation (2.42) is nonlinear. Thus, the theory for nonlinear iterative inversion of section (2.2) can readily be applied. Here the emphasis is put on the properties of the inversion when a cell parameterization is chosen in combination with ray-tracing to compute the traveltimes in the forward model.

Again an initial model \mathbf{x}_0 is assumed. Ray-tracing through the initial model gives the raypaths $\underline{\mathbf{A}}(\mathbf{x}_0)$ and the modeled traveltimes $\mathbf{g}(\mathbf{x}_0)$. Then from the difference of the real data \mathbf{d} and the

modeled traveltimes, $\Delta \mathbf{d}_0 = \mathbf{d} - \mathbf{g}(\mathbf{x}_0)$ (equation (2.2)), an update $\Delta \mathbf{x}_0$ must be computed. Because of the large number of parameters and the difficulties of calculating analytical first order derivatives, a non-derivative method must be used. Actually an approximation is used for the first order derivatives, but without the extra computations which are needed when for example a finite difference approximation is used. This is shown below.

Consider the first order "update equation"

$$\left. \frac{\partial \mathbf{g}}{\partial \mathbf{x}} \right|_{\mathbf{x}=\mathbf{x}_k} \Delta \mathbf{x}_k = \Delta \mathbf{d}_k \quad (2.43)$$

with data difference vector $\Delta \mathbf{d}_k = \mathbf{d} - \mathbf{g}(\mathbf{x}_k)$. The Jacobian of \mathbf{g} is given by

$$\frac{\partial \mathbf{g}}{\partial \mathbf{x}} = \frac{\partial \underline{\mathbf{A}}(\mathbf{x})}{\partial \mathbf{x}} \mathbf{x} + \underline{\mathbf{A}}(\mathbf{x}). \quad (2.44)$$

This is also a nonlinear expression which implies that it is difficult to solve update equation (2.43) for $\Delta \mathbf{x}_k$. Therefore a linearization is used. It is assumed that the raypaths depend on the current model only; they are supposed to be *independent* of the slowness parameters of the next iteration. This yields $\partial \underline{\mathbf{A}}(\mathbf{x}) / \partial \mathbf{x} = 0$, and thus the Jacobian becomes

$$\frac{\partial \mathbf{g}}{\partial \mathbf{x}} = \underline{\mathbf{A}}(\mathbf{x}). \quad (2.45)$$

Using this result in (2.43) yields the *linear* system of equations

$$\underline{\mathbf{A}}(\mathbf{x}_k) \Delta \mathbf{x}_k = \Delta \mathbf{d}_k, \quad (2.46)$$

with data difference vector $\Delta \mathbf{d}_k = \mathbf{d} - \mathbf{g}(\mathbf{x}_k)$. No explicit derivatives are needed; the update is computed by using the old raypaths and by varying the slowness parameters. This involves solving a linear system of equations. As is illustrated in Figure (2.3), a new parameter vector is constructed using the update, new raypaths are computed and the whole process is repeated until the data difference vector is small enough. In essence this is the method used in crosswell tomography in all non-derivative methods.

However, some additional problems must be faced first. One row in $\underline{\mathbf{A}}$ contains only a few nonzero parameters, because one ray only intersects a small number of cells. This means that $\underline{\mathbf{A}}$ is a sparse matrix. For a general experiment the system of equations (2.46) has more equations (data points) than unknowns. It has no unique solution because matrix $\underline{\mathbf{A}}$ is singular and there are a lot of conflicting equations due to the noise on the data. Furthermore, there is a large number of parameters and a large number of data points. A number of traditional solving techniques exist for this problem that can deal with the large number of parameters, such as ART (Algebraic Reconstruction Technique) and SIRT (Simultaneous Iterative Reconstruction Technique) (Dines and Lytle (1979), Ivansson (1986)). These simple back-projection methods directly solve the system of equations (2.46) by algebraic manipulation of the equations and can

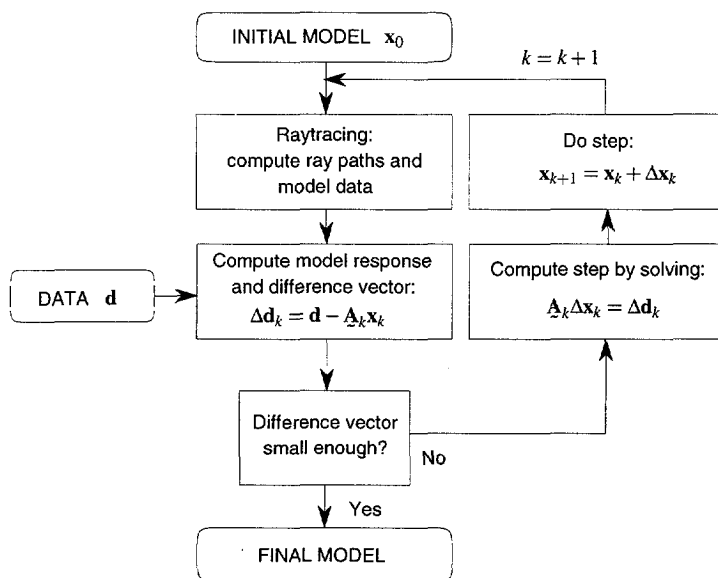


Fig. 2.3 Flow of a nonlinear iterative unconstrained inversion procedure using ray-tracing and a non-derivative method.

be fast. With these methods it is however difficult to determine a criterion for when to stop the iterative process. The iterations must be stopped before the image deteriorates too much due to high frequency fluctuations. This requires a rather intuitive measure. Furthermore, it is not possible to include a priori knowledge. But if on the other hand the least squares norm is used together with all available a priori information a unique inversion is possible.

For the linear system (2.46) a unique solution in the least squares sense is mathematically given by

$$\Delta x_k = (\mathbf{A}_k^T \mathbf{A}_k)^{-1} \mathbf{A}_k^T \Delta d_k. \quad (2.47)$$

But the inverse operation can not be performed since $\mathbf{A}_k^T \mathbf{A}_k$ is likely to be also (numerically) singular and then the solution is not unique at all. One approach is to limit the singular value range of the matrix $\mathbf{A}_k^T \mathbf{A}_k$, by utilizing a singular value decomposition or by using a damped least squares solution (see equation (2.16) on page 22). But in this section the Bayesian approach is taken under Gaussian assumptions of the data and a priori information. This leads to a least squares formulation with an objective function containing a sum of squares.

2.3.2 Linear Bayesian inversion

Because the only purpose of this section is to argue that a cell-based parameterization is not a good candidate for the estimation of the macro velocity model, linear inversion is used. The general Bayesian inversion theory leads to the minimization of an objective function of the form of equation (2.27). It is now assumed that the raypaths are independent of the current slowness parameters. The Jacobian of the forward model is then given by $\partial \mathbf{g} / \partial \mathbf{x} = \underline{\mathbf{A}}(\mathbf{x})$ (see equations (2.43)-(2.45)). This can be used in the Gauss-Newton update, which needs the first order derivatives of the forward model. One iteration step is computed from an initial model \mathbf{x}_0 leading to an estimate \mathbf{x}_1 , with $\mathbf{x}_1 = \mathbf{x}_0 + \Delta \mathbf{x}_0$. Using equation (2.40) with $\underline{\mathbf{J}}_0 = \underline{\mathbf{A}}$, $\Delta \mathbf{x}_0 = \mathbf{x}_1 - \mathbf{x}_0$ and $\Delta \mathbf{d}_0 = (\mathbf{d} - \underline{\mathbf{A}}\mathbf{x}_0)$ gives the linear system of equations

$$[\underline{\mathbf{A}}^T \underline{\mathbf{C}}_n^{-1} \underline{\mathbf{A}} + \underline{\mathbf{C}}_x^{-1}](\mathbf{x}_1 - \mathbf{x}_0) = \underline{\mathbf{A}}^T \underline{\mathbf{C}}_n^{-1}(\mathbf{d} - \underline{\mathbf{A}}\mathbf{x}_0) + \underline{\mathbf{C}}_x^{-1}(\mathbf{x}_0 - \mathbf{x}^a) \quad (2.48)$$

with \mathbf{x}^a the a priori model parameter vector, $\underline{\mathbf{C}}_n$ the data covariance matrix and $\underline{\mathbf{C}}_x$ the covariance matrix of the a priori parameters.

The solution of this system is actually independent of \mathbf{x}_0 . Removing these terms from the left- and the right-hand side and solving for \mathbf{x}_1 gives the inversion formula

$$\mathbf{x}_1 = (\underline{\mathbf{A}}^T \underline{\mathbf{C}}_n^{-1} \underline{\mathbf{A}} + \underline{\mathbf{C}}_x^{-1})^{-1} (\underline{\mathbf{A}}^T \underline{\mathbf{C}}_n^{-1} \mathbf{d} + \underline{\mathbf{C}}_x^{-1} \mathbf{x}^a). \quad (2.49)$$

The corresponding covariance matrix is given by

$$\underline{\mathbf{C}}_{\hat{\mathbf{x}}} = (\underline{\mathbf{A}}^T \underline{\mathbf{C}}_n^{-1} \underline{\mathbf{A}} + \underline{\mathbf{C}}_x^{-1})^{-1}. \quad (2.50)$$

In the seismic literature on cell-based tomography equation (2.49) is presented as the solution of the inverse problem when straight rays are assumed. Actually it is more general: it means that an initial model with a particular value of the slowness field is taken and one iteration of the nonlinear problem is performed with the assumption that the raypaths are independent of the slownesses. In addition to this assumption it is computationally advantageous to use a straight-ray approximation and to use straight initial raypaths. This corresponds to taking a constant initial background medium. The estimate (2.49) then updates the constant background while keeping the raypaths straight. It is the experience of several researchers that straight-ray travel-time inversion will perform reasonably well when the velocity never departs from the average by more than about 10 percent (Dines and Lytle (1979)). Lines and LaFehr (1989) show that the straight-ray assumption gives good results for the computed traveltimes in moderate contrast media. Therefore, in the examples shown in this section a straight-ray assumption is used.

In case of maximum likelihood estimation, all a priori information is equally likely. The ML estimate with corresponding covariance matrix is thus found by putting the inverse of the a priori covariance matrix to zero in (2.49) and (2.50):

$$\mathbf{x}_1 = (\underline{\mathbf{A}}^T \underline{\mathbf{C}}_n^{-1} \underline{\mathbf{A}})^{-1} \underline{\mathbf{A}}^T \underline{\mathbf{C}}_n^{-1} \mathbf{d}. \quad (2.51)$$

The corresponding covariance matrix is given by

$$\underline{C}_{\hat{x}} = (\underline{A}^T \underline{C}_n^{-1} \underline{A})^{-1}. \quad (2.52)$$

Finally, if the data covariance matrix is a diagonal matrix with equal valued elements, matrix \underline{C}_n may be eliminated from equation (2.51) and the maximum likelihood estimator becomes the standard linear least squares estimator:

$$\underline{x}_1 = (\underline{A}^T \underline{A})^{-1} \underline{A}^T \underline{d}. \quad (2.53)$$

2.3.3 Inversion examples for linear cell models

In order to analyze the resolution and accuracy of traditional cell-based tomography, some inversion experiments will be presented. Synthetic data is used to have full control over the ex-

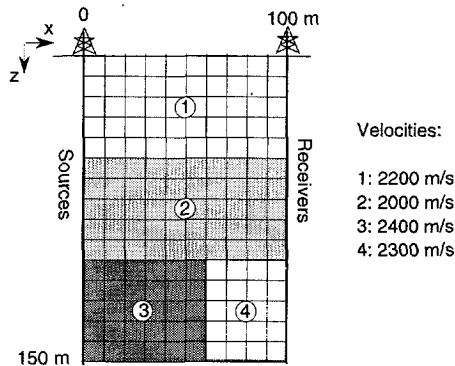


Fig. 2.4 The four-area model with 150 cell parameters. There are 900 rays shot through this model. Velocities are indicated, but slownesses are used in the inversion.

periments. The original model that is used is shown in Figure (2.4). It has three layers, with the bottom layer consisting of two parts. In the figure velocities are given for clarity, but actually slownesses are used. The model is discretized using 10x15 square cells of 10x10 m, resulting in a total of 150 parameters. On the left side of the model 30 sources are placed. For each shot, straight rays are traced from left to right into 30 geophones placed on the right side. Both the first shot and receiver are positioned at 2.5 m in depth. The array spacing is 5 m. As the data is computed with the same straight ray assumption as is used in the inversion, the inversion is exact. This is desirable because in this case the inversion results will exhibit the highest overall accuracy possible, excluding nonlinear effects like ray-bending. Summarized, the following procedure is used:

- Compute synthetic data.
- Optional: add Gaussian noise to synthetic data.
- Compute the a posteriori covariance matrix, which is the inverse of $(\mathbf{A}^T \mathbf{C}_n^{-1} \mathbf{A} + \mathbf{C}_x^{-1})$, using a singular value decomposition. If \mathbf{C}_x^{-1} is small or absent (MLE), discard the singular values that are near the floating point precision of the computer. In the examples the values below 10^{-14} times the maximum singular value are discarded. For MAP estimation, this is not needed because the matrix is not singular.
- Using this inverse, compute the full solution of equation (2.49) or (2.51).
- Compute the correlation matrix.

For six shots the traveltimes with and without noise are shown in Figure 2.5 (a) and (b) respectively. The standard deviation of the Gaussian noise is 0.5 ms. Note that this corresponds to about 1/4 of a wavelength at 500 Hz.

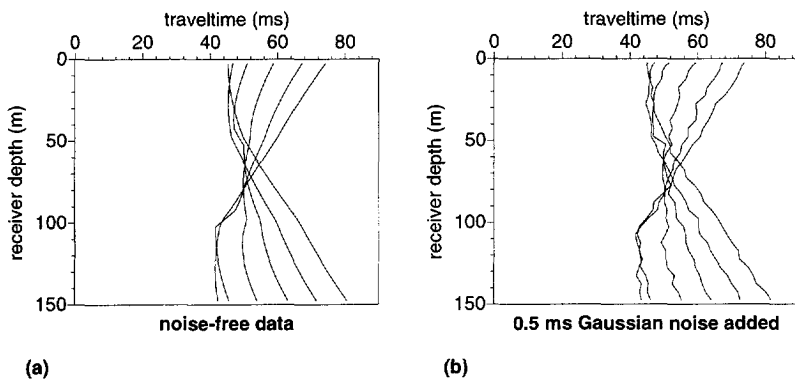


Fig. 2.5 Traveltime graphs of 6 shots, depth range from 2.5 m to 127.5 m, spaced 25 m. (a) Without noise. (b) Gaussian noise added with a standard deviation of 0.5 ms. The receiver sampling actually is 5m; the points are connected by straight lines.

Maximum Likelihood Estimation

For the first example, Gaussian noise with a standard deviation of 0.5 ms is assumed to be present on the traveltime data, but no noise is actually added to the data. During the maximum likelihood inversions, 8 singular values out of the 150 have been discarded, due to their low values. The results of the inversion using ML estimation can be found in Figure 2.6. Graphs (a) and (b) visualize the estimated model using the inverse of the estimated slowness. In Figure 2.6.c, the a posteriori standard deviation is visualized. For one cross-section at 45 m, the 95% uncertainty

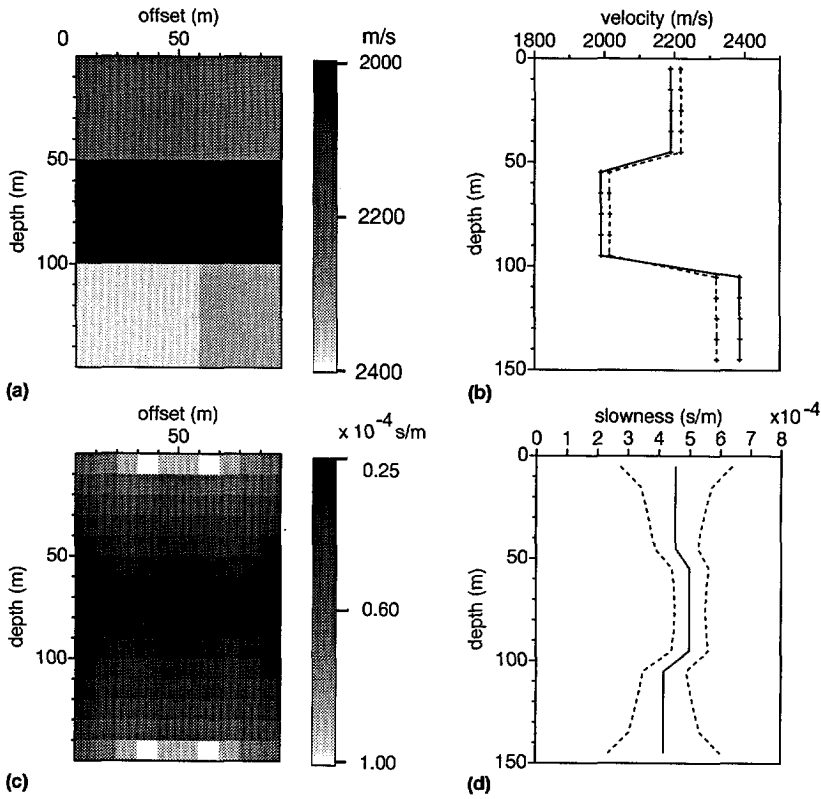


Fig. 2.6 ML estimation results. No noise is actually added to the traveltimes. (a) Inverted a posteriori slownesses. (b) Vertical cross-sections through (a) at $x=25\text{ m}$ and $x=75\text{ m}$ (dashed). (c) A posteriori slowness standard deviations. (d) True model and 95% uncertainty interval at a cross-section of 45 m.

intervals around the true model are indicated in Figure 2.6.d. The intervals are defined by adding $\pm 2\sigma$ to the a posteriori slowness model, with σ the a posteriori standard deviation.

A remarkable effect is observed. The “step” along the horizontal direction of 2400-2300 m/s in the lower layer is imaged, although the estimated velocity is about 50 m/s too high. But the presence of this contrast in the lower layer results in a step of about 50 m/s in the upper two layers too, aligned along the depth direction. The velocity is about 50 m/s too high in that area. This suggests a strong correlation in the z -direction, which indeed is the case, as will be shown later in this section.

Now the inversion is repeated with the noise-contaminated data. Figure 2.7 shows the results

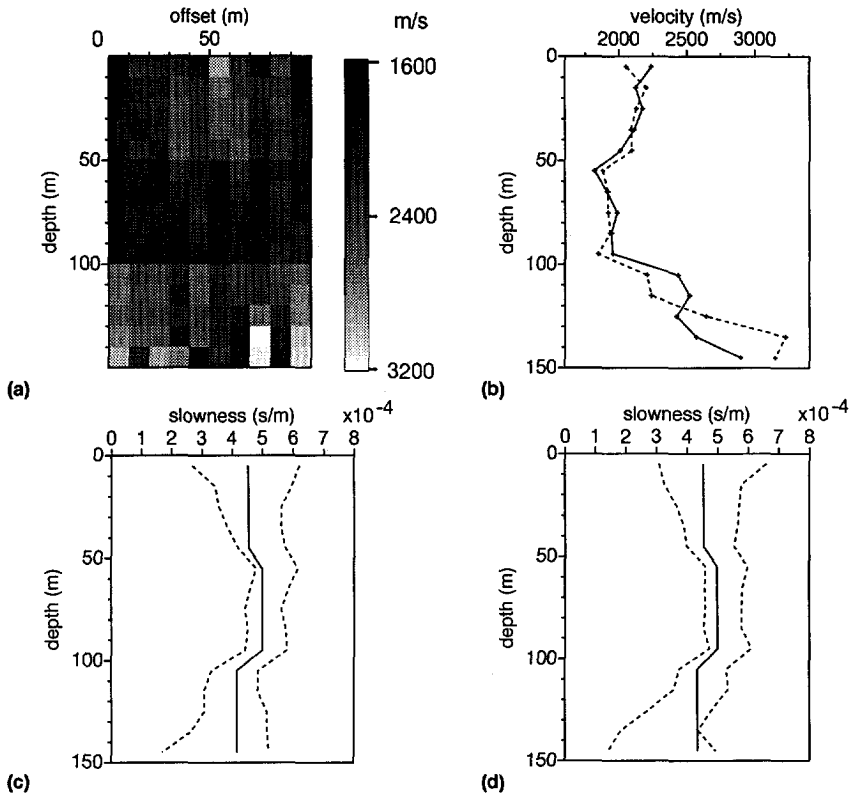


Fig. 2.7 ML estimation results with noisy data. (a) Inverted a posteriori slownesses. (b) Vertical cross-sections through (a) at $x=25$ m and $x=75$ m (dashed). (c) True model and 95% uncertainty interval at a cross-section of 25 m. (d) True model and 95% uncertainty interval at a cross-section of 75 m.

of the a posteriori model and the a posteriori standard deviations.

For these examples it may be concluded that if the traveltimes are contaminated by noise, it is not possible to obtain a good estimate. Therefore, some kind of additional information must be used to stabilize the solution. As was outlined in the previous section, Bayesian estimation techniques provide a consistent way of incorporating this a priori knowledge. Next, an example of Bayesian estimation with the same model and data is presented.

Bayesian estimation

Again the model of Figure 2.4 is used, with the same acquisition configuration and the same data. In addition it is now assumed that the slowness is known to be $(4.545 \pm 0.681) \cdot 10^{-5}$ s/m,

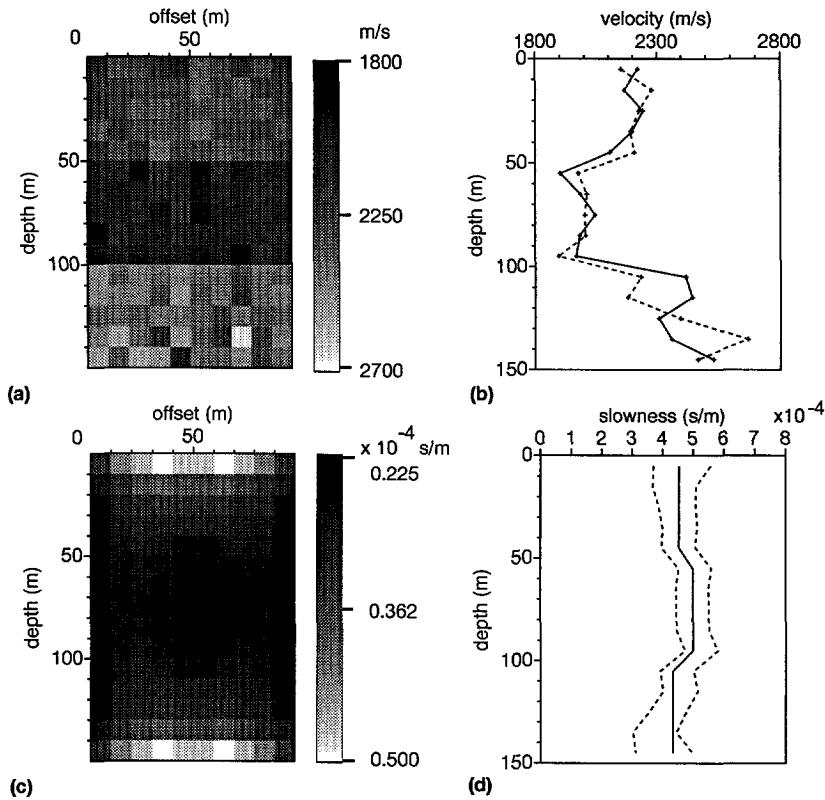


Fig. 2.8 Bayesian estimation results with noisy data. (a) inverted a posteriori slownesses. (b) Vertical cross-sections through (a) at $x=25$ m and $x=75$ m (dashed). (c) a posteriori standard deviations. (d) true model (straight line) and 95% uncertainty interval (dashed lines) for a cross-section at 75 m.

which equals $(1/2200)$ s/m with a standard deviation of 15%. Results of performing the inversion using equation (2.49) can be found in Figure 2.8. Figure 2.8.a shows the inverted a posteriori slownesses, Figure 2.8.b a cross-section through the inverted slownesses, Figure 2.8.c the a posteriori standard deviations and Figure 2.8.d a cross-section through the a posteriori slownesses.

Compared to the maximum likelihood example, it may be concluded that the results are more accurate in the regions where the ML estimator failed most. This is at the top center and bottom center of the model, where there is less ray coverage. There the a priori information takes over and the standard deviation is tending towards the a priori standard deviation. Still, the different layers can hardly be distinguished, because the noisy detail blurs the interface positions.

It may be concluded that the cell-based travelttime tomography technique gives inaccurate estimates if no a priori information is available. In the presence of noise on the data, 900 data points are not enough to estimate 150 parameters accurately. The addition of accurate a priori knowledge is mandatory for obtaining an accurate inversion result.

The a posteriori correlation matrix

One of the tools to inspect inversion results is the correlation matrix, which describes the interdependence of the estimated parameters. For the four-area model the correlation matrix consists of 150x150 entries. It is thus difficult to visualize the whole matrix in one picture. A convenient solution is to look at one column at the time. This shows the correlation of one parameter with all other parameters. Figure 2.9 shows four entries of the correlation matrix for the parameter at the cells centered at $(x,z)=(5,75)$ m, $(5,35)$ m, $(45,75)$ m and $(45,35)$ m (from left to right).

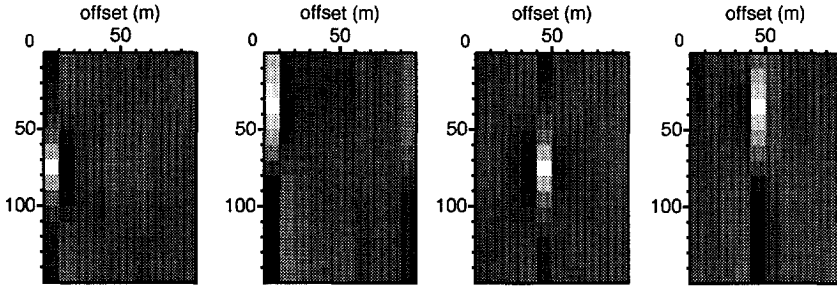


Fig. 2.9 Four entries of the correlation matrix. Black corresponds to a correlation of -0.8 , and white to a correlation of $+1$.

For all four plots, a negative correlation with the neighboring parameters along the horizontal direction exists. Overall, a high mutual correlation between parameters in the same region of the grid is present. It is surprising that the correlation between parameters in the vertical direction is higher than that of parameters in the horizontal direction. If the rays were mainly along the horizontal direction, the opposite would be expected. An explanation for the high vertical correlations is that, in this case, a lot of rays are crossing the model under high angles. This effect also causes the step anomaly observed in the homogeneous upper and middle layers of Figure 2.6.

2.4 Sparse macro velocity model based travelttime tomography

For all parameter estimation problems it is important to realize that if more parameters must be estimated using the same amount of data, then the estimated parameters become less accurate.

Therefore, a model representation is chosen that will yield a macro velocity model for the migration step and which explains the data with preferably as few parameters as possible. With the traditional cell representation of the previous section, hundreds of parameters are estimated at once, with a relatively low accuracy for each parameter. These large numbers of parameters are needed because the cell method aims at resolving all the detail of the subsurface. However, a macro velocity model does not have to be that detailed, because the detail is imaged in the later migration step. By using more a priori knowledge, the number of parameters in the model can be decreased. If certain geometric or material properties of the subsurface are known, this knowledge can be included in the model description. For example, if from the well-logs a specific layered structure can be assumed, the forward macro model can be build up with layers. Note again that in practice there will always be a priori knowledge available on the local structure and geology around a well-site.

2.4.1 Forward macro model representation

In this section a geologically oriented subsurface macro model for crosswell applications is proposed that employs a boundary-type of parameterization. The boundaries between major geological volumes or areas can be parameterized by spline functions, sine expansions or polynomials. Over the last years, a number of references to surface seismic traveltime inversion methods can be found in the geophysical literature that adopt this concept. Examples are Chiu and Stewart (1987), Van der Made (1988) and Scheffers (1993). Bishop et al. (1985) use cubic spline functions to parameterize reflector depth, but also overlay their model with a gridded velocity field. The crosswell application of the boundary-type macro velocity model has been introduced by Giling et al. (1992).

For the crosswell case the model space is two-dimensional. Therefore, a one-dimensional description of the boundaries suffices. Hermitian polynomials are chosen, because they are especially suited for traveltime inversion. The major advantage of polynomials is that derivatives of the traveltimes to the model parameters, which are needed in the inversion, can be computed analytically. Opposed to using less accurate numerical derivatives, this will yield a better convergence speed and a more stable inversion process.

Figure 2.10 shows the parameterization of the crosswell macro velocity model using third order Hermitian polynomials. Consider an interface with L node points and $L - 1$ segments. The interface is parameterized according to either

$$\begin{cases} z_j(u) = a_{0,j} + a_{1,j}u + a_{2,j}u^2 + a_{3,j}u^3 \\ x_j(u) = c_{0,j} + c_{1,j}u \end{cases} \quad (2.54)$$

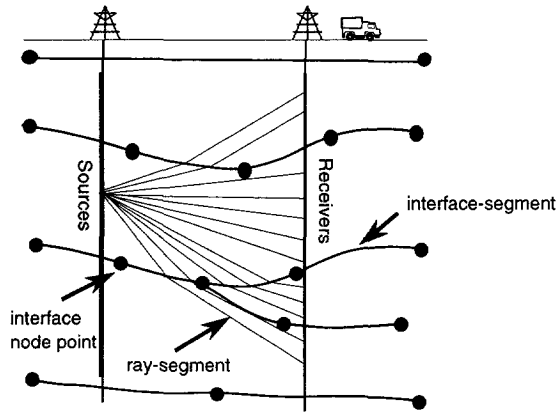


Fig. 2.10 Impression of a sparse crosswell macro velocity model parameterized with polynomial boundaries.

or

$$\begin{cases} z_j(u) = c_{0,j} + c_{1,j}u \\ x_j(u) = a_{0,j} + a_{1,j}u + a_{2,j}u^2 + a_{3,j}u^3 \end{cases} \quad (2.55)$$

where $0 \leq u < 1$ and $j \in \{1, 2, \dots, L-1\}$. With these choices, there is always one of the two coordinates x, z that has only one degree of freedom, which means it has a constant sampling interval along the interface. Parameterization (2.54) is used for near horizontally oriented interfaces, and (2.55) is used for near vertically oriented interfaces, such as faults and unconformities. At the edges of each segment it is assured that the spatial derivative equals the spatial derivative of the neighboring segment. For details on how to compute the coefficients a_{ij} and c_{ij} see Van der Made (1988) and Scheffers (1993).

Apart from geometry parameters that describe the structure, velocity parameters are introduced for the compressional and shear wave velocities in the enclosed areas. Although the velocity field within the boundaries can be parameterized in a general manner, for example using polynomials or gridding (cells), and even anisotropy may be taken into account, in this thesis a constant velocity is taken. This yields the lowest number of parameters possible.

2.4.2 Ray-tracing

Since the velocity field is assumed to be homogeneous in each enclosed area, the direct-wave raypath from source to receiver consists of straight ray segments. Over the interfaces, Snell's law must be obeyed and the ray is kinked. This is also visualized in Figure 2.10 for one shot

with a number of receivers.

For the ray-tracing procedure a combination of “shooting” and “bending” is used. Shooting means that from each source a fan of rays is shot, and rays passing close to a particular receiver are assumed to belong to that receiver. Snell’s law is explicitly used when shooting. The subsequent bending step modifies the rays by assuring that all rays describe minimum time paths. This means that the ray must be stationary, which is accomplished by disturbing the initial ray-path in such a way that the derivative of the traveltimes with respect to all model parameters is minimized. A steepest descent algorithm is used to minimize the derivative, which is described by Guiziou and Haas (1988). In the bending step, Snell’s law is implicitly obeyed.

Due to the discrete number of rays in the initial ray fan there can still be source-receiver pairs for which a ray has not been found. Therefore, the computed rays can be interpolated and extrapolated to nearby sources and receivers for which a ray has not been found yet. This procedure has proved to be efficient with respect to computation time; in the expensive shooting step it is not necessary to find all raypaths at once.

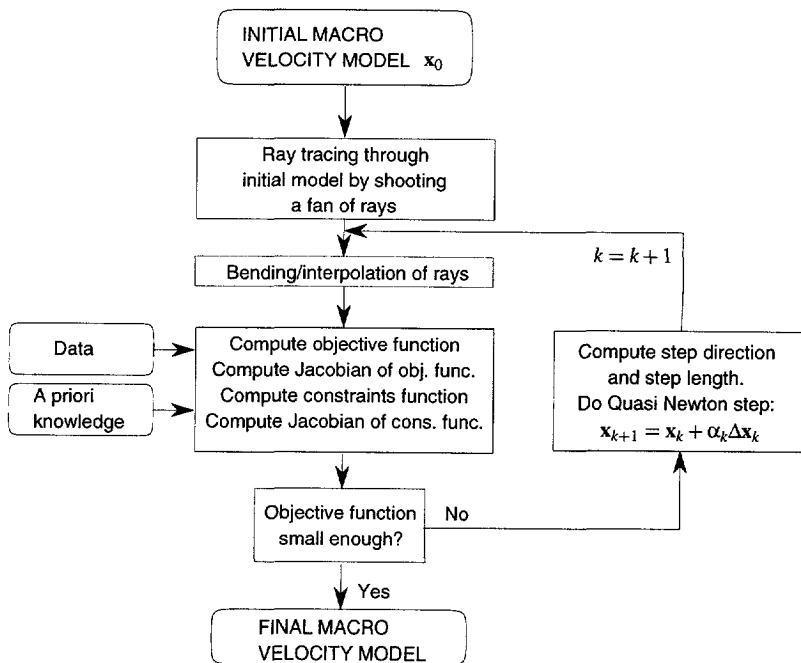


Fig. 2.11 Flowchart of the nonlinear iterative constrained inversion procedure using the boundary-type of parameterization

2.4.3 Nonlinear optimization and inversion

All geometry and velocity parameters are stored in the parameter vector \mathbf{x} and the picked travel-time data is stored in a vector \mathbf{d} . Using Bayesian inversion, the MAP point estimate follows from the minimization of objective function (2.27) on page 25. The forward model $\mathbf{g}(\mathbf{x})$ is nonlinear both in the velocity and geometry parameters. Instead of a closed form solution, an iterative solution method must be used, as has been discussed in section 2.2. In addition, for complex structures containing for example faults, pinch-outs or unconformities, linear and nonlinear boundary conditions must be included (Scheffers (1993)). Figure 2.11 shows the flowchart along which the nonlinear constrained inversion is carried out. In the kernel a Quasi-Newton algorithm is employed to minimize the objective function. In the implementation a routine from the NAG numerical library has been used (routine number E04UCF, NAG (1990)).

The expensive shooting procedure is only performed once. However, for complicated macro models it may be necessary to carry out the shooting more than once because of ray-paths becoming infeasible during inversion. This is the case if, for example, a transmitted ray does not exist anymore due to post-critical reflection. Or if an interface is shifted over a large distance and the rays crossing the interface are not feasible anymore. Reshooting is also necessary when interfaces that are crossing the source and receiver arrays are shifted along the arrays, causing some sources or receivers to lay in different areas over subsequent iterates.

As has been mentioned before, an advantage of the type of model definition is that the Jacobian can be computed analytically. This is not feasible for the cell model used in section 2.3, where an approximation of the Jacobian by keeping the raypaths fixed has been used instead.

When crosswell direct-wave traveltime inversion is compared to surface reflection traveltime inversion, a major difference is that for a reflection inversion all events from the reflectors can be treated separately (recursive estimation by layer stripping). This makes the inversion more robust. For transmission data using first arrivals only, all data must be used in one inversion procedure and all parameters are estimated at the same time. For the latter case it is more likely that the minimization procedure converges to a local minimum.

2.4.4 Nonlinear model driven inversion examples

Although it has been indicated that using slowness parameters instead of velocity parameters makes the forward model more linear, in the examples of this section velocity parameters are used. This has the advantage that a priori information on the velocities, which is described by Gaussian distributions, can readily be incorporated. Furthermore, an a posteriori accuracy and resolution analysis can be carried out directly using velocities and thus results can more easily be interpreted. To check the convergence and results of the inversion procedure, an experiment may be repeated using slownesses. The results may then be compared with the initial inversion results. From experience it is known that, for the examples presented in this chapter, the

inversion results obtained using slowness parameters are consistent with the inversion results obtained using velocity parameters.

Two examples are presented here: the estimation of a faulted layer macro velocity model and the estimation of a macro velocity model containing a flood front. Synthetic traveltimes are computed through the “real” model and noise is added to the traveltimes. The synthetic data is then inverted. Real data examples can be found in Chapter 5.

Faulted layer macro model

Figure 2.12 shows the real model, a priori model and estimated model results for a three-layer macro velocity model. In real life the true model would not be known, but it is assumed that the middle layer contains a fault. The goal is to estimate the velocity of the four different areas and the position of the fault. Because the fault plane is assumed to be flat its position is parameterized by the position of the two end points along the horizontal (x) axis. The number of parameters to be estimated thus is 6. Synthetic data is generated using the real model. Gaussian noise with a standard deviation of 0.5 ms is added to the traveltimes. This corresponds to 1/4 of a wavelength at 500 Hz. Six shot positions are used with 29 receivers per shot giving a maximum of 174 travelttime data points. However, some rays could not be found due to shadow zones leaving a total of 169 rays and thus 169 data points. The total travelttime mismatch (the summed absolute travelttime mismatch over all data points) is 536 ms, which is 3.2 ms per ray on the average.

As is shown in the middle table of Figure 2.12, the a priori model contains relatively moderate information on the parameters. The strongest a priori information consists of the geological structure itself. This knowledge must come from other available sources, as has been explained previously. The total a priori model layer is taken homogeneous, but a vertical fault is inserted in the middle layer. In practice a decision to alter the structure (by inserting layers or faults) can be made if after the inversion the travelttime residuals can not be made small enough.

The inversion is done in two steps. In the first step, the initial model is taken equal to the a priori model. Then a complete re-shooting and bending is performed and the inversion is repeated with the initial model equal to this re-traced model. Note again that in the actual inversion loop, only ray bending is used. The a priori information is of course not altered in this second run. After inversion, the total travelttime mismatch has decreased to 65 ms (0.40 ms per ray on the average). The final model is shown in the bottom row of Figure 2.12 with the parameters and corresponding standard deviations displayed in the table. It can be concluded that the velocity parameters are estimated with high accuracy while the position of the fault is estimated less accurately. When interpreting the results it must be realized that the estimated parameters are not independent. Also, the computed standard deviations are those of a *multivariate* Gaussian distribution. Therefore it is useful to inspect the full a posteriori correlation matrix, as is given in Table 2.1 on page 45. Note the strong anti-correlation between x_1 and x_2 . Furthermore, only the velocity in the top layer is estimated relatively independent from the position of the fault.

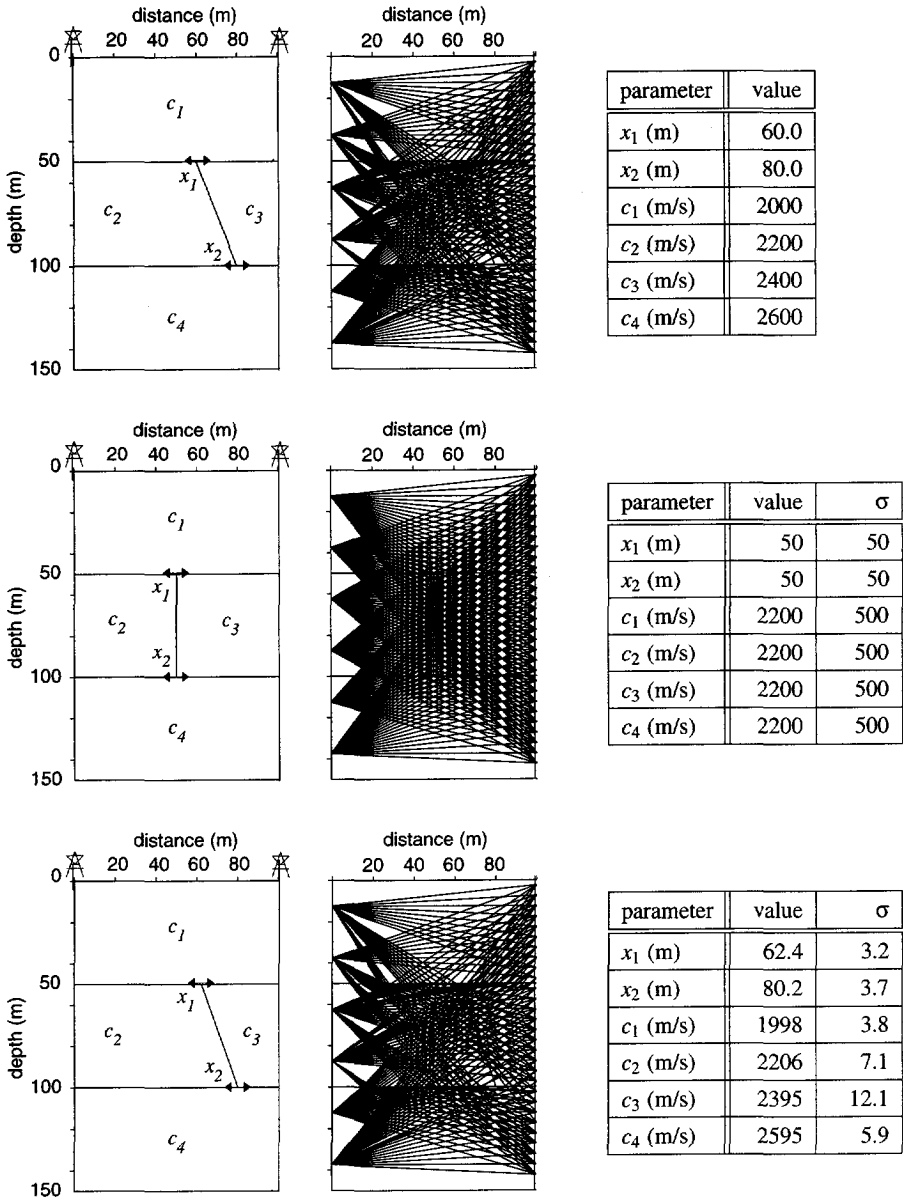


Fig. 2.12 Traveltime inversion example with faulted layer model. Top row: real model; Middle row: a priori model (=start model); Bottom row: estimated model. There are two free geometric parameters (indicated by the arrows) and four velocity parameters. The standard deviation on the parameters is given by σ . Both the models with and without rays are shown.

Table 2.1 *A posteriori correlation matrix for the fault model*

	x_1	x_2	c_1	c_2	c_3	c_4
x_1	1.000	-0.492	0.058	0.201	0.136	-0.198
x_2	-0.492	1.000	0.025	0.270	-0.135	-0.167
c_1	0.058	0.025	1.000	-0.114	-0.196	-0.005
c_2	0.201	0.270	-0.114	1.000	-0.390	-0.379
c_3	0.136	-0.135	-0.196	-0.390	1.000	-0.086
c_4	-0.198	-0.167	-0.005	-0.379	-0.086	1.000

Macro model with flood front

A second experiment is done in which it is attempted to estimate a macro velocity model containing a CO₂ flood front after gas injection in a well. The real model is shown at the top of Figure 2.13. It has a three-layer shale/oil-sand/shale - like structure, with large ($\approx 25\%$) velocity contrasts between the layers. In the middle layer a velocity contrast ($\approx 10\%$) is present due to the injection from the left well. Although in a real flood front small-scale fingering effects may be present, in this example only the “envelope” of the flood-front is considered. The same acquisition as for the previous model is used: six shot positions with 29 receivers per shot. Synthetic data is computed and Gaussian noise is added with a standard deviation of $\sigma = 0.5$ ms.

For the initial model again the same constant velocity $c = 2200$ m/s is assumed as for the previous example (see middle row of Figure 2.12). But the flood front is parameterized by four positional parameters. So compared to the previous example, there are more parameters, and because of the curved flood-front and the higher velocity contrasts the problem is more nonlinear. The actual inversion is done in two steps: first the velocities are estimated by keeping the initial vertical flood front fixed, and second the positional (geometric) parameters x_i are relaxed. This finally yields the results displayed at the bottom of Figure 2.13. In addition to the velocity parameters, x_2 and x_3 are well resolved. The top and bottom of the flood front can not be estimated accurately, because relatively few rays travel through these parts of the flood front.

Table 2.2 shows the a posteriori correlation matrix for the flood front model experiment. Note the relatively strong anti-correlation between c_2 and c_4 . Furthermore, the smallest correlations (less than 0.03) are between x_3, x_4 and between x_3, c_1 . Considering the two velocity parameters at the left and right of the flood front, parameter c_2 is more correlated with the position of the flood front than parameter c_3 .

Final remarks

The examples show the potential of the proposed crosswell travelttime inversion method. Although it is well known that for crosswell tomography it can be problematic to obtain sufficient horizontal resolution, it has been shown that, for the sample experiments, with a geologically oriented type of parameterization, the position of (near) vertically oriented boundaries can be estimated with reasonable accuracy.

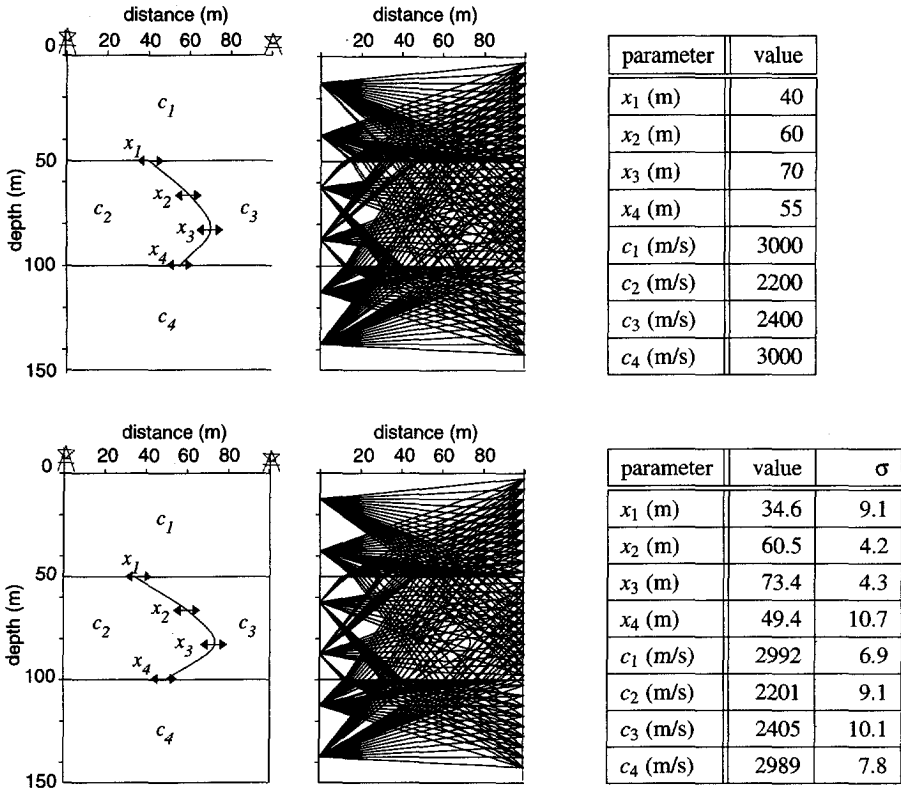


Fig. 2.13 Traveltime inversion example with flood front model. Top: real model; Bottom: estimated model. There are four free geometric parameters (indicated by the arrows) and four velocity parameters. The standard deviation on the estimated parameters is given by σ .

Table 2.2 A posteriori correlation matrix for the front flood model

	x_1	x_2	x_3	x_4	c_1	c_2	c_3	c_4
x_1	1.000	-0.172	0.259	0.071	0.037	0.332	-0.161	-0.175
x_2	-0.172	1.000	-0.062	0.220	-0.164	0.353	-0.102	-0.284
x_3	0.259	-0.062	1.000	0.029	-0.018	0.383	-0.045	-0.224
x_4	0.071	0.220	0.029	1.000	-0.790	0.379	-0.263	-0.122
c_1	0.037	-0.164	-0.018	-0.079	1.000	-0.105	-0.331	0.057
c_2	0.332	0.353	0.383	0.379	-0.105	1.000	-0.387	-0.518
c_3	-0.161	-0.102	-0.045	-0.026	-0.331	-0.387	1.000	0.096
c_4	-0.175	-0.284	-0.224	-0.122	0.057	-0.518	0.096	1.000

Chapter 3

Crosswell migration using wavefield extrapolation

After determination of a macro velocity model from first arrival traveltimes, the scattered waves in the received wavefield are used to resolve detailed structural information. This step is called the *wavefield imaging* step. Analogous with the surface seismic approach, this step may also be called *depth migration*, where events recorded in time are “migrated” to their correct positions in the space domain. Note that in this thesis the term “migration” must be read as “depth migration”, and must not be confused with so-called “time migration” techniques.

Apart from imaging diffracted waves, the main goal in the migration step is to image *reflectivity*. As has been explained in Chapter 1, in contrast to seismic *inversion* methods that aim at resolving velocity or density fields, seismic *migration* aims to resolve the reflectivity information of the subsurface. For surface reflection data, one-way wave theory is especially suited for developing such a migration scheme. Therefore, in this chapter one-way wave theory is used at the basis of the crosswell migration scheme.

In this thesis, scalar one-way wave theory is used, applicable to the migration of compressional waves (P-waves). The theory may also be adapted for the migration of shear waves (S-waves). If shear waves can be isolated from the total wavefield, a shear wave macro velocity model can be estimated and a shear wave migration can be attempted, again using the scalar wave equation. However, the migration of shear wave or full elastic data is beyond the scope of this thesis.

3.1 Representation of crosswell seismic data

3.1.1 Conceptual model

The conceptual model of crosswell seismic wave propagation and scattering is sketched in Figure 3.1. A downhole *source* S emits acoustic waves into the formation. One part of the radiated

source waves *propagates* (**W**) towards inhomogeneities such as reflectors, and *interacts* with those inhomogeneities, indicated by the symbol Θ . Then, the scattered wavefield is again *propagating* (**W**) towards the receiver well and *detected* by the downhole receivers (**P**). Another part of the wavefield propagates directly from the source towards the receivers and is called the primary wave.

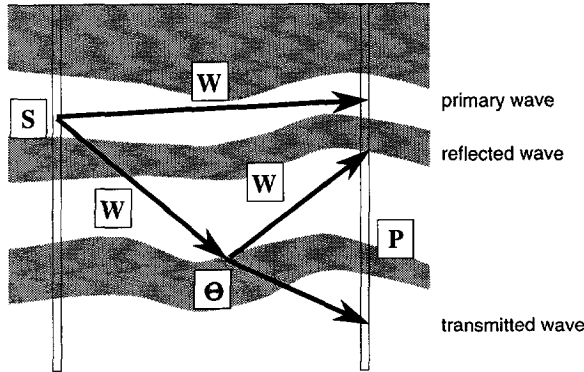


Fig. 3.1 The conceptual model for crosswell seismic wave propagation. **S** denotes the source wavefield, **W** denotes propagation, Θ interaction and **P** is the detected wavefield.

To develop a crosswell wavefield imaging scheme, this model must be inverted in such a way that the interaction quantity Θ can be extracted and visualized. This means that first the propagation effects **W** must be removed, and then the interactions can be imaged. The interaction quantity Θ contains both transmission and reflection effects, which must be treated separately. In the following sections, a theoretical basis is given to this conceptual model, and subsequently a solution to the inverse problem is presented.

3.1.2 One-way wave equation

In this section the one-way wave equation is derived in the angular frequency domain. Use is made of the Fourier transform pair

$$F(\omega) = \int_{-\infty}^{+\infty} f(t) e^{-j\omega t} dt \quad (3.1)$$

$$f(t) = \frac{1}{\pi} \text{Re} \left[\int_0^{+\infty} F(\omega) e^{j\omega t} d\omega \right], \quad (3.2)$$

where ω is the angular frequency, t denotes time, $f(t)$ is a real valued function, and the imaginary unit j is defined as $j^2 \equiv -1$.

The following form of the two-way acoustic wave equation in the angular frequency domain is used as a starting point:

$$\frac{\partial \mathbf{Q}}{\partial z} - \hat{\mathbf{A}} \mathbf{Q} = \mathbf{D}. \quad (3.3)$$

In this matrix equation, the wave vector $\mathbf{Q}(\mathbf{x})$ and the source vector $\mathbf{D}(\mathbf{x})$ are given by

$$\mathbf{Q} = \begin{pmatrix} P \\ V_z \end{pmatrix}, \quad \mathbf{D} = \begin{pmatrix} F_z \\ I - \frac{1}{j\omega} \left[\frac{\partial}{\partial x} \left(\frac{1}{\rho} F_x \right) + \frac{\partial}{\partial y} \left(\frac{1}{\rho} F_y \right) \right] \end{pmatrix} \quad (3.4)$$

where $P(\mathbf{x})$ denotes the acoustic pressure, $V_z(\mathbf{x})$ denotes the vertical component of the particle velocity, I denotes the volume source density of volume injection rate, $\rho(\mathbf{x})$ is the volume density of mass and F_x, F_y, F_z denote the components of the volume source density of volume force. Vector \mathbf{x} denotes the Cartesian coordinate vector (x, y, z) . For notational convenience, the angular frequency variable ω is suppressed. The operator matrix $\hat{\mathbf{A}}(\mathbf{x})$ is defined as

$$\hat{\mathbf{A}} = \begin{pmatrix} 0 & -j\omega\rho \\ -\frac{j\omega}{K} + \frac{1}{j\omega} \left[\frac{\partial}{\partial x} \left(\frac{1}{\rho} \frac{\partial}{\partial x} \cdot \right) + \frac{\partial}{\partial y} \left(\frac{1}{\rho} \frac{\partial}{\partial y} \cdot \right) \right] & 0 \end{pmatrix} \quad (3.5)$$

with compression modulus $K(\mathbf{x})$. The hat ($\hat{\cdot}$) denotes operators containing the horizontal differentiation operators $\partial/\partial x$ and $\partial/\partial y$.

Now a one-way wave vector $\mathbf{P}(\mathbf{x})$ and a one-way source vector $\mathbf{S}(\mathbf{x})$ are introduced according to

$$\mathbf{P} = \begin{pmatrix} P^+ \\ P^- \end{pmatrix} \quad \text{and} \quad \mathbf{S} = \begin{pmatrix} S^+ \\ S^- \end{pmatrix}. \quad (3.6)$$

$P^+(\mathbf{x})$ and $P^-(\mathbf{x})$ represent waves traveling in the $+z$ and $-z$ direction, respectively. Similarly, $S^+(\mathbf{x})$ and $S^-(\mathbf{x})$ represent the sources for waves traveling in the $+z$ and $-z$ direction respectively. The direction along which a two-way wavefield is decomposed into two one-way wavefields is called the *principal direction of one-way wave propagation* or, in short, “the principal direction”. In this thesis, the z coordinate axis is taken parallel to the principal direction. Although in the seismic practice the z -axis is commonly chosen to point downwards (in depth), this choice is not mandatory. But for now let the z -axis be the (vertical) depth axis. Thus, a “+” sign denotes “downward” and a “-” sign denotes “upward” propagation.

For a homogeneous medium, the downgoing wavefield P^+ and the upgoing wavefield P^- propagate independently, obeying the one-way wave equation

$$\frac{\partial \mathbf{P}}{\partial z} + j\omega \hat{\mathbf{A}} \mathbf{P} = \mathbf{S}, \quad (3.7)$$

with $\hat{\mathbf{A}}$ the vertical slowness operator matrix, which is a diagonal matrix. For general continuous inhomogeneous media the goal is to find an expression similar to (3.7), with the propagation still described by a diagonal operator matrix. The operator matrix $\hat{\mathbf{A}}$ is decomposed according to

$$\hat{\mathbf{A}} = -j\omega \hat{\mathbf{L}} \hat{\mathbf{\Lambda}} \hat{\mathbf{L}}^{-1} \quad (3.8)$$

in such a way that $\hat{\mathbf{\Lambda}}$ is indeed diagonal. In this decomposition, which is closely related to an eigenvalue decomposition, the operator matrices $\hat{\mathbf{L}}$, $\hat{\mathbf{\Lambda}}$ and $\hat{\mathbf{L}}^{-1}$ have the following structure:

$$\hat{\mathbf{L}} = \begin{pmatrix} \hat{L}_1 & \hat{L}_1 \\ \hat{L}_2 & -\hat{L}_2 \end{pmatrix}, \quad \hat{\mathbf{\Lambda}} = \begin{pmatrix} \hat{\Lambda} & 0 \\ 0 & -\hat{\Lambda} \end{pmatrix} \quad \text{and} \quad \hat{\mathbf{L}}^{-1} = \frac{1}{2} \begin{pmatrix} \hat{L}_1^{-1} & \hat{L}_2^{-1} \\ \hat{L}_1^{-1} & -\hat{L}_2^{-1} \end{pmatrix}. \quad (3.9)$$

The operator matrices $\hat{\mathbf{L}}$, $\hat{\mathbf{\Lambda}}$ and $\hat{\mathbf{L}}^{-1}$ are pseudo-differential operators which depend implicitly on the horizontal differential operators $\partial/\partial x$ and $\partial/\partial y$. A thorough discussion on the usage of these operators in seismic wave theory can be found in Wapenaar and Berkhout (1989) and De Hoop (1992). Using (3.8) in the two-way expression (3.3) yields

$$\hat{\mathbf{L}}^{-1} \frac{\partial \mathbf{Q}}{\partial z} + j\omega \hat{\mathbf{\Lambda}} \hat{\mathbf{L}}^{-1} \mathbf{Q} = \hat{\mathbf{L}}^{-1} \mathbf{D}. \quad (3.10)$$

By comparing this result to the one-way wave equation for homogeneous media (3.7), it is suggested to define \mathbf{P} and \mathbf{S} as

$$\mathbf{P} = \hat{\mathbf{L}}^{-1} \mathbf{Q} \quad \text{and} \quad \mathbf{S} = \hat{\mathbf{L}}^{-1} \mathbf{D}. \quad (3.11)$$

The meaning of the $\hat{\mathbf{L}}$ operator now becomes clear: $\hat{\mathbf{L}}$ is a *composition* operator, while $\hat{\mathbf{L}}^{-1}$ is a *decomposition* operator. Using definitions (3.11) in equation (3.10) finally yields the one-way wave equation, according to

$$\frac{\partial \mathbf{P}}{\partial z} - \hat{\mathbf{B}} \mathbf{P} = \mathbf{S}, \quad (3.12)$$

where the one-way operator matrix $\hat{\mathbf{B}}$ is defined as

$$\hat{\mathbf{B}} = -j\omega \hat{\mathbf{\Lambda}} + \hat{\mathbf{\Theta}}, \quad (3.13)$$

with

$$\hat{\mathbf{\Theta}} = -\hat{\mathbf{L}}^{-1} \frac{\partial \hat{\mathbf{L}}}{\partial z}. \quad (3.14)$$

The interaction operator matrix $\hat{\mathbf{\Theta}}$ is defined to have the structure

$$\hat{\mathbf{\Theta}} = \begin{pmatrix} \hat{T}^+ & \hat{R}^- \\ -\hat{R}^+ & -\hat{T}^- \end{pmatrix} \quad (3.15)$$

where

$$\hat{R}^+ = -\hat{R}^- = +\frac{1}{2} \left(\hat{L}_1^{-1} \frac{\partial \hat{L}_1}{\partial z} - \hat{L}_2^{-1} \frac{\partial \hat{L}_2}{\partial z} \right) \quad (3.16)$$

and

$$\hat{T}^+ = -\hat{T}^- = -\frac{1}{2} \left(\hat{L}_1^{-1} \frac{\partial \hat{L}_1}{\partial z} + \hat{L}_2^{-1} \frac{\partial \hat{L}_2}{\partial z} \right). \quad (3.17)$$

The \hat{R}^\pm operators account for the interaction between wavefields that have opposite propagation directions (P^\pm with P^\mp). Thus, the \hat{R}^\pm operators are identified as *reflection* operators. Similarly, as the \hat{T}^\pm operators describe the coupling between wavefields with the same propagation direction (P^\pm with P^\pm) they are identified as *transmission* operators.

Both $\hat{\Theta}$ and $-j\omega\hat{\Lambda}$ account for scattering due to medium variations along the horizontal plane. But the scattering along the principal direction (the z -axis), and thus the coupling of the upgoing and downgoing wavefields along the principal direction is only described by the interaction matrix $\hat{\Theta}$. The operator $-j\omega\hat{\Lambda}$ accounts for the propagation along the vertical axis. Table 3.1 summarizes which operators account for propagation, scattering along the horizontal plane (“scattering $\partial/\partial x, \partial/\partial y$ ”) and scattering along the vertical axis (“scattering $\partial/\partial z$ ”).

Table 3.1 Interpretation of the operators $\hat{\Lambda}$ and $\hat{\Theta}$.

	$\hat{\Lambda}$	$\hat{\Theta}$
propagation	X	
scattering $\partial/\partial x, \partial/\partial y$	X	X
scattering $\partial/\partial z$		X

In the case of a (near-) horizontally layered medium, which is reasonable to assume in crosswell seismic exploration, it follows that in the one-way wave equation (3.12) the factor $-j\omega\hat{\Lambda}$ mainly accounts for the *propagation* effects, while the term $\hat{\Theta}$ mainly accounts for all the *scattering* effects.

3.1.3 One-way representation

Using the one-way wave equation, a representation for the one-way wave field can now be derived to be used for the migration of seismic data. First, choose a reference operator $\hat{\mathbf{B}}$, which defines a one-way Green’s matrix $\hat{\mathbf{G}}(\mathbf{x}, \mathbf{x}')$, according to the one-way wave equation

$$\frac{\partial \hat{\mathbf{G}}}{\partial z} - \hat{\mathbf{B}}\hat{\mathbf{G}} = \underbrace{\mathbf{I}\delta(\mathbf{x} - \mathbf{x}')}_{\text{'point source'}}. \quad (3.18)$$

The 'bar' over the operator $\hat{\mathbf{B}}$ denotes that it is a reference operator. The Green's matrix has the following structure

$$\underline{\mathbf{G}}(\mathbf{x}, \mathbf{x}') = \begin{pmatrix} G^{+,+}(\mathbf{x}, \mathbf{x}') & G^{+,-}(\mathbf{x}, \mathbf{x}') \\ G^{-,+}(\mathbf{x}, \mathbf{x}') & G^{-,-}(\mathbf{x}, \mathbf{x}') \end{pmatrix}, \quad (3.19)$$

where the superscripts refer to the propagation direction at \mathbf{x} and \mathbf{x}' respectively. Now choose for the source term in the one-way wave equation (3.12) a one-way point source $\mathbf{S} = \mathbf{S}_0(\mathbf{x})\delta(\mathbf{x} - \mathbf{x}_S)$, and rewrite equation (3.12) as

$$\frac{\partial \mathbf{P}}{\partial z} - \hat{\mathbf{B}}\mathbf{P} = \underbrace{\mathbf{S}_0\delta(\mathbf{x} - \mathbf{x}_S) + \{\hat{\mathbf{B}} - \underline{\hat{\mathbf{B}}}\}\mathbf{P}}_{\mathbf{S}_{tot}(\mathbf{x})}, \quad (3.20)$$

where $\mathbf{S}_{tot}(\mathbf{x})$ is interpreted as a distribution of sources. Thus, \mathbf{P} and $\underline{\mathbf{G}}$ satisfy the same wave equation, only with different source terms. By using the superposition principle, a representation of the one-way wave vector \mathbf{P} can be found according to

$$\mathbf{P}(\mathbf{x}) = \int \underline{\mathbf{G}}(\mathbf{x}, \mathbf{x}') \mathbf{S}_{tot}(\mathbf{x}') d^3 \mathbf{x}', \quad (3.21)$$

or

$$\mathbf{P}(\mathbf{x}) = \mathbf{P}^i(\mathbf{x}) + \mathbf{P}^s(\mathbf{x}), \quad (3.22)$$

where the 'incident wave field' is given by

$$\mathbf{P}^i(\mathbf{x}) = \underline{\mathbf{G}}(\mathbf{x}, \mathbf{x}_S) \mathbf{S}_0(\mathbf{x}_S) \quad (3.23)$$

and the 'scattered wave field' by

$$\mathbf{P}^s(\mathbf{x}) = \int \underline{\mathbf{G}}(\mathbf{x}, \mathbf{x}') \hat{\underline{\Delta}}(\mathbf{x}') \mathbf{P}(\mathbf{x}') d^3 \mathbf{x}', \quad (3.24)$$

with contrast operator $\hat{\underline{\Delta}}(\mathbf{x}')$ defined as (Wapenaar (1995b))

$$\hat{\underline{\Delta}}(\mathbf{x}') = \hat{\mathbf{B}}(\mathbf{x}') - \underline{\hat{\mathbf{B}}}(\mathbf{x}'). \quad (3.25)$$

Equation (3.24), with the general contrast operator defined in equation (3.25), is a generalization of the representation discussed by a.o. Coronas (1975). Equation (3.24) expresses an implicit solution for the total wavefield \mathbf{P} , because \mathbf{P} is present in both the left- and right-hand side of the equation. If multiple scattering is neglected, the incident wavefield \mathbf{P}^i may be substituted for the total wavefield \mathbf{P} in (3.24). This yields the linearized one-way representation

$$\mathbf{P}(\mathbf{x}) = \underbrace{\underline{\mathbf{G}}(\mathbf{x}, \mathbf{x}_S) \mathbf{S}_0(\mathbf{x}_S)}_{\text{'incident waves'}} + \underbrace{\int \underline{\mathbf{G}}(\mathbf{x}, \mathbf{x}') \hat{\underline{\Delta}}(\mathbf{x}') \underline{\mathbf{G}}(\mathbf{x}', \mathbf{x}_S) \mathbf{S}_0(\mathbf{x}_S) d^3 \mathbf{x}'}_{\text{'scattered waves'}}. \quad (3.26)$$

So far, a particular choice for the reference operator $\hat{\mathbf{B}}$ has not been made yet. It is defined in a similar fashion as operator $\hat{\mathbf{B}}$ in equation (3.13) as

$$\hat{\mathbf{B}} = -j\omega\hat{\mathbf{A}} + \hat{\mathbf{E}}. \quad (3.27)$$

Thus it is possible to make an independent choice for $-j\omega\hat{\mathbf{A}}$, which mainly describes the propagation effects, and $\hat{\mathbf{E}}$, which mainly describes the scattering effects. According to the conceptual model used for seismic migration, in order to extract the scattering (or reflectivity) information, the propagation effects must be removed first. Hence, in the forward model the propagation effects must explicitly be present, separated from the scattering effects. With this in mind, the following choices for the reference operators $\hat{\mathbf{A}}$ and $\hat{\mathbf{E}}$ are made:

$$\hat{\mathbf{A}} = \hat{\mathbf{A}} \quad (\text{propagation in the actual medium}) \quad (3.28.a)$$

$$\hat{\mathbf{E}} = \mathbf{O} \quad (\text{no scattering}), \quad (3.28.b)$$

where \mathbf{O} is the null matrix. This implies that the reference operator $\hat{\mathbf{B}} = -j\omega\hat{\mathbf{A}}$ now accounts for the *primary* propagation effects in the actual medium. The contrast operator $\hat{\mathbf{A}} = \hat{\mathbf{B}} - \hat{\mathbf{B}}$ accounts for the scattering effects of the actual medium, because

$$\hat{\mathbf{A}}(\mathbf{x}') = \hat{\mathbf{B}}(\mathbf{x}') - \hat{\mathbf{B}}(\mathbf{x}') = \hat{\mathbf{E}}(\mathbf{x}') = \begin{pmatrix} \hat{T}^+(\mathbf{x}') & \hat{R}^-(\mathbf{x}') \\ -\hat{R}^+(\mathbf{x}') & -\hat{T}^-(\mathbf{x}') \end{pmatrix}. \quad (3.29)$$

By substituting the *diagonal* operator matrix $\hat{\mathbf{B}}$ into the expression for the Green's function (3.18) and choosing the appropriate boundary conditions (i.e., outgoing waves for $z \rightarrow -\infty$ and for $z \rightarrow \infty$), it follows that the Green's matrix $\mathbf{G}(\mathbf{x}, \mathbf{x}')$ has a diagonal form as well:

$$\mathbf{G}(\mathbf{x}, \mathbf{x}') = \begin{pmatrix} G^{+,+}(\mathbf{x}, \mathbf{x}') & 0 \\ 0 & G^{-,-}(\mathbf{x}, \mathbf{x}') \end{pmatrix}. \quad (3.30)$$

The linearized forward model is now explicitly written as

$$\begin{aligned} P^\pm(\mathbf{x}) &= G^{\pm,\pm}(\mathbf{x}, \mathbf{x}_S) S_0^\pm(\mathbf{x}_S) \\ &\pm \int_V G^{\pm,\pm}(\mathbf{x}, \mathbf{x}') \hat{R}^\mp(\mathbf{x}') G^{\mp,\mp}(\mathbf{x}', \mathbf{x}_S) S_0^\mp(\mathbf{x}_S) d^3\mathbf{x}' \\ &\pm \int_V G^{\pm,\pm}(\mathbf{x}, \mathbf{x}') \hat{T}^\pm(\mathbf{x}') G^{\pm,\pm}(\mathbf{x}', \mathbf{x}_S) S_0^\pm(\mathbf{x}_S) d^3\mathbf{x}'. \end{aligned} \quad (3.31)$$

Introducing the propagators for the primary downgoing and upgoing waves in the actual medium $W^+(\mathbf{x}, \mathbf{x}')$ and $W^-(\mathbf{x}, \mathbf{x}')$, the non zero entries in the Green's matrix can be written as

$$G^{+,+}(\mathbf{x}, \mathbf{x}') = +H(z - z') W^+(\mathbf{x}, \mathbf{x}') \quad (3.32)$$

$$G^{-,-}(\mathbf{x}, \mathbf{x}') = -H(-z + z') W^-(\mathbf{x}, \mathbf{x}'), \quad (3.33)$$

where H is the Heaviside function. As an example, for a homogeneous medium in a 3D situation the propagators read

$$W^+(\mathbf{x}, \mathbf{x}') = W^-(\mathbf{x}', \mathbf{x}) = \frac{1}{2\pi} \frac{\partial}{\partial z'} \left(\frac{e^{-j\bar{k}\Delta\mathbf{x}}}{\Delta\mathbf{x}} \right) = \frac{1}{2\pi} \frac{1 + j\bar{k}\Delta\mathbf{x}}{\Delta\mathbf{x}} \frac{\Delta z}{\Delta\mathbf{x}} \frac{e^{-j\bar{k}\Delta\mathbf{x}}}{\Delta\mathbf{x}} \quad (3.34)$$

with $\Delta\mathbf{x} = |\mathbf{x} - \mathbf{x}'|$, $\Delta z = |z - z'|$, and $\bar{k} = \omega/\bar{c}$, with $\bar{c} = \sqrt{\bar{K}/\bar{\rho}}$, where \bar{c} is the reference propagation velocity.

Substituting (3.33) in (3.31), six separate contributions can be identified. Two contributions are the upgoing and downgoing incident wavefields

$$P_i^+(\mathbf{x}) = +H(z - z_S)W^+(\mathbf{x}, \mathbf{x}_S)S_0^+(\mathbf{x}_S) \quad (3.35)$$

$$P_i^-(\mathbf{x}) = -H(-z + z_S)W^-(\mathbf{x}, \mathbf{x}_S)S_0^-(\mathbf{x}_S), \quad (3.36)$$

and furthermore both the downgoing primary scattered wavefield

$$\begin{aligned} P_s^-(\mathbf{x}) = & - \int_V H(z - z')H(-z' + z_S)W^+(\mathbf{x}, \mathbf{x}')\hat{R}^-(\mathbf{x}')W^-(\mathbf{x}', \mathbf{x}_S)S_0^-(\mathbf{x}_S)d^3\mathbf{x}' \\ & + \int_V H(z - z')H(z' - z_S)W^+(\mathbf{x}, \mathbf{x}')\hat{T}^+(\mathbf{x}')W^+(\mathbf{x}', \mathbf{x}_S)S_0^+(\mathbf{x}_S)d^3\mathbf{x}' \end{aligned} \quad (3.37)$$

and the upgoing primary scattered wavefield

$$\begin{aligned} P_s^-(\mathbf{x}) = & + \int_V H(-z + z')H(z' - z_S)W^-(\mathbf{x}, \mathbf{x}')\hat{R}^+(\mathbf{x}')W^+(\mathbf{x}', \mathbf{x}_S)S_0^+(\mathbf{x}_S)d^3\mathbf{x}' \\ & - \int_V H(-z + z')H(-z' + z_S)W^-(\mathbf{x}, \mathbf{x}')\hat{T}^-(\mathbf{x}')W^-(\mathbf{x}', \mathbf{x}_S)S_0^-(\mathbf{x}_S)d^3\mathbf{x}' \end{aligned} \quad (3.38)$$

consist of two volume integral terms each. The Heaviside functions select pieces of the volume integral given the acquisition geometry, with receivers at depth z and sources at depth z_S . Of primary interest in seismic migration are the reflectivity operators \hat{R}^\pm .

For the representation of surface seismic data, choose both sources and receivers to lie in an upper halfspace which is homogeneous for $z \leq z_0$. Furthermore, let the source depth be larger than the receiver depth, and consider a downward radiating one-way source wavefield $S_0^+(\mathbf{x}_S)$ only ($S_0^-(\mathbf{x}_S) = 0$). In that case only the upgoing scattered wavefield is non zero and the forward model for acoustic wave equation based depth migration of surface data is obtained as

$$P_s^-(\mathbf{x}) = \int_{z' > z_0} W^-(\mathbf{x}, \mathbf{x}')\hat{R}^+(\mathbf{x}')W^+(\mathbf{x}', \mathbf{x}_S)S_0^+(\mathbf{x}_S)d^3\mathbf{x}'. \quad (3.39)$$

Berkhout (1982) introduced this one-way representation using a discrete formulation. Since then, it has commonly been known as the "WRW" model. In this thesis the WRW model is extended to include crosswell data.

Depending on the acquisition geometry and the inhomogeneities in the subsurface, for crosswell data all the contributions (3.35)-(3.38) may be non-zero. As the final goal in migration is to extract the reflectivity information contained in the \hat{R}^\pm operators, the forward model is further refined. First, the primary wavefield is removed in a pre-processing step (see Appendix A). This leaves the scattered wavefield contributions (3.37)-(3.38), containing both transmission operators \hat{T}^\pm and reflection operators \hat{R}^\pm . In the next section, it will be argued that in practice the transmission operators may be neglected by looking more closely at the physical meaning of the different contributions.

3.1.4 Practical aspects of the representation

When *flux-normalized* one-way wavefields are used (Wapenaar (1995b); De Hoop (1992)) the \hat{T}^\pm operators are truly zero if in addition the principal direction is chosen perpendicular to the layering (for example a vertical principal direction with a horizontally layered subsurface). In all other cases, the \hat{T}^\pm operators result in two kinds of contributions.

The first contribution can be identified as waves that are actually transmitted through interfaces. These waves are, in general, not distinguishable from the incident wavefield because of comparable traveltimes. Note that the sum of these transmission contributions and the incident wavefield is called the *direct* wavefield. When removing the direct wavefield, these transmission contributions are also removed.

The second contribution can physically be identified as a wavefield that, after interaction with inhomogeneities in the subsurface, is "reflected" or diffracted without reverting its direction along the principal direction. An example of such a contribution is a wavefield that is upgoing at the source well, reflected at a dipping interface and is still upgoing at the receiver well. For moderate dips, these steep angle reflections in general do not contribute significantly to the final resolution. In that case it is possible to suppress this contribution by selecting only a particular range of propagation angles in the illuminating and reflecting wavefields (see also section 3.2.2). In other cases (i.e., for steep dips), a local operation can be applied in each point of the subsurface in such a way that the scattering is again described in terms of \hat{R}^+ and \hat{R}^- , which now must be interpreted as reflections from the *top* and *bottom* of interfaces, respectively. This is described in section 3.2.3.

Summarized, when taking a vertical principal direction and a proper data selection procedure, the \hat{T}^\pm may be neglected for (near) horizontal layered media. For more general inhomogeneous media, it is possible to locally transfer the scattering contained in the \hat{T}^\pm operators to the \hat{R}^\pm operators, and therefore the \hat{T}^\pm operators may again be neglected.

Putting the terms containing \hat{T}^\pm in (3.37)-(3.38) to zero we end up with two scattered wavefields

per shot record according to

$$P_s^-(\mathbf{x}) = + \int dx' \int dy' \int_{z' > \max(z, z_s)} W^-(\mathbf{x}, \mathbf{x}') \hat{R}^+(\mathbf{x}') W^+(\mathbf{x}', \mathbf{x}_S) S_0^+(\mathbf{x}_S) dz' \quad (3.40)$$

$$P_s^+(\mathbf{x}) = - \int dx' \int dy' \int_{z' < \min(z, z_s)} W^+(\mathbf{x}, \mathbf{x}') \hat{R}^-(\mathbf{x}') W^-(\mathbf{x}', \mathbf{x}_S) S_0^-(\mathbf{x}_S) dz' \quad (3.41)$$

where the integrals are written out explicitly and the Heaviside functions are replaced by taking a limited integration interval. The two equations (3.40) and (3.41) form the forward model representation for crosswell data. In addition to a \hat{R}^+ reflectivity operator, which in general accounts for the reflectivity from the top of layers, the \hat{R}^- operator accounts for the reflectivity from the bottom of layers. Operator \hat{R}^+ is exactly the same as the one for the surface reflection situation. It is important to realize that the reflectivity operators \hat{R}^\pm describe *implicit* properties of the medium, and are independent of the seismic acquisition geometry that is used.

3.1.5 Matrix notation

The forward model obtained in section 3.1.4 can also be derived using the matrix notation introduced by Berkhout (1982). Since in practice all source/receiver coordinates and recorded data are discrete, a formulation of the forward problem in terms of matrices and vectors is especially appropriate. In discrete form the "WRW" model of equation (3.39) can be written as

$$\mathbf{P}_s^-(z_0) = \sum_m \mathbf{W}_v^-(z_0, z_m) \mathbf{R}^+(z_m) \mathbf{W}_v^+(z_m, z_0) \mathbf{S}_0^+(z_0), \quad (3.42)$$

where the integrations along the x and y axis are replaced by matrix multiplications, and the integration along the z -axis is replaced by a summation. The subscript "v" explicitly indicates that the propagators extrapolate wavefields along the vertical direction, from one depth level to another. Note that the matrix multiplication with the discrete form of the reflectivity operator \hat{R}^+ involves a *convolution* along the x -axis.

Equation 3.42 applies to the single shot case. For a one-way point source the source vector $\mathbf{S}_0^+(z_0)$ only contains one non-zero element. Furthermore, the scattered wavefield at the surface is described by the vector $\mathbf{P}_s^-(z_0)$, containing the sampled scattered wavefield at level $z = z_0$. Expression 3.42 is extended to the multi-shot situation in a straightforward way by writing

$$\mathbf{P}_s^-(z_0) = \sum_m \mathbf{W}_v^-(z_0, z_m) \mathbf{R}^+(z_m) \mathbf{W}_v^+(z_m, z_0) \mathbf{S}_0^+(z_0), \quad (3.43)$$

where the columns in matrix $\mathbf{S}_0^+(z_0)$ contain the source wavefields at $z = z_0$, and the columns in matrix $\mathbf{P}_s^-(z_0)$ contain the corresponding scattered wavefields at $z = z_0$.

For the crosswell situation a matrix expression can be obtained by discretizing equations (3.40) and (3.41). Let the z -axis again be the vertical (depth) axis, and let the source and receiver boreholes be vertical. For convenience, a 2D situation is assumed, and therefore the integrations over

y' are omitted. Since the data is acquired along vertical boreholes, we choose to replace the integration along the z -axis by a matrix multiplication. The integration along the x -axis is replaced by a summation over x with sampling Δx . There is, however, an important difference from the model for surface data, because in (3.40) and (3.41) the reflectivity operators \hat{R}^+ and \hat{R}^- implicitly describe convolutions along the x -axis. This implies that in the matrix representation an extra summation along the x -axis is needed. But if only the structural information is aimed at, a locally reacting medium may be assumed, yielding zero-offset reflectivity only. In that case the operators \hat{R}^+ and \hat{R}^- in equations (3.40) and (3.41) reduce to simple scalars R^+ and R^- . This implies that in the matrix notation a single summation along the x -axis suffices.

The total wavefield is now written in matrix-vector notation as $\mathbf{P}^\pm(x_M) = \mathbf{P}_i^\pm(x_M) + \mathbf{P}_s^\pm(x_M)$ with the incident waves given by

$$\mathbf{P}_i^+(x_M) = \mathbf{W}_h^+(x_M, x_0) \mathbf{S}_0^+(x_0) \quad (3.44)$$

$$\mathbf{P}_i^-(x_M) = \mathbf{W}_h^-(x_M, x_0) \mathbf{S}_0^-(x_0), \quad (3.45)$$

and the equations for the scattered wavefield are derived from (3.40) and (3.41) according to

$$\mathbf{P}_s^-(x_M) = + \sum_m \mathbf{W}_h^-(x_M, x_m) \mathbf{R}^+(x_m) \mathbf{W}_h^+(x_m, x_0) \mathbf{S}_0^+(x_0) \quad (3.46)$$

$$\mathbf{P}_s^+(x_M) = - \sum_m \mathbf{W}_h^+(x_M, x_m) \mathbf{R}^-(x_m) \mathbf{W}_h^-(x_m, x_0) \mathbf{S}_0^-(x_0), \quad (3.47)$$

where $\mathbf{W}_h^-(x_M, x_m)$ is a discretized version of $\{H(-z_M + z_m)W^-(\mathbf{x}_M, \mathbf{x}_m)\}$ with $\mathbf{x}_m = (x_m, z_i)$, $\mathbf{x}_M = (x_M, z_j)$ with i, j running over all depth levels, and the other propagation matrices \mathbf{W}_h^\pm are defined in a similar manner. Note that the extrapolation is performed along the horizontal direction (indicated by the subscript "h"), but that the superscripts '+' and '-' still refer to the positive and negative z -axis, i.e. downgoing and upgoing waves respectively. The propagation matrices are upper triangular or lower triangular matrices, and the reflectivity matrices are diagonal matrices. The structure of the equations is sketched in Figure 3.2.

3.2 The inverse problem: practical implementation of crosswell migration

A migration scheme can now be obtained by inverting matrix equations (3.46)-(3.47) to extract the reflectivity matrices \mathbf{R}^\pm . This means that the propagation effects that are described by the \mathbf{W}_h^\pm matrices have to be removed, and subsequently the reflectivity is imaged. Because of the similarity between equations (3.46) and (3.47) on the one hand and the equation for the forward model for surface data (3.42) on the other hand, first the scheme for the migration of surface data is revisited. Then, two approaches to crosswell migration are presented. The first approach resembles the surface seismic approach the most, and is therefore denoted as "conventional". It is, however, not valid for media containing strongly dipping layers. Therefore, in section 3.2.3 the conventional approach is extended to be valid for more general inhomogeneous media.

$$\begin{array}{c}
 \begin{array}{c}
 \downarrow z \\
 \left(\begin{array}{c} | \\ | \end{array} \right) = \left(\begin{array}{c} \xrightarrow{z'} \\ \hline \text{O} \end{array} \right) \left(\begin{array}{c} \searrow z' \\ \hline \end{array} \right) \left(\begin{array}{c} \xrightarrow{z_s} \\ \hline \text{O} \end{array} \right) \left(\begin{array}{c} \downarrow z_s \\ \bullet \end{array} \right) \\
 \mathbf{P}_s^-(x_M) \quad \mathbf{W}_h^-(x_M, x_m) \quad \mathbf{R}^+(x_m) \quad \mathbf{W}_h^+(x_m, x_0) \quad \mathbf{S}_0^+(x_0)
 \end{array} \\
 \\
 \begin{array}{c}
 \downarrow z \\
 \left(\begin{array}{c} | \\ | \end{array} \right) = \left(\begin{array}{c} \xrightarrow{z'} \\ \hline \text{O} \end{array} \right) \left(\begin{array}{c} \searrow z' \\ \hline \end{array} \right) \left(\begin{array}{c} \xrightarrow{z_s} \\ \hline \text{O} \end{array} \right) \left(\begin{array}{c} \downarrow z_s \\ \bullet \end{array} \right) \\
 \mathbf{P}_s^+(x_M) \quad \mathbf{W}_h^+(x_M, x_m) \quad \mathbf{R}^-(x_m) \quad \mathbf{W}_h^-(x_m, x_0) \quad \mathbf{S}_0^-(x_0)
 \end{array}
 \end{array}$$

Fig. 3.2 Structure of matrix equations (3.46) (top) and (3.47) (bottom).

3.2.1 Migration of surface data revisited

Assume a medium which only contains non-zero values of the reflectivity at one depth level $z = z_m$. After removal of the propagation effects, the full pre-stack equation 3.43 is written as

$$\mathbf{P}_s^-(z_m) = \mathbf{R}^+(z_m) \mathbf{P}_i^+(z_m), \quad (3.48)$$

with the forward extrapolated incident wavefields at $z = z_m$ given by

$$\mathbf{P}_i^+(z_m) = \mathbf{W}_v^+(z_m, z_0) \mathbf{S}_0^+(z_0), \quad (3.49)$$

and the inverse extrapolated scattered wavefields at $z = z_m$ given by

$$\mathbf{P}_s^-(z_m) = \mathbf{F}_v^-(z_m, z_0) \mathbf{P}_s^-(z_0), \quad (3.50)$$

where

$$\mathbf{F}_v^-(z_m, z_0) = [\mathbf{W}_v^-(z_0, z_m)]^{-1}. \quad (3.51)$$

Thus, for this situation a direct relationship exists between the incident wavefields and the scattered wavefields at level $z = z_m$, which is given by the reflectivity matrix $\mathbf{R}^+(z_m)$. Therefore, the full angle dependent reflectivity information at depth level $z = z_m$ can be obtained according to

$$\mathbf{R}^+(z_m) = \mathbf{P}_s^-(z_m) [\mathbf{P}_i^+(z_m)]^{-1}. \quad (3.52)$$

Note again that the matrix equations are monochromatic. For the special case of reflectivity at $z = z_m$ only, one monochromatic pre-stack experiment may resolve the full angle dependent information.

For a general inhomogeneous medium, equation 3.52 is rewritten as

$$\mathbf{X}^+(z_m) = \mathbf{P}_s^-(z_m)[\mathbf{P}_i^+(z_m)]^{-1}, \quad (3.53)$$

where matrix $\mathbf{X}^+(z_m)$ contains the reflectivity information of level $z = z_m$, but in addition it also contains the distorted reflectivity information of other depth levels. At each depth level $z = z_m$, it is possible to extract the full angle dependent reflectivity information from $\mathbf{X}^+(z_m)$ by using a linear Radon transform (De Bruin (1992)). But, if only the structural information is aimed at, it is sufficient to estimate the *diagonal* of the reflectivity matrix. This yields a so-called “wide-angle zero-offset reflectivity”, which is an average reflection coefficient over all angles. An estimate of this zero offset reflectivity is obtained according to

$$R_{ZO}^+(x_k, z_m) = \frac{1}{N} \sum_{\omega} X^+(x_k, x_k, z_m), \quad (3.54)$$

where $X^+(x_k, x_k, z_m)$ is the main diagonal of matrix $\mathbf{X}^+(z_m)$, $R_{ZO}^+(x_k, z_m)$ (with variable k and fixed m) is the estimate of the diagonal of the reflectivity matrix $\mathbf{R}^+(z_m)$, N denotes the number of frequency components, the annotation “ZO” denotes “zero offset”, and the index k runs over all elements of the main diagonal of $\mathbf{X}^+(z_m)$. This step is generally referred to as the actual *imaging* step. The summation over all frequencies has the effect that only zero-time contributions, which are due to the reflectivity at $z = z_m$, are selected. All other contributions are suppressed because they interfere destructively.

In equation (3.53) the data of all shot records is needed at the same time. Another approach to seismic migration is to migrate single common-shot gathers (CSG’s), and combine the results after migration. For the single shot record migration approach, in equation (3.48) only one column of \mathbf{P}_s and \mathbf{P}_i is considered. To obtain an estimate of the zero offset reflectivity for one CSG, equation (3.53) is written in scalar form as

$$X^+(x_k, x_k, z_m) = P_s^-(x_k, z_m)[P_i^+(x_k, z_m)]^{-1}. \quad (3.55)$$

This means that the inverse extrapolated scattered wavefield is deconvolved in time with the forward extrapolated incident wavefield on a trace-by-trace basis. An estimate of the zero offset reflectivity is obtained by again using equation (3.54).

Note that for the shot record approach, the incident wavefield is illuminating a subsurface point with a limited number of angles. For example, when using a point source or plane wave illumination, the wavefield may illuminate each point with only one illumination angle. In that case, one angle dependent reflection coefficient is obtained per subsurface point. For the same subsurface point, different CSG’s may yield different reflection coefficients, because of a different

illumination. By *stacking* all results, and dividing the stack by the number of shot records, again an average zero-offset reflectivity image is obtained.

With respect to the implementation of this scheme, the propagation matrices and their (spatially band limited) inverse counterparts can be built up in a recursive way by using locally optimized short convolution operators in the space-frequency domain. Combined with table driven extrapolation techniques, this approach can be both accurate and computationally efficient (Blacquière (1989), Rietveld (1995)).

3.2.2 Conventional crosswell migration approach

For the crosswell case, it has been explained that the propagation matrices are upper or lower triangular matrices, due to the fact that the principal direction of wave propagation is chosen parallel to the vertical boreholes. This is different from the surface seismic model, where the acquisition geometry is horizontal and the principal direction of wave propagation is chosen perpendicular to the acquisition aperture. Because of their structure, the crosswell propagation matrices in (3.46) and (3.47) can not be constructed in a recursive way using short convolution operators. Furthermore, the inversion of the propagation matrices is not as straightforward as in the surface seismic case. In this section, the approach taken in this thesis to overcome these extrapolation related problems is presented.

A shot record migration method is chosen for, which means that CSG's are treated independently. Equations (3.46) and (3.47) are used as a starting point. Similar to equation (3.53), at each vertical cross-section $x = x_m$, the following two relations exist:

$$\mathbf{P}_s^-(x_m) = \underline{\mathbf{X}}^+(x_m)\mathbf{P}_i^+(x_m) \quad (3.56)$$

$$\mathbf{P}_s^+(x_m) = \underline{\mathbf{X}}^-(x_m)\mathbf{P}_i^+(x_m), \quad (3.57)$$

where the incident and scattered wavefields are represented by vectors. Note that compared to equation (3.53), $\underline{\mathbf{X}}$ has a different physical meaning here. In principle, the wavefields at $x = x_m$ are computed using

$$\mathbf{P}_i^\pm(x_m) = \underline{\mathbf{W}}_h^\pm(x_m, x_0)\mathbf{S}_0^\pm(x_0) \quad (3.58)$$

$$\mathbf{P}_s^\pm(x_m) = \underline{\mathbf{W}}_h^\pm(x_M, x_m)\mathbf{P}_s^\pm(x_M) \quad (3.59)$$

where the propagation matrices $\underline{\mathbf{W}}_h^\pm$ are upper or lower triangular matrices. To compute $\mathbf{P}_s^\pm(x_m)$, (3.59) must be inverted:

$$\mathbf{P}_s^\pm(x_m) = \underline{\mathbf{F}}_h^\pm(x_m, x_M)\mathbf{P}_s^\pm(x_M) \quad (3.60)$$

where

$$\underline{\mathbf{F}}_h^\pm(x_m, x_M) = [\underline{\mathbf{W}}_h^\pm(x_M, x_m)]^{-1}. \quad (3.61)$$

Because of the advantages of recursive wavefield extrapolation techniques that are used for the surface seismic case, it is desirable that the same methods can be applied to the crosswell case. To simplify the extrapolation operators, the following approach is taken.

Using (3.58) and (3.59), we can write

$$\mathbf{P}_i^+(x_m) + \mathbf{P}_i^-(x_m) = \underline{\mathbf{W}}_h^+(x_m, x_0) \mathbf{S}_0^+(x_0) + \underline{\mathbf{W}}_h^-(x_m, x_0) \mathbf{S}_0^-(x_0) \quad (3.62)$$

$$\mathbf{P}_s^+(x_M) + \mathbf{P}_s^-(x_M) = \underline{\mathbf{W}}_h^+(x_M, x_m) \mathbf{P}_s^+(x_m) + \underline{\mathbf{W}}_h^-(x_M, x_m) \mathbf{P}_s^-(x_m). \quad (3.63)$$

Now, the objective is first to forward extrapolate the source wavefield and inverse extrapolate the total scattered wavefield to x_m , using the sum of the two propagation operators. Then in x_m , the total wavefield is again separated into upgoing and downgoing waves. Using

$$\mathbf{P}_s(x_n) = \mathbf{P}_s^+(x_n) + \mathbf{P}_s^-(x_n) \quad (3.64)$$

for each $0 \leq n \leq M$ and

$$\underline{\mathbf{W}}_h(x_M, x_m) = \underline{\mathbf{W}}_h^+(x_M, x_m) + \underline{\mathbf{W}}_h^-(x_M, x_m), \quad (3.65)$$

equation (3.63) is rewritten as

$$\mathbf{P}_s(x_M) = \underline{\mathbf{W}}_h(x_M, x_m) \mathbf{P}_s(x_m). \quad (3.66)$$

This is possible because the terms $\underline{\mathbf{W}}_h^\pm(x_M, x_m) \mathbf{P}_s^\mp(x_m)$ are negligible. The forward propagation matrix $\underline{\mathbf{W}}_h$ is the sum of the two triangular propagation matrices and thus it is a *full* matrix again.

The scattered wavefield at x_m is computed by inverse wavefield extrapolation from x_M to x_m according to

$$\mathbf{P}_s(x_m) = \underline{\mathbf{F}}_h(x_m, x_M) \mathbf{P}_s(x_M), \quad (3.67)$$

with inverse operator

$$\underline{\mathbf{F}}_h(x_m, x_M) = [\underline{\mathbf{W}}_h(x_M, x_m)]^{-1}. \quad (3.68)$$

To regain the up and downgoing scattered wavefield at each x_m , we write

$$\mathbf{P}_s^\pm(x_m) = \underline{\mathbf{B}}^\pm(x_m) \mathbf{P}_s(x_m), \quad (3.69)$$

where the matrices $\underline{\mathbf{B}}^\pm$ contain convolutional separation operators, which are based on dip filtering techniques.

Similarly, equation (3.62) is written as

$$\mathbf{P}_i^\pm(x_m) = \underline{\mathbf{B}}^\pm(x_m) \underline{\mathbf{W}}_h(x_m, x_0) \mathbf{S}_0^\pm(x_0). \quad (3.70)$$

Hence, similar to the scattered wave field, the incident wave field is forward extrapolated using the sum of the two original propagator matrices and then again split into up and downgoing waves with the operators contained in the matrices \mathbf{B}^{\pm} .

To further simplify the propagator matrices \mathbf{W}_h , they are approximated by propagators similar to those used in the surface seismic case, but rotated by 90 degrees such that the original convolutions along the x -axis are now applied along the z -axis. Let such a primary propagator be denoted by the subscript 'a'. The forward and inverse propagators are written as:

$$\mathbf{W}_h(x_m, x_0) \approx \mathbf{W}_a(x_m, x_0) \quad (3.71)$$

$$\mathbf{F}_h(x_m, x_M) \approx \mathbf{F}_a(x_m, x_M). \quad (3.72)$$

These operators extrapolate the wavefield along the horizontal axis. To avoid scattering along the z -axis, the macro model must be smoothed. The advantage of this approach is that the extrapolation operators \mathbf{W}_a and \mathbf{F}_a can now be built up recursively and efficiently, using short operators in the space-frequency domain that are applied as local convolutions along the z -axis (Blacquièrè (1989), Rietveld (1995)).

With respect to the inverse propagator, so far it has been assumed that it is possible to simply invert the corresponding forward propagator. In practice, instability problems may arise. Therefore, in this thesis the inverse propagator is computed by complex conjugating the forward operator:

$$\mathbf{F}_a(x_m, x_M) = [\mathbf{W}_a(x_M, x_m)]^{-1} \approx [\mathbf{W}_a(x_m, x_M)]^*, \quad (3.73)$$

which is commonly known as the "matched filter approach". In this way, propagating waves are treated correctly, while evanescent waves are suppressed.

Summarized, the incident wavefield and scattered wavefield at each x_m are obtained by using the equations

$$\mathbf{P}_i^{\pm}(x_m) = \mathbf{B}^{\pm}(x_m) \mathbf{W}_a(x_m, x_0) \mathbf{S}_0^{\pm}(x_0) \quad (3.74)$$

and

$$\mathbf{P}_s^{\pm}(x_m) = \mathbf{B}^{\pm}(x_m) [\mathbf{W}_a(x_M, x_m)]^* \mathbf{P}_s(x_M). \quad (3.75)$$

The crosswell imaging step differs from the surface seismic procedure, because for the crosswell situation we have to distinguish between \mathbf{R}^+ and \mathbf{R}^- , and the imaging must be carried out twice. In essence, the procedure is the same as the one used for surface data and involves a deconvolution (compare equation (3.55))

$$\mathbf{X}^{\pm}(x_m, z_k, z_k) = \mathbf{P}_s^{\mp}(x_m, z_k) [\mathbf{P}_i^{\pm}(x_m, z_k)]^{-1}, \quad (3.76)$$

and then the actual imaging takes place (compare equation (3.54))

$$R_{ZO}^{\pm}(x_m, z_k) = \frac{1}{N} \sum_{\omega} X^{\pm}(x_m, z_k, z_k). \quad (3.77)$$

Equation (3.76) means that in every point $(x, z) = (x_m, z_k)$ the received wavefield is deconvolved with the illuminating wavefield and then in equation (3.77) the result is averaged over all frequencies to select zero time. This is done twice to estimate both R_{ZO}^+ and R_{ZO}^- . Note that because of the way in which the reflectivity operators are defined (equation 3.16 on page 51), the zero offset reflectivity estimates $R_{ZO}^+(x_m, z_k)$ and $R_{ZO}^-(x_m, z_k)$ have opposite signs.

The separation matrices \mathbf{B}^{\pm} split the wavefield in upgoing and downgoing waves, along the (vertical) principal direction. The operators in \mathbf{B}^{\pm} are constructed using the same optimization techniques as are used for the propagator operators. For a horizontally layered subsurface, the separation may be carried out by simply discriminating between waves with positive and negative propagation angles with respect to the x -axis. If there are moderately dipping layers present, the separation operators may be designed to also suppress a range of incident and reflected waves around the horizontal axis. As has been argued in section 3.1.4, in this way the contributions due to the \hat{T}^{\pm} operators, which have a low resolution anyway, may be neglected.

If the objective is to image (strongly) dipping layers, the decomposition into “upgoing” and “downgoing” waves must be performed along a direction perpendicular to the local orientation of the layers. In the next section, this alternative approach is presented.

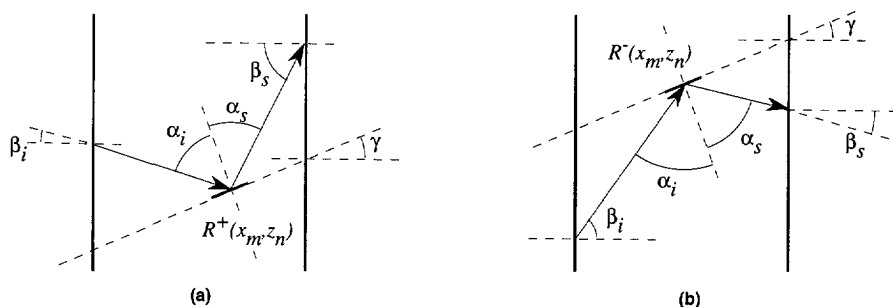


Fig. 3.3 The relation between the angle of the incident and scattered waves in a subsurface point determines which part of the reflectivity R^{\pm} is present. (a) For $R^+(x_m, z_n)$ it follows that $\beta_i < \beta_s$. (b) For $R^-(x_m, z_n)$ it follows that $\beta_i > \beta_s$.

3.2.3 Alternative approach to crosswell migration

In this section a crosswell migration method is presented which is valid for general inhomogeneous media. Instead of using a fixed direction along which the waves are separated into upgo-

ing and downgoing waves, a direction must be chosen based on the local inhomogeneities. The key issue is to consider the difference between the local angle of the incident and the reflected waves in each point of the subsurface. Consider the two situations sketched in Figure 3.3. An incident plane wave with angle β_i is reflected at a local reflector with dip angle $-\pi/2 < \gamma < \pi/2$, into a plane wave with angle β_s . When using a local plane reflector assumption, then $\alpha_i = \alpha_s$. For both situations it follows that

$$\beta_s = 2\gamma - \beta_i. \quad (3.78)$$

In the limiting case that $\beta_i = \gamma$, the waves travel along the reflector, and there is no reflected energy. If $\beta_i \neq \gamma$, two cases can be identified:

$$\beta_i < \beta_s \Leftrightarrow \beta_i < \gamma \Leftrightarrow (\beta_i - \gamma) < 0 : \text{reflection at top of interfaces } (R^+), \quad (3.79)$$

$$\beta_i > \beta_s \Leftrightarrow \beta_i > \gamma \Leftrightarrow (\beta_i - \gamma) > 0 : \text{reflection at bottom of interfaces } (R^-). \quad (3.80)$$

Essentially, the goal is to discriminate between these two cases: reflected waves in case (3.79) must only contribute to R^+ , and reflected waves in case (3.80) must only contribute to R^- .

Using equation (3.78), the local dip can be derived from the angles of the incident and scattered waves. These are actually available from the forward extrapolated incident wavefield and the inverse extrapolated scattered wavefield. This observation leads to a convenient solution to distinguish between (3.79) and (3.80), by looking at the data after trace-by-trace deconvolution of the scattered wavefield with the incident wavefield. This will now be further explained.

Let a local unit incident plane wave be defined in the time domain along depth z as

$$p_i(z, t) = \delta\left(t + \frac{z}{c} \sin \beta_i\right), \quad (3.81)$$

where c is the local propagation velocity and δ is the Dirac delta function. Similarly, a local unit scattered plane wave is defined as

$$p_s(z, t) = \delta\left(t + \frac{z}{c} \sin \beta_s\right). \quad (3.82)$$

The deconvolution procedure subtracts the traveltime of the incident wavefield from the scattered wavefield for every z -level, yielding the deconvolved result

$$p_d(z, t) = \delta\left(t + \frac{z}{c} [\sin \beta_s - \sin \beta_i]\right), \quad (3.83)$$

or, using equation (3.78)

$$p_d(z, t) = \delta\left(t + \frac{2z}{c} [\sin(\gamma - \beta_i) \cos \gamma]\right). \quad (3.84)$$

The deconvolved plane wave can be represented by

$$p_d(z, t) = \delta\left(t + \frac{z}{c} \sin \beta_d\right), \quad (3.85)$$

where $c' = c/2$ and $\sin \beta_d = \sin(\gamma - \beta_i) \cos \gamma$. Recall that we want to discriminate between situation (3.79) and (3.80). Because $\cos \gamma > 0$ for $-\pi/2 < \gamma < \pi/2$, we can now discriminate between the two situations in the *deconvolved* result, by simply discriminating between $\beta_d > 0$ and $\beta_d < 0$. Note that in the limiting case of a horizontal reflector ($\gamma = 0$) and an incident wave that is traveling along the vertical z -axis, the wavelength along the z -axis in the deconvolved result is equal to *half* the wavelength of the incident (and scattered) wave, due to the fact that $c' = c/2$. This is important with respect to the spatial sampling interval that is chosen. If the input data is not spatially aliased, it may still be necessary to decrease the spatial sampling prior to deconvolution to avoid aliasing.

Summarized, the order of the separation process (see equations (3.74) and (3.75)) and the deconvolution process (equation (3.76)) is interchanged. First a deconvolution using the total wavefields is carried out at each $x = x_m$ on a trace-by-trace basis:

$$X(x_m, z_k, z_k) = P_s(x_m, z_k)[P_i(x_m, z_k)]^{-1}, \quad (3.86)$$

and then the wavefields are separated:

$$\mathbf{X}^\pm(x_m) = \mathbf{B}^\pm(x_m)\mathbf{X}(x_m), \quad (3.87)$$

where for notational convenience the scalar values of $X(x_m, z_k, z_k)$ in equation (3.86) are put into a vector $\mathbf{X}(x_m)$. The matrices \mathbf{B}^\pm again contain local angular filters which are constructed using optimized short operators. Note that these have the same function as the filters in equations (3.74) and (3.75), but they do not have to be identical to the ones in equations (3.74) and (3.75). After the separation step, the imaging is again performed by using equation (3.77) to extract the zero-offset reflectivity information.

Note that the separation operators are *independent* of the medium parameters because the operators only have to split the wavefields around zero angle; it is only necessary to discriminate between the situations $\beta_d > 0$ and $\beta_d < 0$.

3.2.4 Implementation of the deconvolution step

In practice, the deconvolution process, as used in equations (3.55), (3.76) and (3.86) can be tedious, because the illuminating wavefield may be small or zero in badly illuminated areas like shadow zones. Therefore, the deconvolution step is reconsidered here in more detail.

It is useful to look at the following version of equation (3.86), which, with the proper “+” and “-” annotations, is also valid for equation (3.76):

$$X(x_m, z_k, z_k) = \frac{P_s(x_m, z_k)[P_i(x_m, z_k)]^*}{\{P_i(x_m, z_k)[P_i(x_m, z_k)]^*\}^q + \epsilon_q}. \quad (3.88)$$

Depending on the parameter q , three different types of imaging can be identified:

- $q = 0$: Correlation only ($\epsilon_0 \equiv 0$)
- $q = 1/2$: Partial stabilized deconvolution
- $q = 1$: True stabilized deconvolution .

For $q = 0$, the forward extrapolated illuminating wavefield is correlated with the inverse extrapolated scattered wavefield. Using correlation in seismic imaging was introduced by Claerbout (1971). The “deconvolution” is always stable and $\epsilon_0 \equiv 0$. This means that the wavelet that is present in $X(x_m, z_k, z_k)$ is a correlation between the wavelet that is present in the data and the wavelet that is present in the source wavefield. Furthermore, in regions with less illumination (where $P_i(x_m, z_k)$ is small) the reflectivity estimate obtained after imaging is additionally suppressed. This also includes the effect of geometrical spreading.

If $q = 1/2$, the actual amplitude of the illuminating wavefield is not used; only its phase is used. Effects of spherical divergence and bad illumination are just left in the data but are also not exaggerated, as is the case for $q = 0$. The spectral amplitudes of the wavelet in the data are not affected. If there are regions where the illuminating wavefield approaches zero, a stabilization factor $\epsilon_{1/2} = \epsilon$ may be required, where the value of ϵ is related to the absolute amplitude in the incident wavefield.

If $q = 1$, the true amplitude approach that is followed in this thesis is obtained. Effects of spherical divergence and poor illumination are corrected for. In regions where the illuminating wavefield approaches zero, the migration image may be too noisy and must be suppressed by using a stabilization factor $\epsilon_1 = \epsilon^2$. Note that in regions where ϵ is significantly higher than the absolute amplitude of the incident wavefield, the deconvolution approaches a correlation scaled with $1/\epsilon^2$. Thus, in poorly illuminated areas again the reflectivity estimate is suppressed.

The incident wavefield $P_i(x_m)$ contains the source signature. In practice, it may be difficult to estimate a source signature for each CSG. Therefore, it is customary to take a source signature which has unit amplitude in the frequency domain, within the band of interest. The consequence is that, for all three methods, the original wavelet that is present in the data is also present in the deconvolved result, and thus in the migrated sections. The handling of geometrical spreading is not affected. With respect to the phase of the unit-amplitude wavelet, it is necessary to approximate the phase of the real wavelet in such a way that after deconvolution the signal is close to zero phase. A zero phase deconvolved result is mandatory if we want to combine the migration results for R^+ and R^- , as only in that case reflectors are imaged at the same position. As a first approximation to zero phasing the wavelet, the time offset between the first break to the maximum peak of the direct wave may be taken into account.

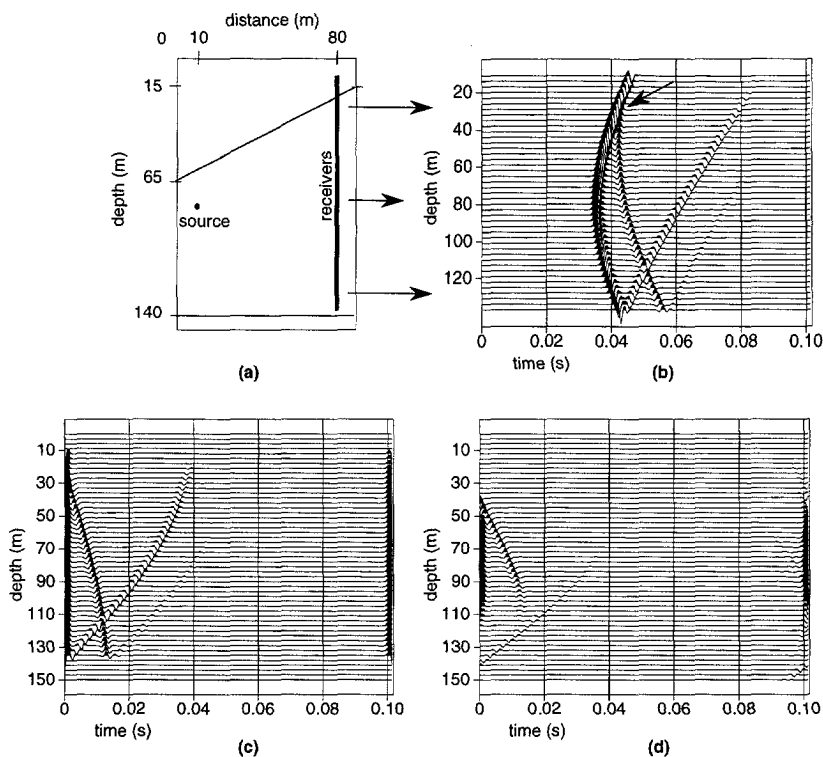


Fig. 3.4 (a) Model with two reflectors composed of density contrasts. (b) Acoustic finite difference data with a source at a depth of $z = 80$ m. (c) Same shot record deconvolved with incident wavefield. (d) Shot record inverse extrapolated to $x = 50$ m and then deconvolved with incident wavefield.

3.2.5 Steep-dip example

To illustrate the process of inverse wavefield extrapolation and deconvolution, an example is presented. Figure 3.4.a shows a simple model with two reflectors: one dipping reflector at the top and, as a reference, one horizontal reflector at the bottom, at $z = 140$ m. Only density contrasts are present, the velocity field is taken homogeneous. Figure 3.4.b shows one shot record obtained with acoustic finite difference modeling with the source at the position indicated in (a). The most interesting region is indicated by the arrow, where both the incident and reflected wavefield are traveling in the $-z$ direction. If we chose to do a decomposition into upgoing and downgoing waves along the (vertical) z -axis, this steep angle reflection would be attributed to a *transmitted* wave (see also section 3.1.4). In this example, the “alternative” approach of section

3.2.3 is taken. First, the shot record is deconvolved with the incident wavefield at the receiver well. This result is plotted in Figure 3.4.c. It shows that the direct wavefield correctly lines up at $t = 0$, since the true velocity is used¹. Moreover, the reflection responses of both reflectors now have opposite effective propagation angles and can be separated in the angular domain. Figure 3.4.d shows the result of inverse extrapolating the shot record in (b) to $x = 50$ m, and a subsequent deconvolution with the incident wavefield. Again the direct wave is aligned at $t = 0$, showing the correctness of the velocity field, and the two reflections intersect the $t = 0$ axis at the correct depth of the reflectors at a vertical cross-section $x = 50$ m.

Note that in this example the direct wave is left in the data just to give insight into the deconvolution procedure. It must be removed before the actual imaging takes place. For reasons of efficiency it is preferable to remove it from the original shot records, and not at each x_m .

3.3 Spatial resolution - surface data versus crosswell data

In this section the spatial resolution that can be obtained in the proposed crosswell migration procedure is addressed, and a comparison is made with the migration scheme for surface data. The analysis is based on spatial Fourier techniques which are also employed in the field of geophysical diffraction tomography (Devaney (1984), Wu and Toksoz (1987)). For an extensive discussion on resolution in (surface) seismic migration see Berkhout (1984b).

The forward model of equation (3.40) on page 56, which contains the \hat{R}^+ operator, is used as a starting point. Assume a 2D situation. Choose a unit (one-way) point source at (x_S, z_S) and a detector point at (x_D, z_D) . Let the reflectivity be given by the scalar $R^+(x, z)$ (zero offset reflectivity only). Consider the relation between the downgoing source wavefield and the upgoing wavefield at the detectors by rewriting equation (3.40) as:

$$P_S^-(x_D, z_D | x_S, z_S) = \int_{z > \max(z_D, z_S)} \int_{-\infty}^{+\infty} W^-(x_D, z_D, |x, z) R^+(x, z) W^+(x, z, |x_S, z_S) dx dz. \quad (3.89)$$

For a homogeneous macro model the propagators are shift invariant and can both be represented by the same function W

$$W^+(x, z, |x_S, z_S) = W^+(x - x_S, z - z_S | 0, 0) = W(x - x_S, z - z_S) \quad (3.90)$$

$$W^-(x_D, z_D, |x, z) = W^-(x_D - x, z_D - z | 0, 0) = W(x_D - x, z_D - z), \quad (3.91)$$

and thus

$$P_S^-(x_D, z_D | x_S, z_S) = \int_{z > \max(z_D, z_S)} \int_{-\infty}^{+\infty} W(x_D - x, z_D - z) R^+(x, z) W(x - x_S, z - z_S) dx dz. \quad (3.92)$$

¹Note that errors in the alignment of the direct wave at $t = 0$ are related to errors in the macro velocity model and may thus be used to update this model.

Define the spatial Fourier transform of W according to

$$\tilde{W}(k_x, z) = \int_{-\infty}^{+\infty} W(x, z) e^{+jk_x x} dx. \quad (3.93)$$

Equation (3.92) is transformed over x_D and x_S to the spatial Fourier domain, yielding

$$\begin{aligned} \tilde{\tilde{P}}_s^-(k_{x_D}, z_D | k_{x_S}, z_S) = \\ \int_{z > \max(z_D, z_S)} \int_{-\infty}^{+\infty} \tilde{W}(k_{x_D}, z_D - z) e^{jk_{x_D} x} R^+(x, z) \tilde{W}(k_{x_S}, z - z_S) e^{jk_{x_S} x} dx dz. \end{aligned} \quad (3.94)$$

It is well known that in the spatial Fourier domain W is the phase shift operator

$$\tilde{W}(k_x, z) = e^{-j\sqrt{k^2 - k_x^2}|z|}. \quad (3.95)$$

Here only the propagating part of the wavefield is considered. Substituting (3.95) in (3.94) yields

$$\tilde{\tilde{P}}_s^-(k_{x_D}, z_D | k_{x_S}, z_S) = \int_{z > \max(z_D, z_S)} \int_{-\infty}^{+\infty} e^{-jk_{z_D}|z_D - z|} e^{jk_{x_D} x} R^+(x, z) e^{-jk_{z_S}|z - z_S|} e^{jk_{x_S} x} dx dz, \quad (3.96)$$

where

$$k_{z_D} = \sqrt{k^2 - k_{x_D}^2} \quad \text{and} \quad k_{z_S} = \sqrt{k^2 - k_{x_S}^2}. \quad (3.97)$$

To obtain the surface seismic case, $z_D = z_S = 0$ is chosen. Furthermore, assume that the medium is homogeneous for $z < 0$. After some rearranging, (3.96) reads

$$\tilde{\tilde{P}}_s^-(k_{x_D}, 0 | k_{x_S}, 0) = \iint_{-\infty}^{+\infty} R^+(x, z) e^{+j(k_{x_S} + k_{x_D})x} e^{-j(k_{z_D} + k_{z_S})z} dx dz. \quad (3.98)$$

Thus, by defining the spatial Fourier coordinates

$$K_x = k_{x_S} + k_{x_D} \quad (3.99)$$

$$K_z = -(k_{z_D} + k_{z_S}) \quad (3.100)$$

the scattered wavefield at the surface is directly related to the 2D spatial Fourier transform of $R^+(x, z)$:

$$\tilde{\tilde{P}}_s^-(k_{x_D}, 0 | k_{x_S}, 0) = \check{R}^+(K_x, K_z), \quad (3.101)$$

where the double spatial Fourier transform of $R^+(x, z)$ is defined as

$$\check{R}^+(K_x, K_z) = \iint_{-\infty}^{+\infty} R^+(x, z) e^{+jK_x x} e^{+jK_z z} dx dz. \quad (3.102)$$

An estimate of the zero offset reflectivity can thus be obtained by inverting equation (3.101). Before discussing the results any further, the crosswell situation is addressed.

For the crosswell migration scheme, the same phase shift operators are used as for the surface seismic scheme, but they are applied as convolutions along the z -axis instead of along the x -axis (see section 3.2.2). To simplify the analysis it is assumed that the "reflectivity" merely consists of monopole point scatterers. Note that a point scatterer is build up from all spatial wavelengths from zero to infinity, which makes it attractive to use in resolution analysis. The advantage of the simplification is that it is not necessary to explicitly distinguish between R_{ZO}^+ and R_{ZO}^- , since they have the same polarity and may simply be added. Dropping the distinction between R_{ZO}^+ and R_{ZO}^- , and introducing the crosswell propagators W_a , an equation similar to equation (3.92) is obtained according to

$$P_s(x_D, z_D | x_S, z_S) = \iint_{-\infty}^{+\infty} W_a(x_D - x, z_D - z) R(x, z) W_a(x - x_S, z - z_S) dx dz. \quad (3.103)$$

Transforming this equation over z_D and z_S to the spatial Fourier domain yields

$$\tilde{P}_s(x_D, k_{zD} | x_S, k_{zS}) = \iint_{-\infty}^{+\infty} \tilde{W}_a(x_D - x, k_{zD}) e^{jk_{zD}z} R(x, z) \tilde{W}_a(x - x_S, k_{zS}) e^{jk_{zS}z} dx dz, \quad (3.104)$$

where, for a homogeneous macro model, the phase shift operator is now defined as

$$\tilde{W}_a(x, k_z) = e^{-jk_x|x|} \quad \text{with} \quad k_x = \sqrt{k^2 - k_z^2}. \quad (3.105)$$

Substituting (3.105) in (3.104) and choosing $x_S < x < x_D$ with $x_S = 0$ yields

$$\tilde{P}_s(x_D, k_{zD} | 0, k_{zS}) = e^{-jk_{x_D}x_D} \iint_{-\infty}^{+\infty} R(x, z) e^{j(k_{x_D} - k_{x_S})x} e^{j(k_{z_S} + k_{z_D})z} dx dz. \quad (3.106)$$

For the crosswell case the spatial Fourier coordinates are defined by

$$K_x = k_{x_D} - k_{x_S} \quad (3.107)$$

$$K_z = k_{z_D} + k_{z_S} \quad (3.108)$$

and the scattered wavefield at the detector borehole is directly related to the 2D spatial Fourier transform of $R(x, z)$

$$\tilde{P}_s(x_D, k_{zD} | 0, k_{zS}) e^{+jk_{x_D}x_D} = \tilde{R}(K_x, K_z), \quad (3.109)$$

where, compared to equation (3.101), an additional phase shift $e^{+jk_{x_D}x_D}$ is present due to the distance between the source and receiver boreholes. The results will now be further discussed.

Figure 3.5 shows the way in which the illumination of the subsurface by one plane wave (one value of k_{x_S}) resolves the (single-frequency) reflectivity in the subsurface along a semi-circle

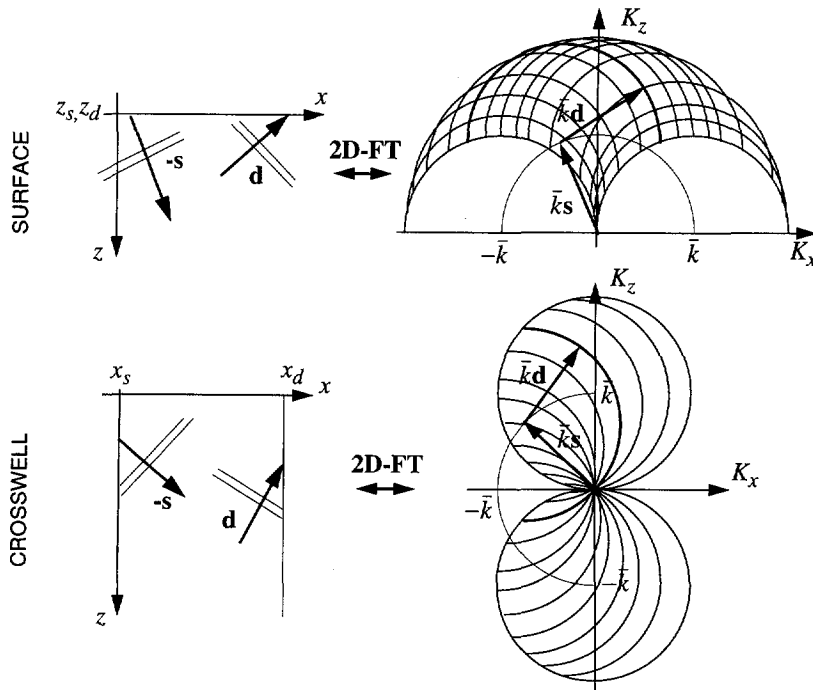


Fig. 3.5 Spectral coverage in the migration of surface data and crosswell data for a homogeneous macro velocity model. Top: surface configuration. Bottom: crosswell configuration. In the spatial domain, a plane incident wave traveling along unit vector $-s$ is scattered in the subsurface, causing a scattered plane wave traveling along the direction of unit vector d . In the double spatial Fourier domain the composition of the vectors $\bar{k}s$ and $\bar{k}d$ point to the related spectral Fourier component that is resolved when this single plane wave data is migrated. For the surface seismic case, $\bar{k}s = (k_{x_s}, -k_{z_s})^T$ and $\bar{k}d = (k_{x_d}, -k_{z_d})^T$, whereas for the crosswell case $\bar{k}s = (-k_{x_s}, k_{z_s})^T$ and $\bar{k}d = (k_{x_d}, k_{z_d})^T$. Taking all plane incident and scattered waves into account, a region in the double spatial Fourier domain spanned by the sketched semi-circles pointed at by $\bar{k}d$ is resolved.

in the spatial Fourier domain (K_x, K_z) . By varying the positions of sources and detectors, an area indicated by the envelope of all semi-circles is covered. By increasing the frequency, the radius of the semi-circles is increased, and higher spatial frequencies are resolved. In the figure the theoretical maximum angular coverage is plotted, whereas in practice the semi-circles will not span a full ± 90 degrees (with respect to the z - or K_z -axis) for the surface seismic case or a full $0 - 180$ degrees for the crosswell seismic situation. The main cause of this limitation in practice is the finite length of the source and receiver arrays. For the surface seismic case, a

typical range of angles is ± 60 degrees around the vertical axis and for crosswell this range is about ± 75 degrees around the horizontal axis. In the spatial Fourier domain these constraints limit the maximum spatial frequency along the K_x direction for the surface reflection case, and along the K_z direction for the crosswell case. For examples of limited angular coverage plots, see Devaney (1984) or Berkhout (1987).

The spectral coverage is closely related to the resolution that can be obtained. In general, by increasing the spectral coverage towards higher K_x and K_z values, the resolution in the migrated section is also increased. Comparing the surface reflection and crosswell situation, it is clear that for the same temporal frequency the surface reflection method resolves higher spatial frequencies along the horizontal axis. Thus, for the same temporal frequency band, and even for full angular coverage, the resolution along the horizontal axis is always better for surface seismic migration. The highest spatial frequency along the vertical axis is obtained for zero incident and scattered wave angles with respect to the depth axis. In general, because of the limited angular coverage, the crosswell method also has less resolution along the vertical axis for the same temporal frequency. In conclusion, to obtain crosswell reflection images with a resolution higher than that obtainable with the surface reflection method, it is mandatory to have measurements obtained at sufficiently high temporal frequencies.

To show the influence of acquisition geometry constraints on the resolution, a simple crosswell example is presented. Consider a subsurface model with one point diffractor and a homogeneous macro velocity model. The model is 100 m wide and 150 m high, with the point diffractor centered. Sources are placed along the left side of the model and receivers at the right. Figure 3.6 shows the results of performing a crosswell migration procedure on six different partial datasets. The bars indicate which parts of the source and receiver arrays are used in each case. The migrated images are the result of combining $R^+(x_m, z_n)$ and $R^-(x_m, z_n)$.

A point diffractor can be seen as a sum over a large range of infinitesimally thin layers with different dip angles, equally distributed over all angles. Figure 3.6 shows that for each part of the data that is used a different dip range is imaged, which builds up the image of the point diffractor. Especially in the cases where the point diffractor lies on the center-line that can be drawn from the center of the partial source array to the center of the partial receiver array, the resolution is relatively low. For these cases (i.e. (c) and (e)), the incident waves and scattered waves are mainly propagating along directions which do not deviate much from the center-line. As can be seen in Figure 3.5, for this situation a spectral area in the double Fourier domain is resolved with only low spatial frequencies, explaining the low resolution. Figure 3.6.a exhibits the largest resolution along both the horizontal and vertical axes, as for this configuration the largest differences in propagation angles between the incident and scattered waves are present.

From these observations, an important conclusion can be drawn. For a crosswell survey with vertical boreholes in a near horizontally layered subsurface, the ratio {borehole

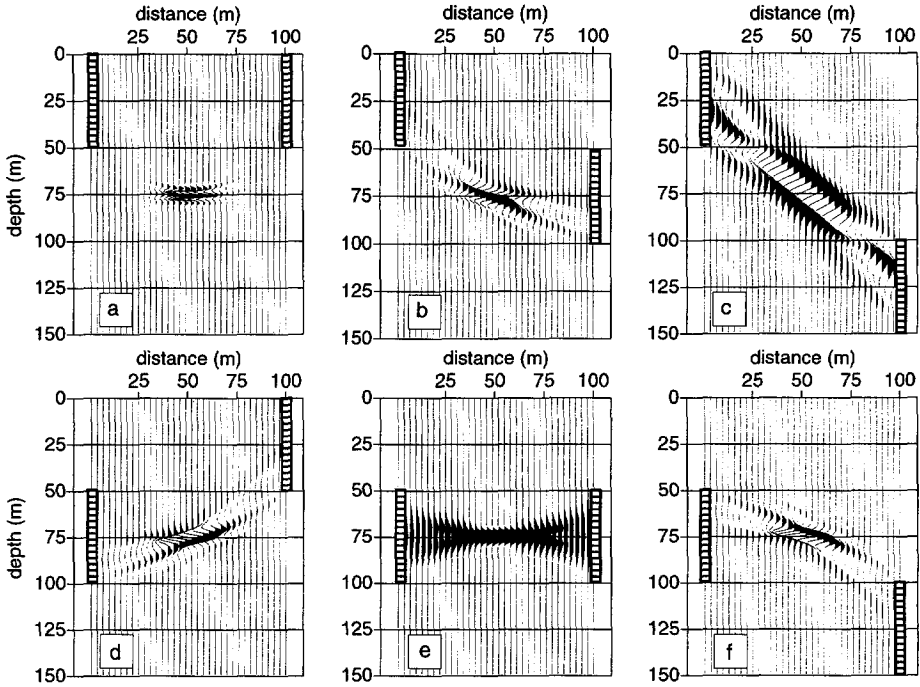


Fig. 3.6 Migrated images of scattered wavefields from a point diffractor at $(x, z) = (50, 75)$ m showing the influence of the acquisition geometry on the resolution. Sources are placed on the left side of the model, receivers on the right. Only the sources and receivers indicated by the bars are used. Note the symmetry between (b), (d) and (f).

depth}/\{borehole distance\} must be *as large as possible*, to allow for incident waves that propagate as closely as possible to the vertical direction. This will yield the highest possible resolution.

3.4 Illumination aspects

In a crosswell survey using vertical wells, it is not possible to have a normal incidence illumination of horizontal reflectors, which is a common situation for surface seismic experiments. Apart from this wide-angle illumination feature, some other important characteristics are present in crosswell migration images. These characteristics are also related to the way the subsurface is illuminated. Using a simple one-reflector example, some aspects are now further investigated.

At the left of Figure 3.7 a crosswell model is shown, which is 180 m wide and 200 m deep, and has a constant velocity of 2750 m/s. From the left side of the model, an incident plane wave with an angle α with respect to the vertical axis is put into the model by means of acoustic finite

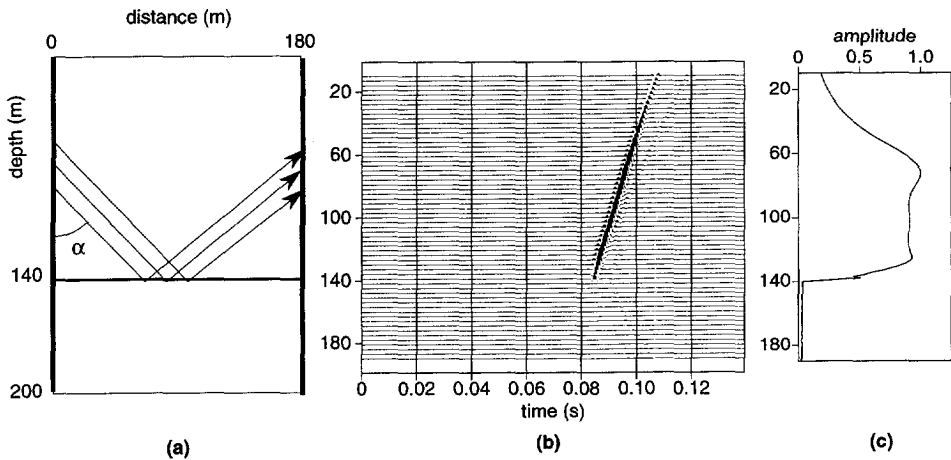


Fig. 3.7 Plane wave illumination of a horizontal reflector. (a) Model with one reflector. (b) Reflection response for $\alpha = 60$ degrees after pre-processing. (c) Amplitude cross-section over reflection response.

difference modeling. This plane wave is reflected at a horizontal reflector at 140 m depth consisting of a density contrast, and then recorded at the right side. A recording of the response for $\alpha = 60$ degrees is shown in the middle of Figure 3.7, where the direct waves have been eliminated by means of a median filtering procedure (see Appendix A). The reflected wave is now clearly visible. On the right side of Figure 3.7, an amplitude cross-section over the absolute values of this reflection event is plotted. An important observation is the fact that only a small part in the plot has an amplitude with a constant value, whereas it would be expected that for this experiment the amplitude of the reflected event would be flat everywhere. Two arguments to explain these results are now discussed.

1. The source array is finite at the top and bottom causing finite aperture effects. It is clear that the bottom end of the source array (for $z = 140$ m) has no influence on the reflected event. The top end of the array only influences the amplitude on the *right* side of the reflector, near 140 m depth in the amplitude cross-section. In that part, the direct wave removal procedure already caused the amplitude to go down a bit, so from the amplitudes it is difficult to judge whether this effect is present. From the snapshots, of which four are shown in Figure 3.8, it can be observed that for this experiment the edge-effects of the source array are not influencing the amplitude near the reflector at (180,140) m. In general, if the ratio {distance from the (top- or bottom) edge of the source array to a reflector} versus {distance between the wells} is increased, the finite aperture effect of the source array becomes less important. With respect to the migration, the deconvolution procedure described in equation (3.88) on page 65 with $q = 1$ corrects for this

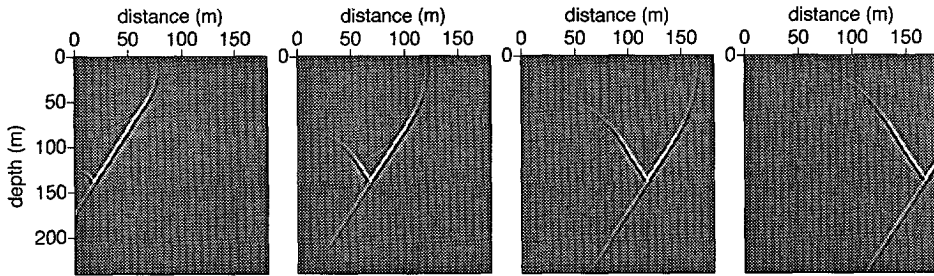


Fig. 3.8 Snapshots at four different times showing the plane wave illumination of a horizontal reflector for $\alpha = 60$ degrees.

finite source array effect.

2. The reflection of the plane wave on the interface can be translated to a situation with a homogeneous medium with a source array mirrored vertically in the reflector, thus starting from 140 m and going downwards. This means that another finite aperture effect is present, namely the "virtual" end of the source array at the position of the reflector. This effect causes the decrease of the amplitude in the cross-section of Figure 3.7 near the top of the receiver aperture. This is also clearly visible in the snapshots shown in Figure 3.8. Whereas for the surface seismic method this situation is not common, for crosswell acquisitions it can not be avoided.

Summarized, for a multi-shot crosswell survey, each reflector that crosses the source borehole may be poorly illuminated near that borehole. For the crosswell case, the illumination of (horizontal) reflectors is *not uniform* and furthermore it is *not symmetric* with respect to a vertical symmetry axis.

At this point, the influence of the illumination on the migration is investigated. In Figure 3.9 migration results using the single plane wave reflection data of Figure 3.7 are shown. Figures (a), (b) and (c) are obtained by using equations (3.76), (3.77) (on page 63) and (3.88) (on page 65) with $p=1$, for $\alpha = 70$, $\alpha = 60$ and $\alpha = 50$ degrees respectively. At the top row three images of $R_{ZO}^+(x_m, z_n)$ are shown, which are zoomed in on a depth range between 100 m and 180 m. In the migration procedure, the correct wavelet has been used. Because of the deconvolution process the images exhibit a sharp main lobe on the position of the reflector, but also the ringing effect of a sinc function can be observed. Note the way in which the vertical resolution increases with the decreasing angle of incidence, as has been explained in section 3.3.

The bottom row shows the normalized amplitude cross-sections over the migration images. With respect to the amplitudes the influence of the non-uniform illumination has become clearly visible, because in the ideal case the amplitude should be constant over the reflector. For all three angles, the amplitude is lower on the left side of the reflector due to the finite aperture effect of

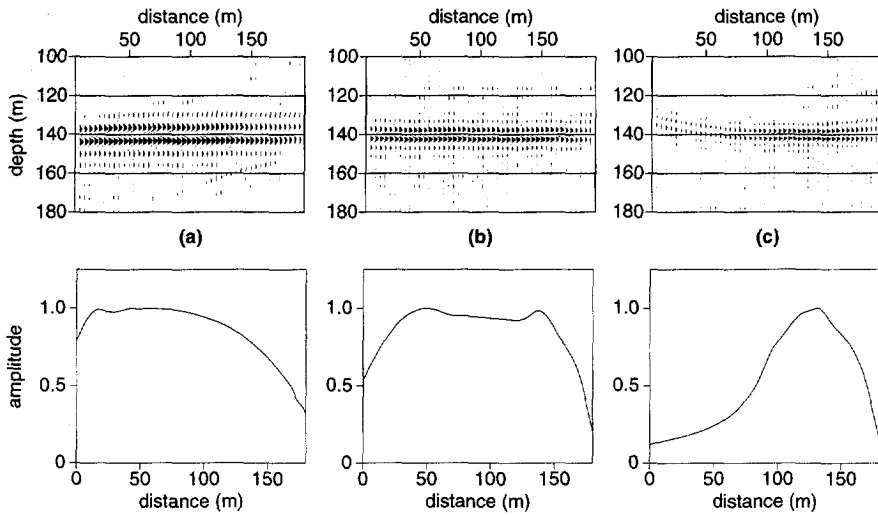


Fig. 3.9 Migration of plane wave responses for different plane wave incident angles α (see Figure 3.7). Top row: $R^+(x_m, z_n)$ image of the reflector. Bottom row: amplitude cross-section over the image of the reflector in the top row. (a) $\alpha = 70$ degrees. (b) $\alpha = 60$ degrees. (c) $\alpha = 50$ degrees.

the source array which effectively ends just above the reflector. This effect is more pronounced for the lower incident angles. On the right side, the direct wave removal procedure introduces some attenuation of the reflection response near the receiver well. For the smaller angle $\alpha = 50$ degrees the finite aperture effect from the top of the source array also influences the amplitudes of the illuminating wave field at the right side of the reflector. The deconvolution process however properly compensates for this effect during migration.

The example shows the trade-off that exists in crosswell migration between the imaging of lateral continuity and resolution. For high resolution images, it is necessary to illuminate under angles that are close to the vertical. But using these propagation angles means that the subsurface may be badly illuminated near the source well.

3.5 Concluding remarks

In this Chapter a new crosswell migration approach has been developed. The emphasis has been put on obtaining a structural image of the subsurface, by imaging zero-offset reflectivity. In the examples we have seen that the irregular acquisition geometry gives rise to an irregular illumination of the subsurface. For one horizontal reflector, this means that some points on the reflector will be imaged with larger amplitudes than other points. With respect to the interpretation

of a migrated seismic section, it is desirable that a horizontal reflector is imaged with the same amplitude from one well to the other. Thus, after migration, a post-processing step may be desirable to correct for the irregular illumination. This is shown in the examples presented in the next two Chapters.

Currently, new insights in seismic migration are maturing that may provide a means to correct for the irregular crosswell illumination effects. The concept of a 'common focus point' (CFP), which is briefly discussed in Appendix B, reformulates seismic migration in such a way that we have full control over the illuminating and detecting *focused beams*. The energy contained in the beams may be used to normalize the migrated section in every subsurface point in a physically justified way. This approach is however beyond the scope of this thesis.

Chapter 4

Synthetic data examples

To assess the accuracy and resolvability of the proposed crosswell migration scheme two case studies are presented. Optimum control over the experiments is achieved by generating the data artificially, using finite difference techniques. The finite difference method employs the full acoustic or elastic two-way wave equation in order to accurately model wave propagation in arbitrary inhomogeneous media (Kelly et al. (1976), Virieux (1986)). In this chapter only acoustic finite difference data is used. Furthermore, tube-wave and borehole coupling effects are not taken into account, and the data contains no noise. However, higher order effects such as multiple scattering are correctly modeled.

With respect to the modeled amplitudes, in field data the amplitude decay contains 3D geometrical spreading effects, whereas in the finite difference modeled data only 2D effects are present. In addition, in field data real-world attenuation effects may be present. As a consequence, in field data reflection events at later arrival times may be drowned in noise.

After processing the data, the obtained migration results can directly be compared to the original model, which is of course not possible for a field data case. Apart from studying the illumination and resolution aspects, the behavior of the extrapolation operators in inhomogeneous media is investigated.

4.1 Horizontally layered medium

4.1.1 Model and acquisition

For the first example a horizontally layered model is constructed, which is called a “1D” model because it only contains variations of the medium parameters along the vertical direction. For surface seismic migration a 1D model is considered to be a simple model. For crosswell migration the situation is more complicated, because the sources and detectors are situated in vertical boreholes. Thus, contrary to the surface seismic situation, a 1D medium actually can be strongly

inhomogeneous along the source and detector arrays. Due to the parallel layering, post-critical reflected waves and channeled waves may be present. Furthermore, because of the parallel layering, internal multiples have the same propagation angles as the primary reflected waves, and may interfere with later arrivals of primary reflected waves. It is also likely that refracted head waves are present, which may arrive earlier than the primary wave. This may cause problems in the pre-processing step while removing the direct wave.

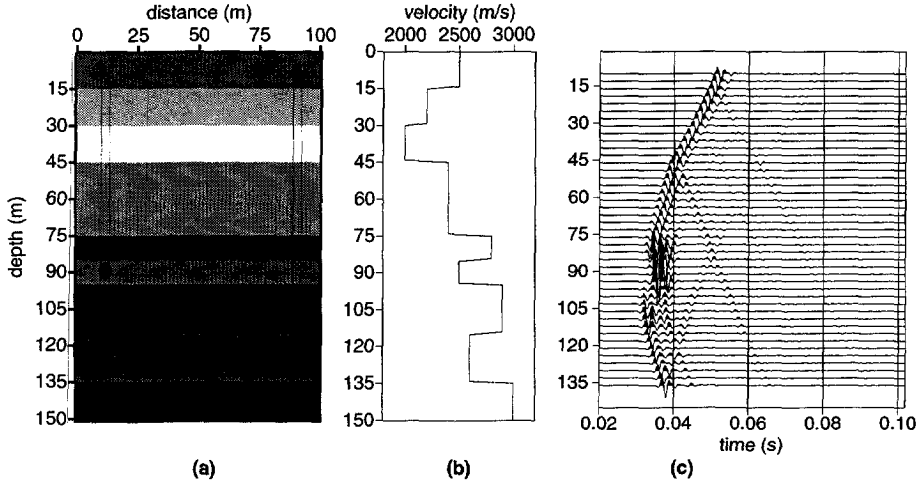


Fig. 4.1 (a) Model used for generating the synthetic data. The source and detector apertures are indicated, with the sources on the left and the detectors on the right of the model. (b) Vertical cross-section of the model. (c) Shot record obtained with the source at 90 m depth, as indicated by the dot in (a). Note that the time axis starts at 20 ms. The amplitudes are clipped at 50% of the maximum value.

The model is shown in Figure 4.1.a and is discretized with a spatial sampling of 1 m. A vertical cross-section of the model is plotted in (b) and shows the low velocity layer present around 90 m depth. The exact depths of the interfaces are 15, 30, 45, 75, 85, 95, 115 and 135 m from top to bottom. Both source and detector arrays start at a depth of 10 m. The distance between the boreholes is 80 m, leaving 10 m at both sides from the boreholes to the model edge. On the edges of the finite difference grid an analytical non-reflecting boundary condition is applied. This boundary condition is based on the work of Lindman (1975), which has been extended for general inhomogeneous media. For the source signature a Ricker wavelet is used with its spectral maximum at 350 Hz and a total bandwidth of 50-800 Hz. A total of 64 shots are fired with 128 detectors each. In Figure 4.1.c one shot record is shown obtained with the source at a depth of 90 m in the left borehole. In the shot record the direct wave can distinctively be observed. A relatively strong channeled wave is present in the low velocity layer. Some faint

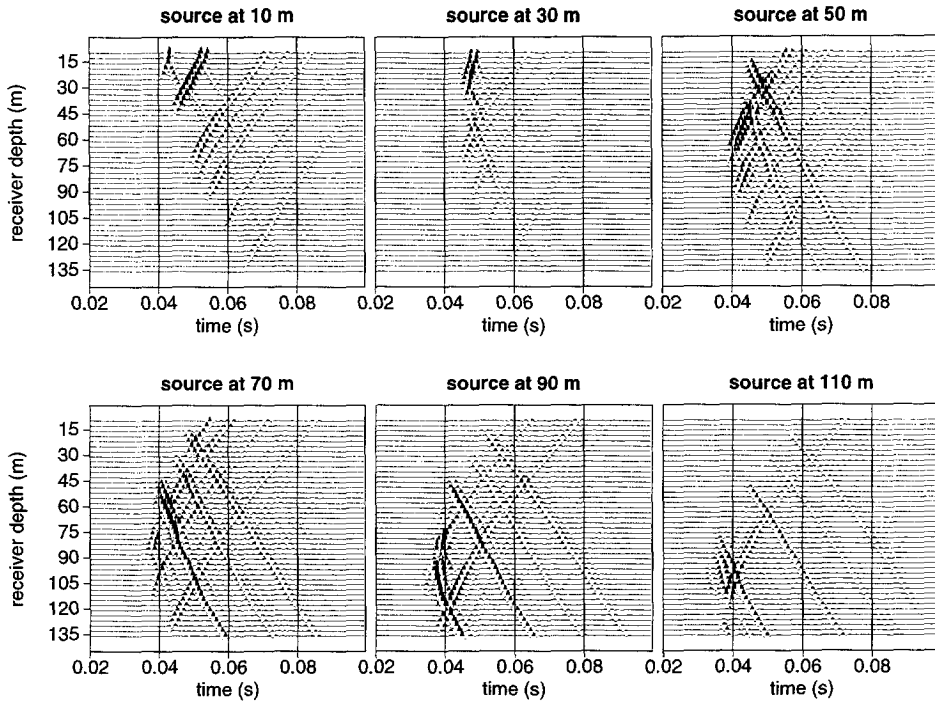


Fig. 4.2 Shot records for six different depths of the source, after removal of the direct wave. The shot record at 90 m depth may be compared with Figure 4.1.c. Note that the time axis starts at 20 ms.

reflected events are visible.

4.1.2 Pre-processing

In the pre-processing step the direct wave is removed from the total wavefield to extract the scattered wavefield. Appendix A describes in more detail the way in which this step is implemented. The direct wave removal procedure is applied in a totally automatic fashion, without interactive control and additional touch-ups.

Figure 4.2 shows six shots after removal of the direct wave. There is a significant difference between the amplitudes of the reflected wave events. Multiple reflected wave events are also clearly visible. Comparing the shot at 90 m with the original shot record in Figure 4.1.c, it can be seen that the direct wave removal procedure has not completely removed the guided wave direct arrival event. In the other shot records of Figure 4.2 some remnants of the direct wave can also be spotted. In the lower right shot record, a packet of multiple reflected events in the layer around 105 m depth can be seen.

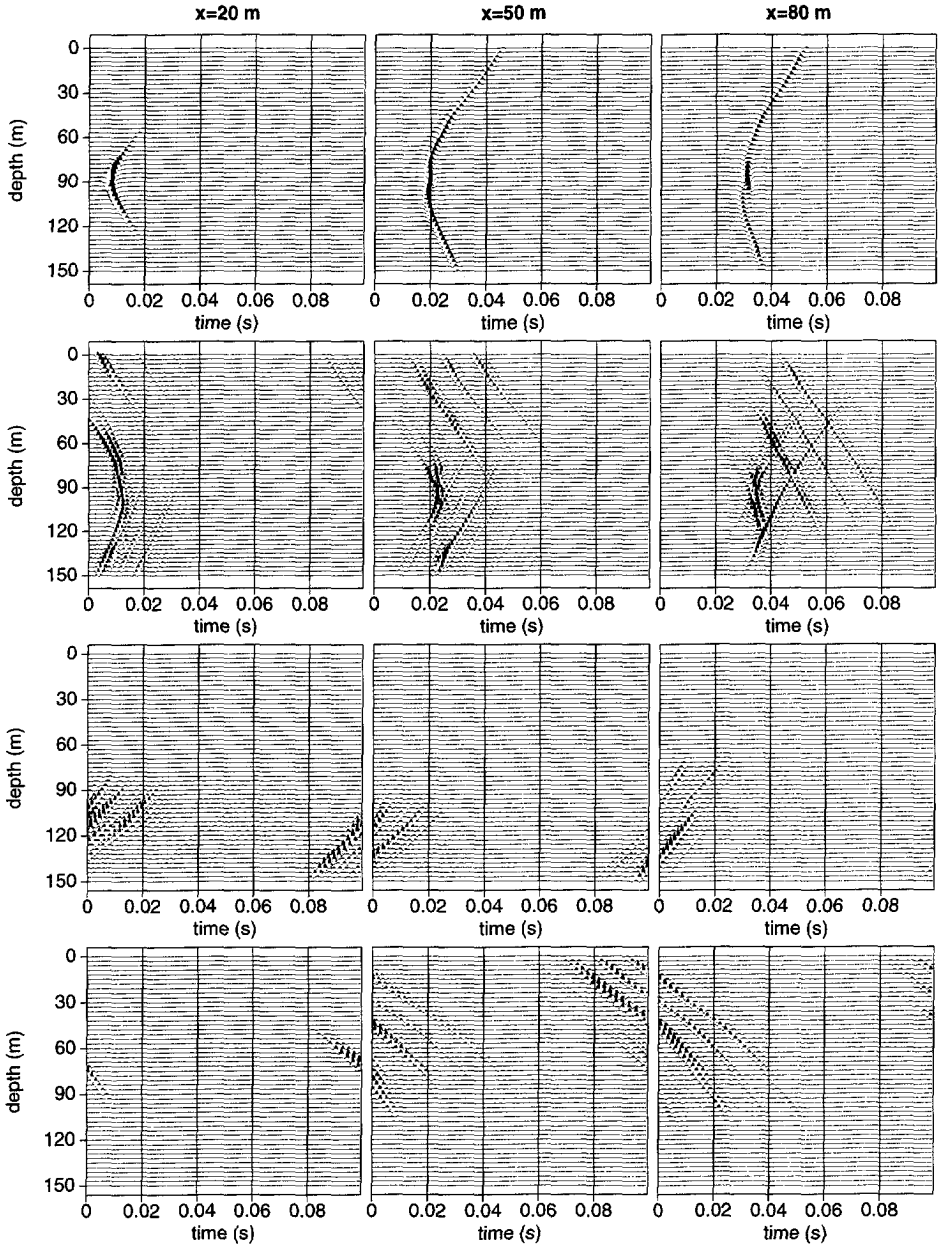


Fig. 4.3 Detailed visualization of the extrapolation and deconvolution process for the source at 90 m depth at vertical cross-sections (from left to right) $x_m = 20\text{ m}$, 50 m and 80 m . First row: forward extrapolated incident wavefield $\mathbf{P}_i^+(x_m)$. Second row: inverse extrapolated scattered wavefield $\mathbf{P}_s^-(x_m)$. Third row: result of deconvolving $\mathbf{P}_s^-(x_m)$ with $\mathbf{P}_i^+(x_m)$. Fourth row: result of deconvolving $\mathbf{P}_s^+(x_m)$ with $\mathbf{P}_i^-(x_m)$

4.1.3 Migration

In this case there is no need to image dipping layers, so the migration approach outlined in section 3.2.2 is taken. Thus, the wavefield is first separated into up- and downgoing waves, and subsequently the separated contributions are imaged. Figure 4.3 visualizes the procedure of wavefield extrapolation, separation and deconvolution in more detail for the data obtained with the source at a depth of 90 m. This again is the shot with the source in the low-velocity layer, which is a worst case situation for this model. Four types of intermediate results are visualized, at three different vertical cross-sections. From top to bottom, Figure 4.3 shows the forward extrapolated incident wavefield $\mathbf{P}_i(x_m)^1$, the inverse extrapolated scattered wavefield $\mathbf{P}_s(x_m)$, the result of deconvolving the upgoing scattered wavefield $\mathbf{P}_s^-(x_m)$ with the downgoing incident wavefield $\mathbf{P}_i^+(x_m)$, and the result of deconvolving the downgoing scattered wavefield $\mathbf{P}_s^+(x_m)$ with the upgoing incident wavefield $\mathbf{P}_i^-(x_m)$. From left to right, the data is shown at a cross-section of $x_m = 20$ m, 50 m and 80 m respectively.

As a smoothed macro velocity model is used, no significant scattered waves are generated during the extrapolation of the wavefields. This can be verified by inspecting the results of the forward extrapolated source wavefield. In these source wavefield panels it can also be observed that some energy is trapped in the low velocity zone.

The results shown in the second row of 4.3 are actually computed from right to left. From right to left, the downgoing events are traveling upwards and the upgoing events are traveling downwards. During extrapolation, an exponential taper to suppress artificial reflections from the boundaries of the model is applied to the edges of the model after each extrapolation step. In these figures it can be seen that, from right to left, the reflection events are absorbed at the top and bottom of the model. Another feature that can be observed is the effect of inverse extrapolating the remnants of the channeled direct wave. These remnants generate artificial tails that will cause artifacts in the final migrated image (see below).

The wavefields are separated into four contributions using convolutional filters in the space-frequency domain. In this example all waves with incident angles between -20 and 20 degrees with respect to the horizontal are suppressed. In the results after the deconvolution (third and fourth row of Figure 4.3) it can be seen that the events intersect the $t = 0$ axis at the position of the original reflectors. Essentially, the values at $t = 0$ in the third row of Figure 4.3 yield one vertical trace in the image of R^+ , and the values for $t = 0$ in the fourth row of Figure 4.3 yield one vertical trace in the image of R^- , at the positions $x = 20, 50$ and 80 m respectively.

The complete migrated sections of R^+ and R^- for the shot record with the source at 90 m depth are displayed in Figure 4.4. Only the part in between the wells is imaged. For reference, the velocity profile is also displayed. In the images, it can be seen that the reflecting interfaces have

¹Note that in the figures the wavefields are represented in the *time* domain, whereas the matrix expressions represent the wavefields in the *frequency* domain.

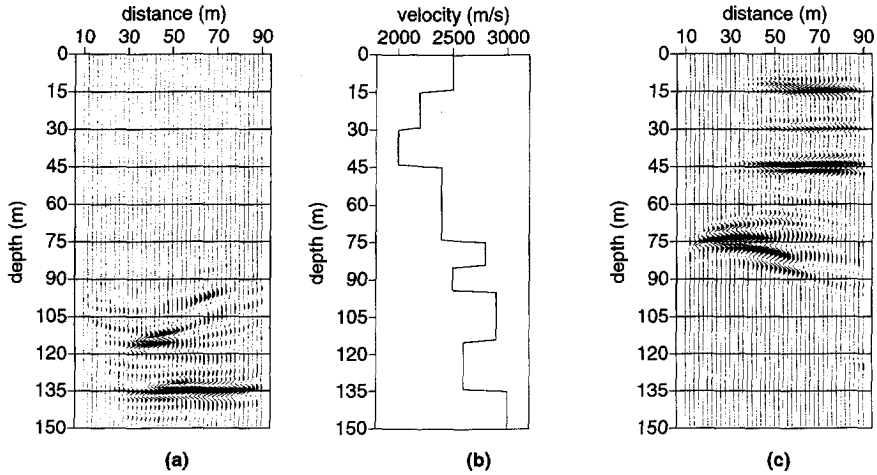


Fig. 4.4 Migration results for the shot with source at 90 m depth. (a) Reflectivity image of R^+ . (b) Velocity profile of original model (same as Figure 4.1.b). (c) Reflectivity image of R^- .

been resolved mainly towards the right side of the model. In (a), it can be observed that the right side of the interface at 115 m depth is badly illuminated. Also, there is a small artifact visible at a depth of 100 m. In (c), the upper reflecting interfaces have clearly been resolved but there are some artifacts visible near the source position, which can be attributed to the presence of the remaining channelled direct wave.

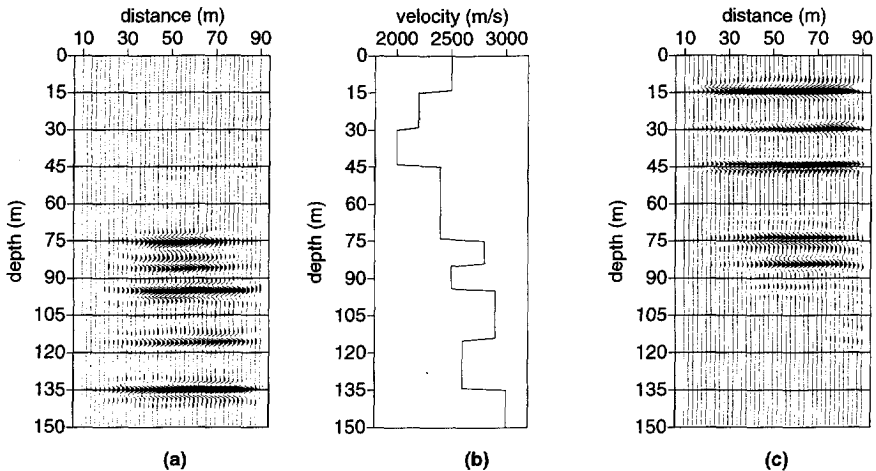


Fig. 4.5 Migration results stacked over all 64 shots. (a) Stacked reflectivity image of R^+ . (b) Velocity profile of original model. (c) Stacked reflectivity image of R^- .

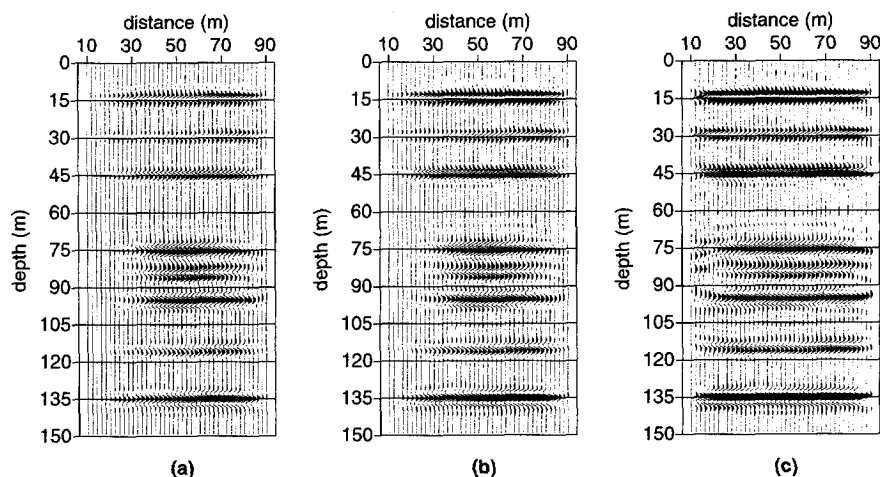


Fig. 4.6 Migration results stacked over all 64 shots and R^+ and R^- . (a) Plain stack over Figures 4.5.a and 4.5.c. (b) Same as (a), but amplitude normalized over depth. (c) Same as (a) after 2D amplitude normalization.

All 64 shots are now processed in one batch job and the results are stacked over separate R^+ and R^- sections. This yields the result shown in Figure 4.5. It can be observed that for the reflector positions at 75 m and 85 m the image in (a) has the opposite polarity compared to the image in (c). This is correct with respect to the theory. But, before stacking the two contributions, the sign of one of the migrated sections must be reverted. The results of this stacking procedure can be found in Figure 4.6. Figure 4.6.a shows the plain stack. Because of the contrasts in illumination over the model, an additional normalization to enhance the features that are not visible in the plot due to the limited dynamic range, is carried out. In Figures 4.6.b and 4.6.c, an additional amplitude normalization has been applied. In (b), a normalization is applied on (a) along the depth direction, by normalizing with a smoothed envelope of all stacked traces. Because the smoothing is performed with a 15 point/15 iterations simple averaging filter, the normalization function is changing relatively slowly over depth compared to the wavelengths that are present. The images of the reflectors in (b) have more equal amplitudes along depth than in (a). Figure 4.6.c shows the results of applying a 2D normalization by scaling with a smoothed envelope of the original stacked section (a). In this case the smoothing of the envelope has been carried out in two steps. A 15 point/15 iterations filter has been applied along the depth direction, followed by a 5 point/5 iterations filter along the horizontal direction. This procedure shows how the quality of the image near the source well can be improved. The normalization along the horizontal direction (partly) corrects for the bad illumination effects of the reflectors near the source borehole, as described in section 3.4. Of course, in practice caution must be taken in designing the normalization factors to avoid enhancing artifacts and noise.

4.2 AMOCO synthetic data set

For the second synthetic data example a finite difference modeled dataset is used which has already been published in the geophysical literature. The model was introduced by Carl Regone and Randy Read in an AMOCO-Western Geophysical study, and reported by Lines and Tan (1990). Results of a tomographic imaging and migration study were also shown in Hardage (1992). Gray and Lines (1992) discuss the latest results in more detail.

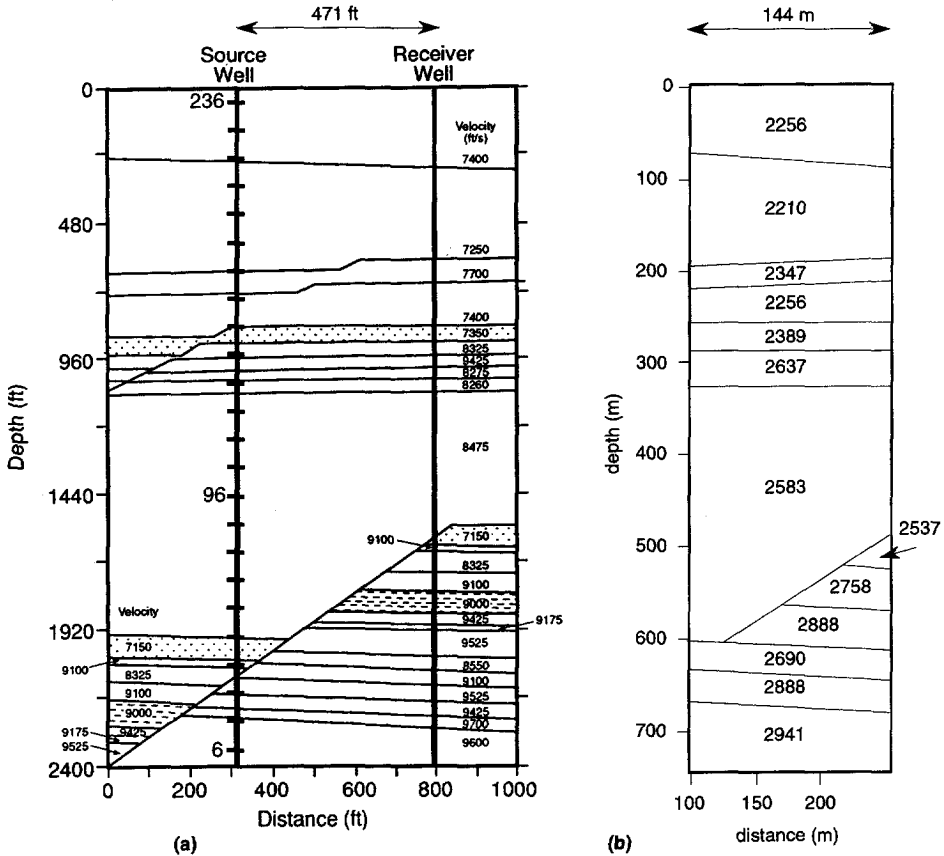


Fig. 4.7 (a) Stratigraphic velocity model used by AMOCO to generate synthetic acoustic seismic data for the testing of their Kirchhoff depth migration scheme. Velocities are given in ft/s. The shot numbers printed along the source well correspond to those in Gray and Lines (1992). (b) Macro velocity model obtained by digitizing and simplifying (a), as is used in this chapter for the migration step. Only the area in between the two wells is used. All distances are converted to meters. Velocities are given in m/s.

4.2.1 Model and acquisition

Figure 4.7.a shows the stratigraphic velocity model used by AMOCO to generate the data with. The original figure of the model has been scanned from the paper by Gray and Lines (1992). The velocities in the model range from 2179 m/s to 2957 m/s (7150 ft/s to 9700 ft/s). The model is 732 m (2400 ft) high and the distance between the boreholes is 144 m (471 ft). Note that the aspect ratio in Figure 4.7 is not correct; the width is too large. Actually, the model is about five times as deep as the offset between the boreholes. In addition, sources and detectors are present in their respective boreholes from the top to the bottom of the model. With respect to the possible incident and reflected angles, this configuration is a desirable one, which may in practice be difficult to achieve.

Compared to the model used in the previous example, this model is more complicated. The main feature is a normal fault at the bottom. In the shallow part of the model a small fault that extends beyond the left side of the source well is also present. Furthermore, a lot of relatively thin layers are present. Around a depth of 290 m (960 ft), three relatively large velocity changes (of approximately 300 m/s (1000 ft/s)) can be found in the package of thin layers. Thus, in that area ample internal multiple reflections are expected to be present. The largest velocity change of 594 m/s (1950 ft/s) is found near a depth of 512 m (1680 ft) at the receiver well, and near a depth of 610 m (2000 ft) near the source well. Figure 4.7.b shows the simplified macro velocity model that is used in the migration step (see section 4.2.3, below). It has been obtained by digitizing the main features of the original model. In 4.7.b SI units are used, and thus velocities are given in m/s.

As performed in Gray and Lines (1992), only one shot out of ten of the original common shot gathers are used. In Figure 4.7.a, the corresponding shot positions are indicated by the horizontal bars crossing the source borehole. When processing the data, the five bottommost shot records appeared to contain less traces than the rest of the shot records. As a result, they were not used. In total, starting from a depth of 12 m (40 ft), 24 shots are used with a spacing of 30.48 m (100 ft) between the shot positions. The receiver spacing is 3.0 m (10 ft), with receivers present from 0 m to 735 m (2410 ft). To accommodate for the bottommost receiver, the model shown in Figure 4.7.a actually is extended over another 3 m using a velocity of 2941 m/s.

4.2.2 Pre-processing

The dominant frequency band in the data appeared to be centered around 200 Hz. The maximum frequency in the data is about 500 Hz. To minimize processing time, the data is first low-pass filtered with a high-cut frequency of 600 Hz, and next resampled to 0.8 ms. Then, the first arrival times are picked and used to mute the direct wave arrivals (see Appendix A). Figure 4.8 shows the original and pre-processed data for two interesting shot positions. The top two panels show the original shot records, clipped at 10% of their respective maximum values. The bottom

panels show the pre-processed data. At 317 m (1040 ft) depth the source wavefield is directly emitted into a package of layers. This results in a lot of internal multiples which are difficult to

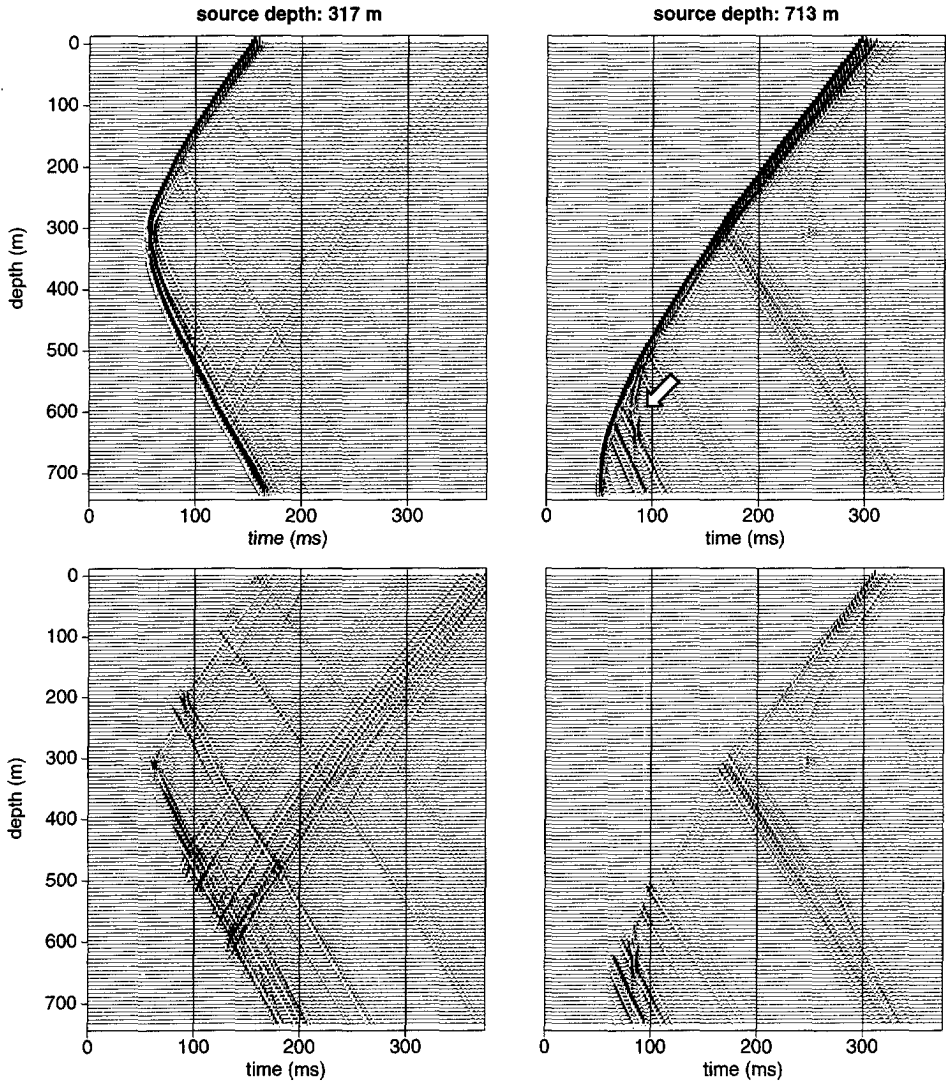


Fig. 4.8 Original and pre-processed data for two shot positions. Top row: original data, clipped at 10% of absolute maximum value. Bottom row: pre-processed data after the direct wave removal procedure, clipped at 50% of absolute maximum value. Left: shot at 317 m depth. Right: shot at 713 m depth. The arrow indicates the reflection from the fault at the bottom of the model.

distinguish from the direct wave field, forming “tails” behind the direct wavefield. After muting the direct waves (bottom-left panel in Figure 4.8), there is still energy present near the source depth, which is due to a channeled wave. Also, at larger depths, the tails due to the internal multiples are clearly visible. The second shot, fired at a depth of 713 m (2340 ft), illuminates the large fault at the bottom. In Figure 4.8 the reflection event from the fault plane is indicated by the arrow in the original data panel. Note however that, when comparing the top-right panel of 4.8 with the bottom-right panel, the upper part of the reflection event is partly removed by the direct wave muting procedure.

Overall, from the pre-processed data it can be seen that the reflection events are relatively clean and noise free, whereas for field data the wavefield may be much more complicated. The amplitudes of the scattered data only moderately decay in time, because the geometrical spreading effects are 2D and there is no attenuation. This synthetic data set however proves to be suitable for a controlled crosswell migration experiment, because it contains reflection events from isolated reflectors, layers thinner than the used wavelengths, and strongly dipping faults.

4.2.3 Migration

Since the objective is to image both the near-horizontally layered structures and the dipping faults, the migration approach outlined in section 3.2.3 is taken. This means that at each vertical cross-section x_m first a deconvolution process of the inverse extrapolated pre-processed wavefield with the forward extrapolated source wavefield is carried out. Then, the imaging step extracts the reflectivity information, after separating the contributions from the top and bottom of the layers. The separation operators that are used in this example suppress angles between -10 and $+10$ degrees with respect to the horizontal axis, and are applied to the deconvolved data.

Figure 4.7.b shows the macro velocity model that is used in the extrapolation of the wavefields. Only the main contrasts are accounted for, and the velocities in the different areas are averages of the velocities in the respective areas of the actual model. The macro velocity model closely resembles a model that would have been obtained after carrying out the macro model estimation step of Chapter 2. However, for this example, a true macro model estimation step is not attempted.

Instead of trying to estimate the source signature, it is decided to leave the source wavelet in the data. To approximate a zero phase wavelet, an extra negative time shift of 3 ms is applied to the data. This time shift is the approximate time from the first break of the wavelet to the maximum peak, and is extracted from the direct wave arrivals.

First the migration results for the two pre-processed shot records of Figure 4.8 are presented. Figure 4.9.a shows the interwell image obtained from reflections at the top of the layers for the shot with the source at 317 m depth. At the bottom, several layers are partly resolved. Figure 4.9.b shows the corresponding image obtained from reflections at the bottom of the layers. As

expected, in both Figures 4.9.a and 4.9.b the remnants of the direct wave cause some artifacts around the source depth. At the top of image 4.9.b, part of the shallowest interface is visible. However, the most interesting feature is the image of the shallow fault. This fault is well illuminated and imaged at the correct position.

Figures 4.9.c and 4.9.d show the images obtained from reflections at the top and bottom of the layers, respectively, for the shot at 713 m depth. This shot is the bottommost shot. Note that the images do not show direct wave related artifacts. In theory, image (c) should be totally empty. The relatively small residue that is still visible demonstrates the performance of the separation operators. Figure 4.9.d shows that part of the lower fault has been properly imaged, although with relatively low resolution. The low resolution is due to the relatively small difference between the angles of the incident and reflected waves at the fault. The top part of the fault is not resolved, because that part of the response has been muted by the direct wave removal procedure.

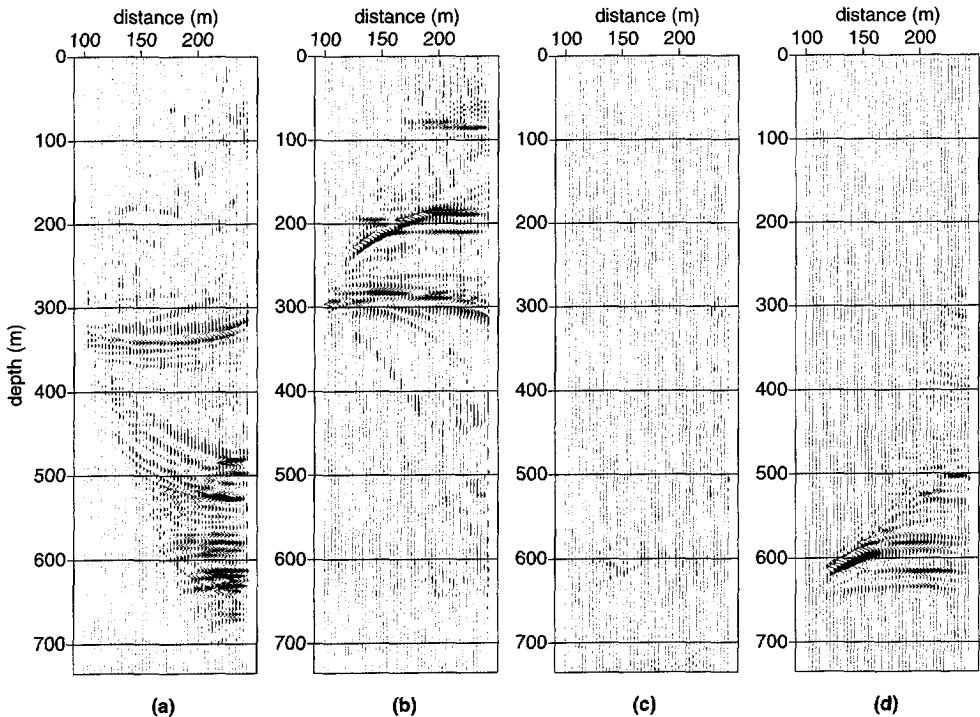


Fig. 4.9 Migration results for two single shots. (a) Image of reflections from top of layers for shot at 317 m. (b) Image of reflections from bottom of layers for shot at 317 m. (c) Image of reflections from top of layers for shot at 713 m. (d) Image of reflections from bottom of layers for shot at 713 m. Figures (a) and (b) are plotted with the same amplitude scale, and similarly (c) and (d) are plotted with the same amplitude scale.

ture, as has been shown above.

With respect to the direct wave related artifacts, this shot is an exceptional one; in most shot records of this experiment the direct wave is removed more successfully (not shown here). In practice, if the artifacts appear to be relatively strong and are thus still visible in the final stack, the remaining direct wave energy must be identified in each shot record and muted manually before migration. Note again that manual editing is not performed in this thesis. All processing steps are equally applied on all shot records of a given dataset.

Figure 4.10 shows the stacked results for all 24 migrated common shot gathers. Figure 4.10.a shows a plain stack of all images of reflections from the top of the layers, and (b) from the bottom of the layers. In (a) the upper fault is not imaged because it has not been properly illuminated. In (b) the fault is clearly visible, and the images of the interfaces of the faulted layer have the correct relative polarity. In the package of layers around 300 m depth, several interfaces can be identified separately. However, the large amount of internal multiples distorts the lateral conti-

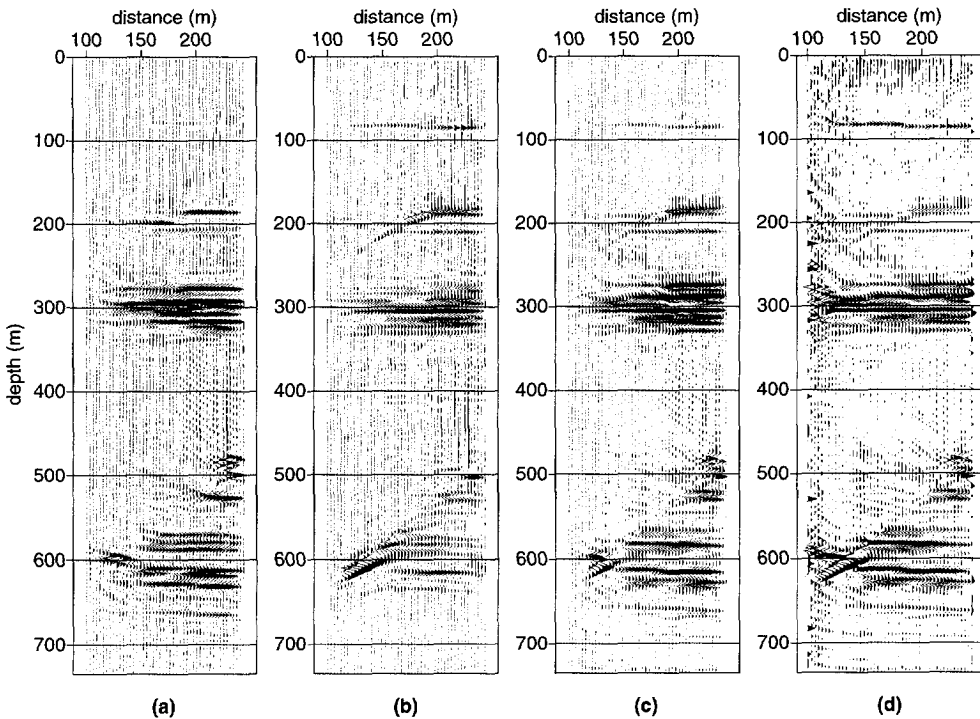


Fig. 4.10 Migration results, stacked over 24 migrated shot records. (a) Reflections from top of layers. (b) Reflections from bottom of layers. (c) Stack of (a) and (b). (d) Same as (c) after amplitude normalization.

nuity and causes some artifacts to be imaged in between the layers. At a depth of 293 m (960 ft), there is a relatively strong top-down velocity increase (2537-2873 m/s (8325-9425 ft/s)), which is properly imaged in (b). Just below this event, the image due to a relatively strong velocity decrease (2873-2522 m/s (9425-8275 ft/s)) can be found. In both panels (a) and (b) of Figure 4.10, between 350 and 500 m, some noisy artifacts can be seen which are due to remaining direct wave energy. At the left side of (a), just above 600 m depth, the slightly dipping top layer of the graben (hanging wall block) is imaged. Note that this part of the subsurface is not present in the macro velocity model. In (a), the structure of the horst (footwall block) can be derived from the outline of images of the layers in that area. The end of the layers resolves the position of the fault plane. In (b) the lower part of the fault is actually imaged, as in Figure 4.9.d.

Comparing Figures 4.10.a and 4.10.b, the opposite polarity and the position of most of the events are consistent. Hence, the two images may be stacked by multiplying one of the images by -1 before stacking them. This stack is displayed in Figure 4.10.c. Finally, in (d), the same stack as in (c) is displayed, after applying an AGC with a window length of 300 m. The large amplitudes in the region of the layers around 960 ft depth are suppressed. This shows the image of the shallowest interface better, just above the 100 m grid-line. Note that this interface is supposed to have a slight dip, but because of the gridding involved when using finite-difference modeling, actually a "staircase" step is modeled instead of a smooth interface. The step can be observed in (d), showing the high resolution of the imaging algorithm. Towards the source borehole, the signal to noise ratio decreases. This may be expected because of the generally poor illumination of reflectors near the source borehole (see section 3.4).

Figure 4.11 shows the results obtained by Gray and Lines (1992). Regretfully, the results in Gray and Lines (1992) are printed as clipped gray-scale images which are difficult to reproduce and interpret. Note that the figures in the original article are of only slightly better print quality than those displayed in Figure 4.11. Gray and Lines (1992) do not give the results after combining the two panels in Figure 4.11. Comparing the results with those displayed in Figure 4.10, it may be concluded that the resolution and number of resolved features are comparable. The top fault looks better resolved in Figure 4.11.b than in Figure 4.10.b. On the other hand, comparing Figure 4.10.a with Figure 4.11.a, the horizontal resolution at the bottom part seems to be better in Figure 4.10.a than in Figure 4.11.a, where in the latter some stretching artifacts are visible. At the sides, 4.11 also exhibits stretched artifacts. Therefore, the fault at the left of the source well is resolved with little success. In this chapter, imaging of the fault to the left of the source borehole is not attempted at all.

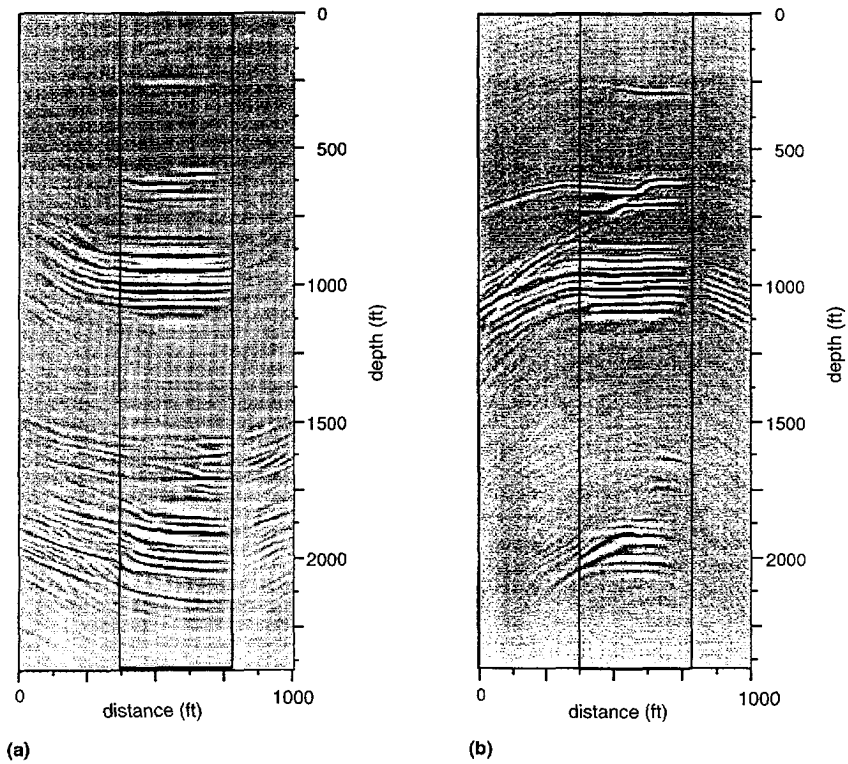


Fig. 4.11 Results reproduced from Gray and Lines (1992). (a) Stack of images from upgoing reflections. (b) Stack of images from downgoing reflections. The gray-scale images were scanned from the original article. The horizontal axis range has been corrected, and rectangular insets were added to indicate the area between the two boreholes which is imaged in this chapter.

Chapter 5

Field data example

In this chapter a field data case-study which addresses the processing steps for real data in a detailed way, is presented. In comparison to synthetic data processing, in the real data case especially the pre-processing step is more extensive.

In Findlay et al. (1991) a crosswell experiment is described which is carried out in an opencast coal exploration site in the United Kingdom at Lowther South, Yorkshire. A dense grid of boreholes is drilled with a typical borehole spacing of 40-60m to obtain the necessary information on the coal reserves and geological structure. The close spacing makes the site attractive for the testing of crosswell surveying. Furthermore, crosswell techniques may actually help opencast coal exploration in detecting small faults, to improve the estimation of coal reserves and to locate old mineworkings more accurately. Data of the first experiment, described in Findlay et al. (1991)¹, is used in this chapter for crosswell processing. The results are compared with those of Findlay et al. (1991).

5.1 Data acquisition

The data is acquired across relatively undisturbed ground. The boreholes are 41 m apart. Detonators and hydrophones are positioned at 2m intervals in (near) vertical boreholes. Thus, only single component data is recorded. The depth range of the sources is 10-62 m, while the detectors are placed between 16 to 60 m. Small explosive charges are used for the sources, with, according to Findlay et al. (1991), a typical bandwidth of 200-500 Hz. An accurate time break is obtained by wrapping a wire around the detonator, which blows open-circuit when the shot is fired.

With a pendulum-type inclinometer, the deviation of the boreholes from the vertical is measured. The largest deviation is found at the bottom of the boreholes, and is about 3 m. Neigh-

¹More recent work can be found in Gouly (1993) and Rowbotham and Gouly (1994).

boring boreholes tend to deviate by the same amount in the same direction. Therefore, vertical boreholes are assumed.

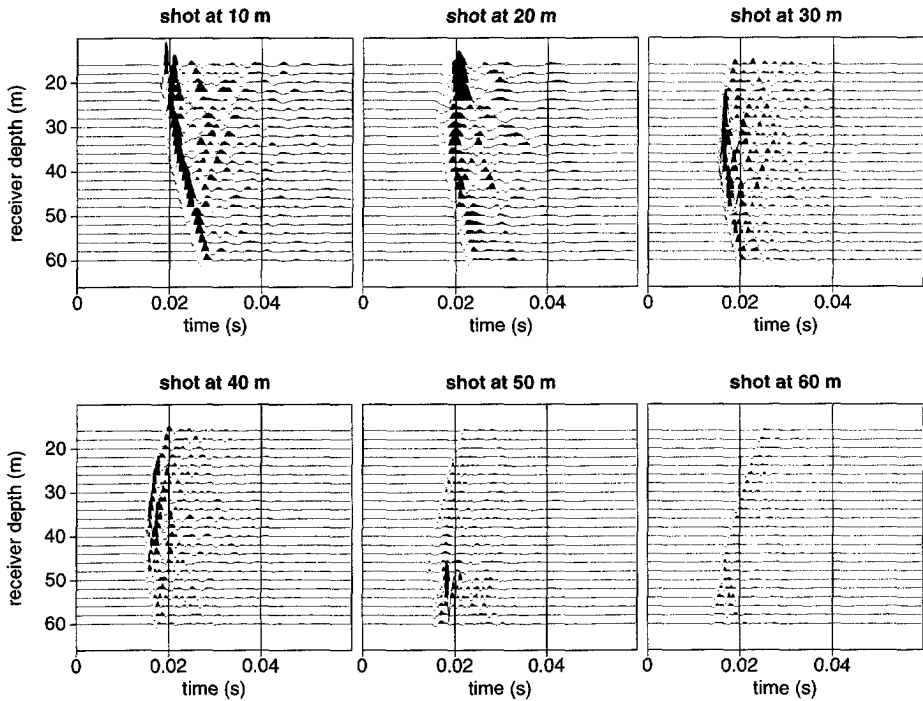


Fig. 5.1 Selected raw common-shot records. The shot depth is indicated. The scaling in the plots is the same for all shots, and is based on the maximum value of the shot at 30 m depth. Only the shot at 50 m depth is clipped, at 77% of its maximum value, because of the excessive amplitude recorded by the hydrophones around 50 m depth.

Figure 5.1 shows 6 raw shots out of the total 27 shots that are used in this chapter. The shots are all plotted on the same scale. Some important features of this dataset are visible. The main characteristic is the variation of the global amplitudes of the wavefields over both shot and receiver positions. It appears that the sources at the top cause the largest amplitudes to be recorded, while for deeper shots the amplitudes gradually decrease. Comparing the maxima of the direct wave in each shot record, the largest value is about five times larger than the smallest value. These differences are attributed to a varying source and hydrophone coupling.

The direct wave arrival is well defined. But the amplitudes of the direct arrivals also exhibit an irregular variation over hydrophone depth. Especially for the shot at 50 m depth in Figure 5.1 it can be seen that one hydrophone recorded a relatively large amplitude direct wave arrival (in the Figure the event is actually clipped at 77% of its maximum value). This is attributed to the

presence of some water-saturated old coal seam workings at that depth. Thus, at 50 m depth, both the source and hydrophone are relatively well coupled.

With respect to the frequency content, Figure 5.1 clearly shows that the shots also differ in temporal bandwidth. In particular, the shot at 20 m does not contain useful energy beyond 500 Hz, whereas in the other shots shown in the figure, some traces contain useful energy up to 750 Hz.

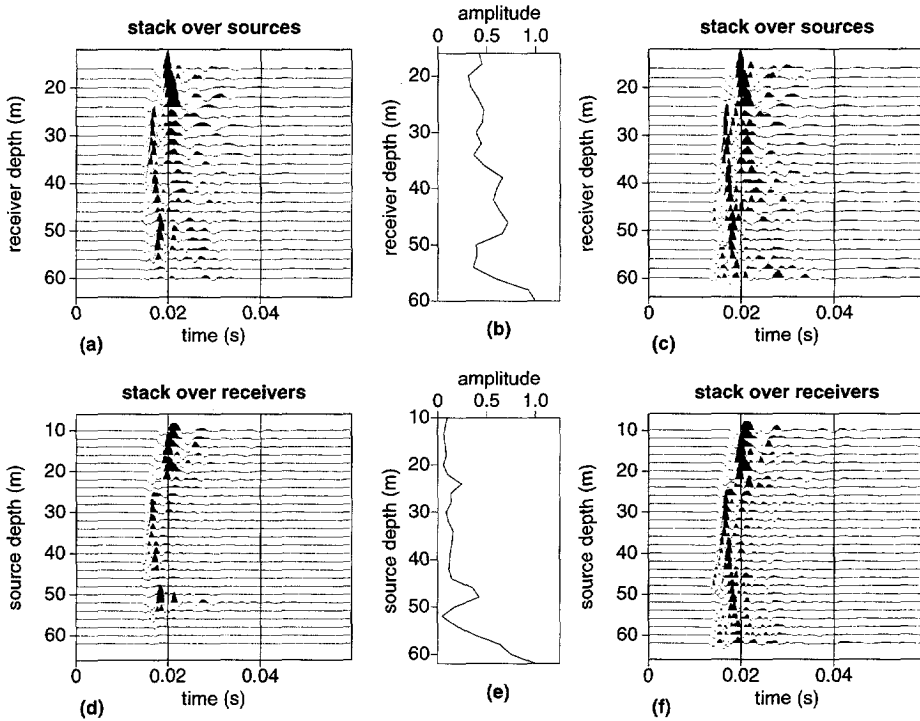


Fig. 5.2 Energy-balancing over sources and receivers. (a) Stack over sources before balancing. (b) Net correction factors applied to all receivers traces. (c) Stack over sources after balancing. (d) Stack over receivers before balancing. (e) Net correction factors applied to all common shot gathers. (f) Stack over receivers after balancing.

5.2 Pre-processing

Because of the difference in amplitude between the traces the first pre-processing step consists of trace-balancing. The objective is to remove the differences in coupling over sources and hydrophones, because the migration algorithm expects a uniform response for the sources and receivers. The following approach is taken (see also Appendix A).

If we fired all shots simultaneously, the total energy recorded by each hydrophone is expected

to be approximately the same. Similarly, if we summed the energy over all hydrophones for a single shot, the summed energy is expected to be comparable for each shot. Thus, by stacking over all sources and by computing the energy, a correction factor is obtained for each receiver, and by stacking over all receivers, a correction factor is obtained for each source. The former is applied to each individual receiver trace, the latter is applied to all traces of each shot record. This correction procedure may be applied in an iterative fashion.

Figure 5.2 shows the results of the trace-balancing procedure in more detail. Figure 5.2.a shows a stack over all raw shot records. The energy in each trace of this stack is computed. Figure (b) shows the inverse of the square-root of the energy for each receiver trace in (a). Next, the correction factors in (b) are applied to all respective receiver traces of each gather. Similarly, a stack over all receivers for each source gather is computed, shown in (d), which yields the correction factors displayed in (e). In this case, the balancing is done twice and actually (b) and (e) are the net correction factors obtained after two iterations. The correction factors do not change significantly after a third iteration. For comparison, (c) and (f) show the stacks of (a) and (d) after trace balancing. Note that the amplitudes of the first arrival in the stacked sections have become more uniform along depth.

Note that in balancing traces over common shot and common receiver gathers, the objective is to remove coupling effects without affecting the amplitude information in the scattered wavefield. A brute approach would be to simply normalize the maximum amplitude of all single traces in the dataset. In that case, the amplitude information of the scattered and reflected waves would be severely distorted. By using an approach which normalizes in a more averaging manner, as has been described above, the scattered wave amplitude information is better preserved.

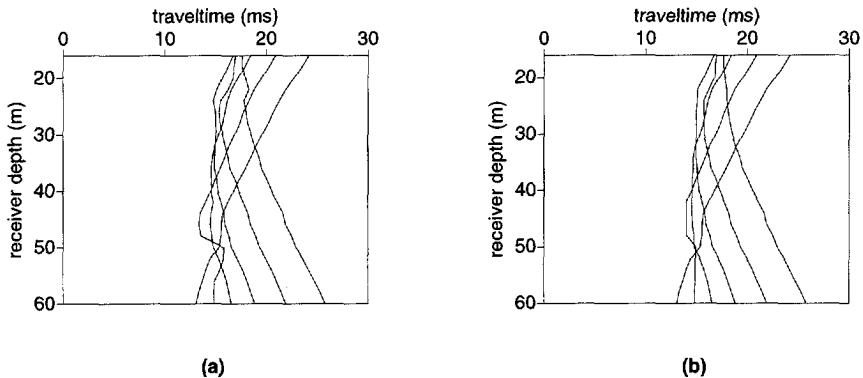


Fig. 5.3 First arrival picking results, for the shots displayed in Figure 5.1. (a) Raw picks. (b) Picks after applying an alpha-trimmed median filter.

The next pre-processing step consists of the picking of the first arrivals, which are used in the removal of the direct wave and in the estimation of the macro velocity model. In this dataset,

the first arrivals are of relatively good quality. They can be picked automatically, directly from the shot records; there is no need to re-order the data and perform the picking in another domain (i.e. common offset). Figure 5.3 shows the result of picking the (trace-balanced) shot records for the shot positions used in Figure 5.1. Figure 5.3.a shows the raw picks, and (b) shows the picks after applying an alpha-trimmed median filter (Stewart (1985)), to remove outliers. One iteration of a 7-point median filter is used with alpha-trim factor $\alpha = 0.5$. The alpha-trim version of the median filter can be seen as a smoothing operator which aims at preserving edges while removing spikes. The filtered picks are more continuous than the raw picks, although the difference is relatively small because the direct wave events already have a relatively good signal to noise ratio.

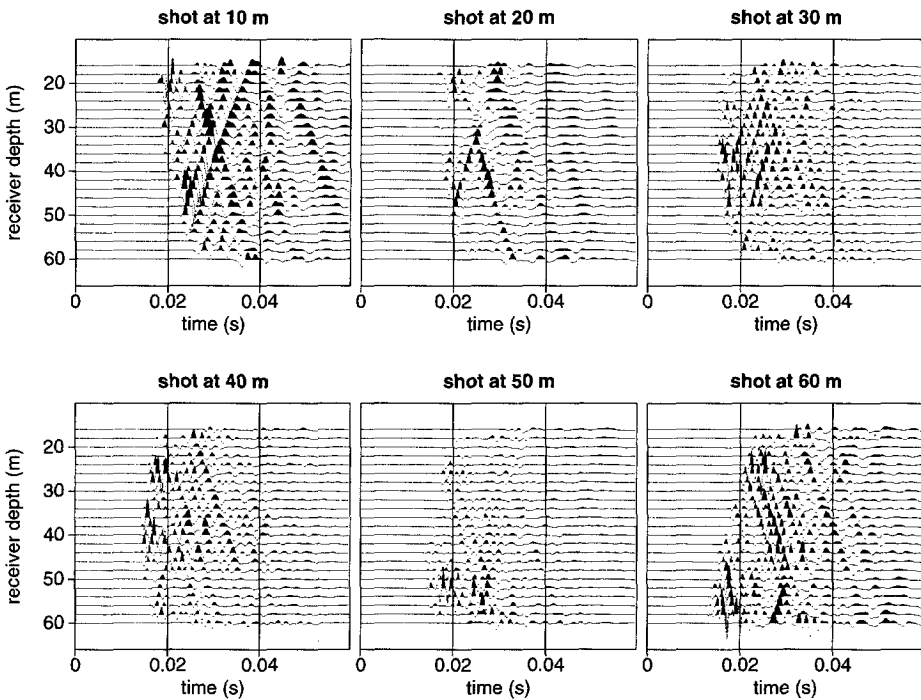


Fig. 5.4 Selected pre-processed common-shot records. The shot depth is indicated. The scaling in the plots is the same for all shots.

Using the first arrival picks, the direct wave event is removed from each shot record using the procedure described in Appendix A. In addition, an f - k filter is applied to all shot records to suppress tube-wave energy. Finally, a time gain is applied to all traces by multiplying with the square-root of the time. This operation adapts the amplitudes from a 3D to a 2D situation.

Figure 5.4 shows the shot records of Figure 5.1 after pre-processing. Distinct reflection events

are now clearly visible. In the raw shot at 20 m in Figure 5.1 a tube-wave event can be seen, emerging at about 30 m depth and traveling downwards. In Figure 5.4 this event is readily suppressed after pre-processing with the f - k filter. Note that, compared to surface seismic acquisition, most reflection events extend over relatively few traces. In typical surface seismic acquisitions, about 150 to 250 traces are recorded for each shot, which may all record the response of a particular reflector. Here, only about 10 traces are recorded for a reflector in the middle of the geophone aperture, and about 20 traces for a reflector at the top and bottom of the aperture. In addition, there is a masking effect due to the presence of the coal seams. For example in the shot at 30 m depth in Figure 5.4, the hydrophones deeper than 50 m show a decreased signal to noise ratio.

5.3 Macro model estimation

From the picked first arrival times, a macro velocity model that can be used in the migration must be estimated. The nonlinear Bayesian inversion approach of Chapter 2 is used. Important considerations are the choice of the a priori model and the initial model. Strictly, the a priori model must be chosen using information which is independent of the crosswell seismic measurements. In this case no well-logs or other seismic data other than the position of some thin coal seams, are available. However, we know that the subsurface is relatively undisturbed and near-horizontally layered. Therefore, a horizontally layered model is taken for the a priori model. With respect to velocities the only a priori knowledge available is the tendency of velocity to increase with depth, due to an increasing overburden pressure. Velocity values with a relatively high standard deviation are assigned to the a priori model.

The initial model may be based on the actual data. It is chosen to compute the initial velocities from the picks of a vertical plane wave illumination response. This is the stack shown in Figure 5.2.c. Figure 5.5.a shows the results of the picking procedure. In Figure 5.5.b the picks have been converted to velocities by using a borehole offset of 41 m. A trend can be seen: the velocity tends to increase with depth. Only around 50 m depth, a sudden velocity drop is present. This is due to the worked coal seam, which is water filled.

Based on the relatively simple lithology that is known to be present, a macro velocity model with only three different layers is chosen. The model has a depth of 100 m in total. The top layer starts at the surface and extends to a depth of 25 m, followed by a layer down to 50 m depth, and finally the deepest layer ranges from 50 m to 100 m depth. The a priori velocity in the layers is taken as 2600 m/s, with a relatively high standard deviation of 500 m/s. The start model velocity values for the three layers are based on Figure 5.5.b, and taken as 2500, 2750 and 3000 m/s from top to bottom.

In the inversion, the a priori standard deviation on all picked traveltimes is set to 0.50 ms. This means that the 95% confidence interval is 1 ms (5 samples) around the picked break. Figure

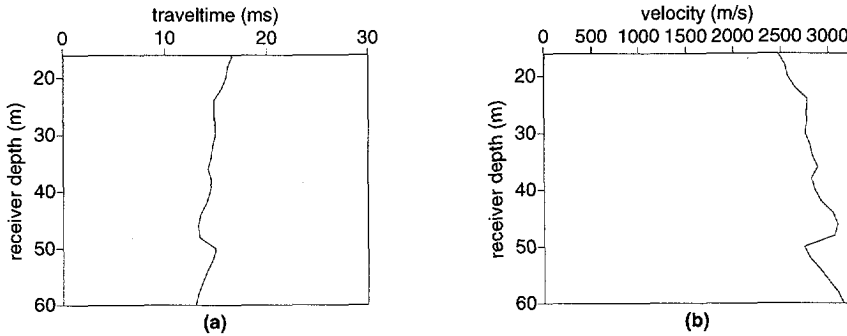


Fig. 5.5 (a) Picks of stacked section displayed in Figure 5.2.c. (b) Picks of (a) converted to velocities using a distance of 41 m

5.6.a shows the results of the macro model estimation step. At the bottom, the estimated velocity values can be found with corresponding a posteriori standard deviations. It can be concluded that accurate estimates of the velocity values have been obtained. The average absolute traveltime mismatch per ray has decreased from 0.65 ms to 0.51 ms. This indicates that the initial model was already close to the optimal solution. But, when using this model in the migration of the data, it appears that some major events do not lign up over all shot records (not shown here). Because of the presence of coal-seams, it is suspected that a certain amount of anisotropy is present. To test for anisotropy, two additional macro model estimation experiments are carried out.

First, the possible ray-paths are divided into two sets, by separating rays with an angle α with respect to the horizontal, with $-25 < \alpha < 25$ degrees, from the rest of the rays. Subsequently, the data corresponding to both sets of rays are separately used for macro model estimation. Figure 5.6.b shows the ray-paths and inversion results for $-25 < \alpha < 25$, and Figure 5.6.c shows the results for the complementary set of ray-paths. In (b) the average absolute traveltime mismatch per ray has decreased from 0.48 ms to 0.30 ms, and in (c) it decreased from 0.84 ms to 0.46 ms. It appears that in (b) the estimated velocities are significantly *higher* than in (a), and in (c) the estimated velocities are significantly *lower* than in (a). Furthermore, from the final average traveltime mismatches, it may be concluded that models (b) and (c) better predict the traveltimes than (a), where all ray-paths have been used at once. These results are a strong indication for the presence of anisotropy.

5.4 Migration

Recall that to obtain the highest possible resolution along depth, we have to properly image reflection events that travel along near vertical paths. Therefore, the macro velocity model of

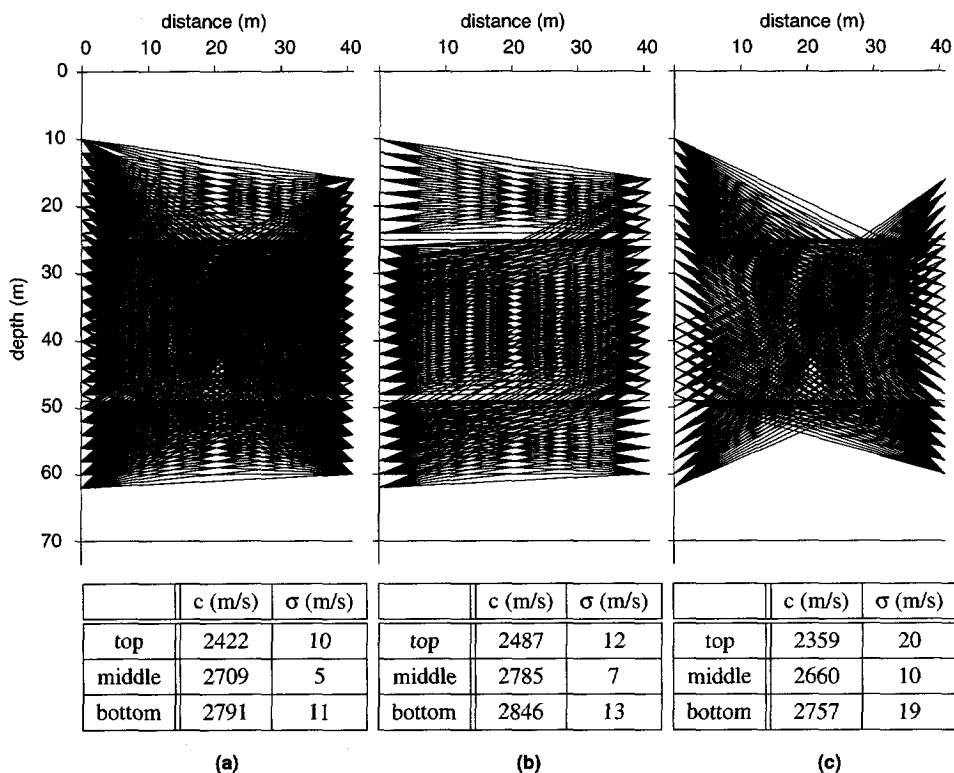


Fig. 5.6 Raypaths used in three macro model estimation experiments, with the tabulated estimated velocity values and standard deviations for all three cases shown in the tables. The model consists of three layers, separated by interfaces at 25 and 50 m depth. Sources are placed on the left side, detectors on the right. (a) All raypaths used. (b) Half the number of raypaths of (a) used, with smallest incident angles with respect to the horizontal at each source position. (c) Other half of raypaths used.

Figure 5.6.c is chosen. As in the data reflection events are identified from deep reflectors, the estimated macro velocity model is extended to 100 m depth, using the velocity of the bottom layer. The grid distance is set at 1 m, which is half the source and detector spacing, in order to avoid spatial aliasing.

As there are no steep dips to be imaged, the migration approach of section 3.2.2 is taken. First, the propagation effects are removed by forward extrapolating the source wavefields and inverse extrapolating the scattered wavefields. Then, at each vertical cross-section x_m , the wavefields are separated into up- and downgoing waves which are finally imaged (see equations (3.76) and (3.77) on page 63).

Figure 5.7 shows the process of inverse wavefield extrapolation for the two shots at 30 and 60 m

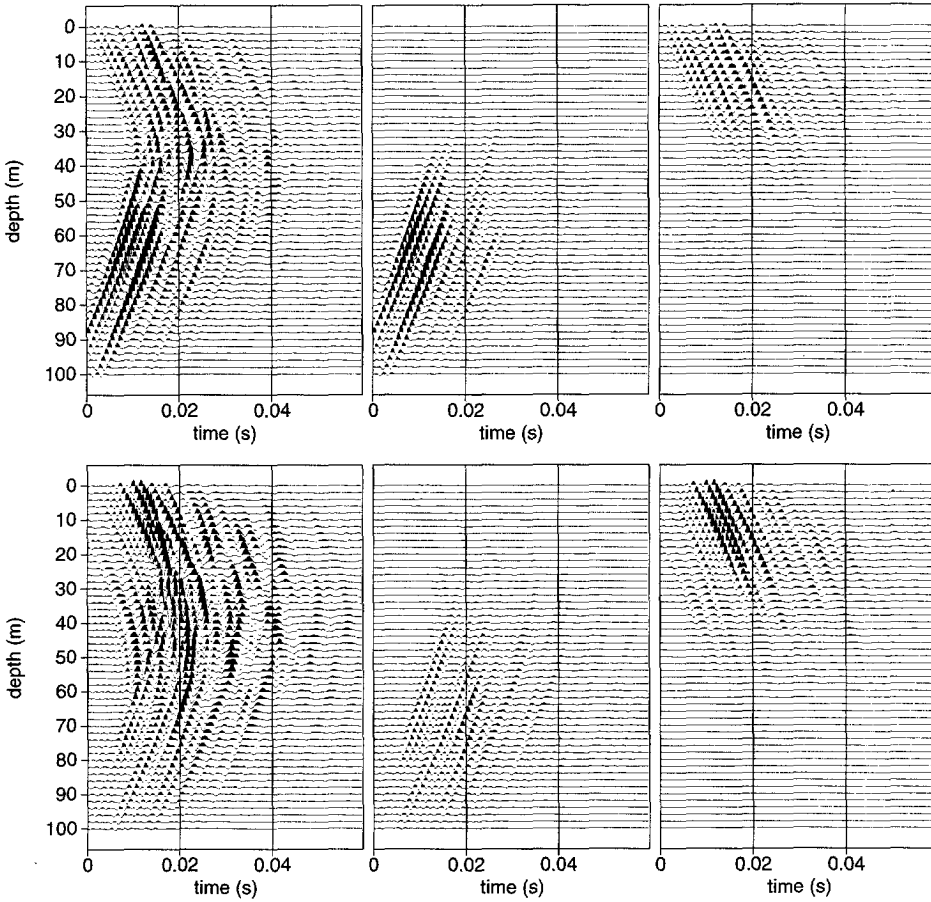


Fig. 5.7 Inverse extrapolated and separated wavefields at vertical cross-section $x = 20$ m for two shots. The scaling in all the plots is the same. Top row: source at 30 m depth. Bottom row: source at 60 m depth. Left: Inverse extrapolated shot records. Middle: downgoing wavefields. Right: upgoing wavefields.

depth. The original data at the receiver borehole can be found in Figure 5.4. At the top row of Figure 5.7, the total inverse extrapolated wavefield at $x = 20$ m is displayed with the corresponding separated wavefields for the shot at 30 m depth. At the bottom row, the equivalent results are shown for the shot at 60 m depth. It can clearly be seen that the downgoing wavefields have moved upwards, and the upgoing wavefields have moved downwards. Furthermore, the influence of applying the local angular filter, which suppresses waves traveling between -25 and $+25$ degrees with respect to the horizontal axis, is shown. This removes the inverse extrapolated remnants of the direct wavefield and in addition suppresses that part of the wavefield that

would image with relatively low resolution. Also, as was shown above, the macro model is less correct for waves traveling along near-horizontal directions. The forward extrapolated source wavefields are separated with the same separation operators. This is not shown here.

In the deconvolution step, the actual source signature is needed. Since the goal is to obtain a structural image, a short wavelet is desirable. Furthermore, the wavelet must be zero-phase to successfully stack the migrated shot records after migration, which enhances the signal to noise ratio. In the data it can be observed that the reflection events already have a compact appearance; no significant ringing effects are present. It has been tried to estimate a wavelet for each shot record and to deconvolve the scattered data with this wavelet to obtain zero-phase reflection events. But, because of the stretching effect of wavelet deconvolution, this approach has been discarded. It is decided not to disturb the wavelet in the data. This means that a source wavelet is used that has unit amplitude within the frequency band of interest. To approximate a zero phase wavelet, a simple time shift is applied to the source wavelet, which is initially determined from the first break to the main peak of the wavelet present in the raw data. After migration, the timeshift is adjusted to achieve a better alignment of the major events over the migrated shot records, and then the migration is repeated. The timeshift is finally set to -1.5 ms on the average.

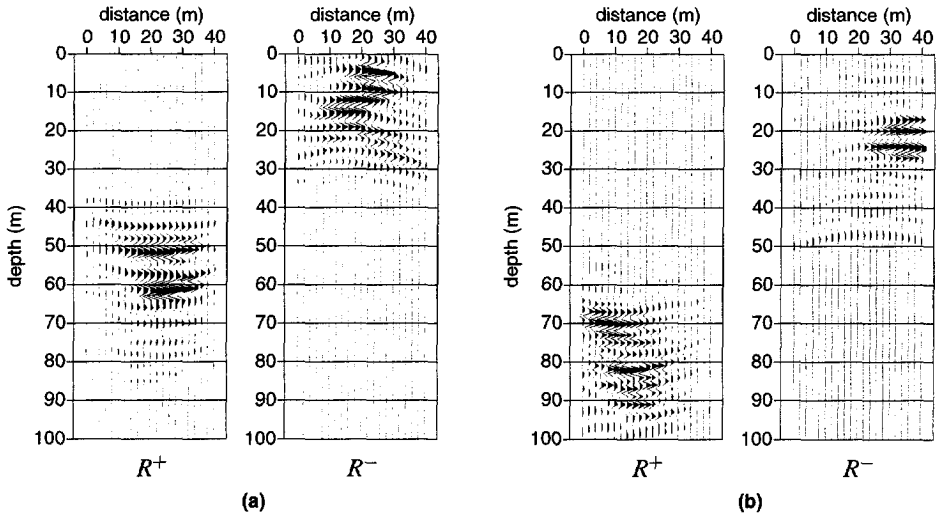


Fig. 5.8 Migration results for two shots. (a) shot at 30 m depth. (b) shot at 60 m depth.

First, the results for the two source positions at 30 and 60 m depth are presented. The original pre-processed data for these shots can be found in Figure 5.4. Figure 5.8.a shows the two images corresponding to R^+ and R^- for the shot at 30 m depth and, similarly, Figure 5.8.b shows the results for the shot at 60 m depth. Some horizontally oriented structures have partly been resolved. In (a), some remaining direct wave energy is imaged in the R^- panel, between 20 and

30 m depth. Due to the constrained illumination angle, the images of the reflectors in (a) do not continue up to the receiver well, at the right. In the R^+ panel of (b), reflectivity is imaged well below the bottom of the source well (recall that the maximum source depth is 62 m, and the maximum receiver depth is 60 m). Furthermore, only the left side of reflectors can be resolved by this shot, because the maximum receiver depth is 60 m. In the R^- panel of (b), reflectivity is resolved around 20 m depth up to the receiver well. This is possible because the direct wave removal procedure aims at preserving reflected wavefields even if they are masked by the direct wavefield. The illumination of this reflector however decreases towards the middle and is zero at the left side. There is no illumination in the shallowest part at all. In addition, angle dependent reflection effects causing lateral amplitude variations are imaged.

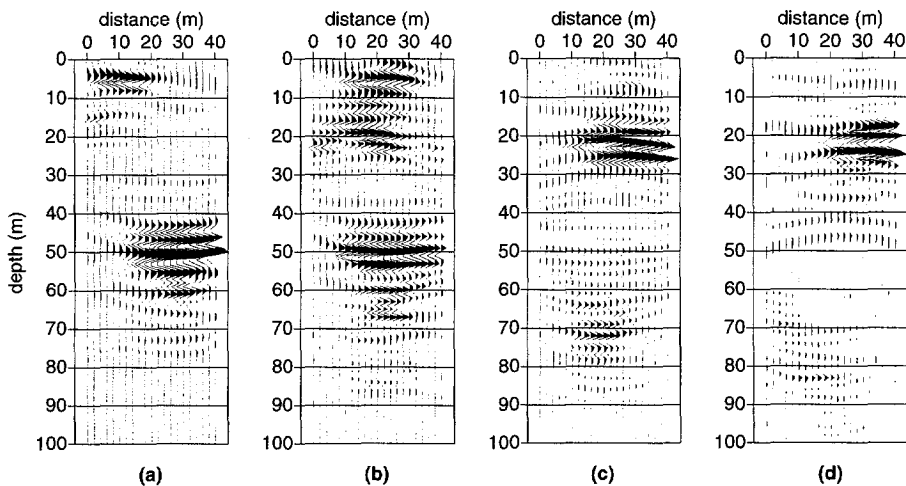


Fig. 5.9 Stacked migrated sections over partial shot range. Shot depth range: (a) 10-22 m. (b) 24-36 m. (c) 38-50 m. (d) 52-62 m. The amplitudes are clipped at 50% of the maximum amplitude over all stacks.

Assuming the macro velocity model to be correct, the migrated sections may be stacked over all shots, to increase the signal to noise ratio and to get one complete image of the interwell space. Due to the absence of imaged reflectivity between 30 and 45 m depth, there is no significant overlap between the stacked images of R^+ and R^- . Therefore, the polarity of the R^- stacked image is reverted, after which it may be added to that of R^+ .

First, four partial stacks are created, as displayed in Figure 5.9. Migrated shot records are stacked over 7 (a,b,c) or 6 (d) neighboring shot positions only. By inspecting the alignment of events over these partial stacks, the correctness of the macro velocity model can be verified. In this particular situation, it can be seen that the image around 20 m depth exhibits a phase change over (b), (c) and (d). Thus, if these partial stacks are added to compute a full stack, destructive

interference will occur, essentially decreasing the signal to noise ratio. The image of the event around 50 m depth does however line up over (a) and (b), while the macro velocity model has only one layer between 25 and 50 m depth. By inspecting single migrated shot records (not shown here) it is concluded that the velocity is correct, but edge effects in the inverse extrapolation of the strong reflection events around 20 m depth disturb the phase of the image near the receiver borehole. These can be suppressed by applying an extra taper on the shot records in the pre-processing step, by gradually tapering the start of the reflection events (see Appendix A). However, after applying this taper, the signal to noise ratio of the image near the receiver well is decreased.

The final stacked results can be found in Figure 5.10. Figure 5.10.a shows the plain stack over all shots, which is a stack over the partial stacks of Figure 5.9. Figure 5.10.b is an AGC enhanced version of (a), where an AGC window of 40 m has been used. Figure 5.10.c shows the results copied from Findlay et al. (1991), figure 5. The main imaged events are identified using the logs of the source and receiver well. Finally, Figure 5.10.d shows the stacked migrated section obtained with a different macro velocity model and after applying an extra taper to the start of all reflection events. The macro velocity model used in (d) is similar to that displayed to the side of (c), but without the shallow layer. Compared to (b), the lateral continuity of the image around 20 m depth is improved.

5.5 Discussion of the results

Comparing Figure 5.10.c with (b) and (d), it is clear that in (c) the imaged events are more uniform and are laterally more continuous. It is not known how the data in Findlay et al. (1991) have been pre-conditioned with respect to the varying amplitude over shots and hydrophones. However, Findlay et al. (1991) do mention that the traces of each shot record have been deconvolved with a minimum phase wavelet, which is estimated from the data. This may influence the phase of the imaged events, and, due to a different stacking, also the amplitudes in the final stacked section. In Findlay et al. (1991), a Kirchhoff type of migration algorithm has been used (Dillon (1990)). In each "diffraction point", amplitude values are summed over an aperture which includes dips of ± 22.5 degrees. In addition, before stacking, the amplitude in each diffraction point is divided by the number of rays that contribute to that point. This scaling normalizes the difference in illumination of the subsurface in the high frequency limit. It does however not completely compensate for the illumination edge effects described in section 3.4 (page 73). In conclusion, given the irregular amplitude distribution of the reflection events in the raw data, it is not known why the reflection events in 5.10.c all have about the same amplitude, both over depth and lateral position.

With respect to the position of the events, it seems that the velocities used in 5.10.b are to be preferred to those in (c) and (d). In the latter, the upper two coal seams are imaged too low, and the worked coal seam is imaged too high. The image around 5 m depth is due to the waterbottom.

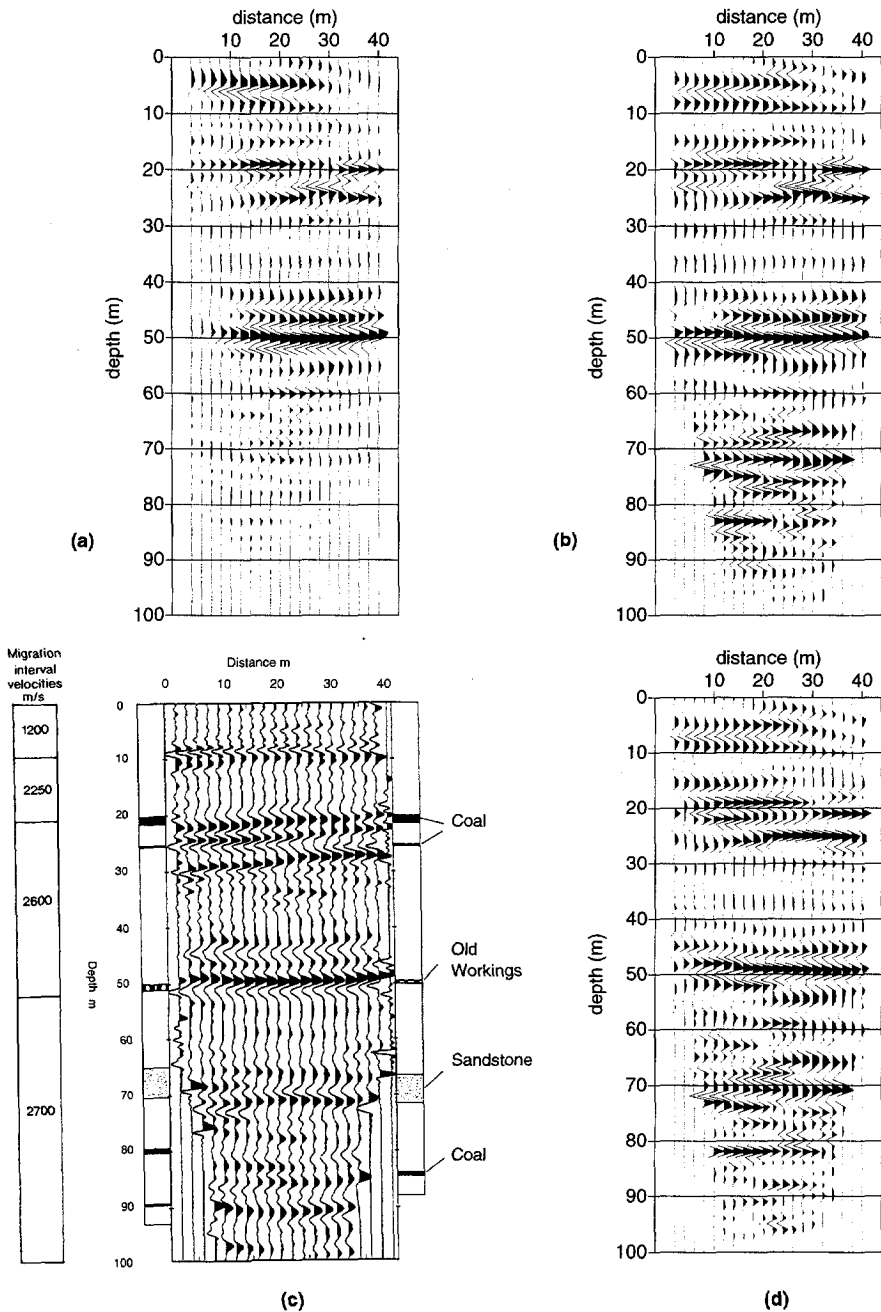


Fig. 5.10 Stacked migration results. (a) Plain stack. (b) Same as (a), but with AGC applied. (c) Result obtained by Findlay et al. (1991) (figure copied from this paper). (d) Results with layer velocities as indicated to the side of (c) (see text).

Taking an extra layer with a velocity of 1200 m/s into account, as was done in (c), did not yield satisfactory results, because of mis-alignment over the different migrated shot records. Note that this layer is located higher than the source and receiver apertures and thus its velocity can not be estimated by direct-wave travelt ime inversion. Similarly, it has been observed that the macro velocity model beneath the sources and receivers (> 62 m depth) may not be correct. In the R^+ image of Figure 5.8.a and 5.8.b, some deeper structures are imaged. In other migrated sections with shots fired beneath the worked coal seam (shot depth > 50 m), similar indications are present (not shown here). They do however not all line up correctly, which may indicate an incorrect velocity in that area. Especially the event at 60 m depth in 5.8.a is relatively strong, but almost absent in all four stacked sections in Figure 5.10. Furthermore, it is suspected that a small fault is present beneath a depth of 70 m. In interpreting the deeper part, it must however be realized that the signal to noise ratio is relatively low.

Summarized, for real data, the final migrated results largely depend on how the data is pre-processed, and what kind of normalizations are carried out after imaging. At this point, the lateral continuity of laterally continuous reflectors, which is important for structural interpretation, is not sufficient yet. The position of the events in 5.10.b is believed to be slightly better than in Findlay et al. (1991). The overall achieved spatial resolution is comparable, and lies in the order of 1-2 meters.

Appendix A

Pre-processing of crosswell data

The pre-processing step aims at processing the raw data in such a way that the subsequent macro velocity model and migration steps will yield the best results. This means that all effects present in the data which are not properly accounted for in later steps are considered to be noise, and must be suppressed. In addition, the data must be in the appropriate form for the later steps; for example traveltime information which is used by the traveltime inversion algorithm must be extracted.

A.1 Sources of noise

The following sources of noise (with the definition of “noise” as given above) can be identified:

1. Noise in the electronics of the acquisition system.

This is the background noise which ultimately limits the signal to noise ratio. Outside the frequency band of interest, this noise can be removed by filtering in the frequency domain. Because of the high quality of the currently available instrumentation for seismic data acquisition, this source of noise is negligible compared to other sources of noise.

2. Borehole related effects.

In the processing steps it is assumed that sources are point sources, receivers are point receivers, and there are no boreholes. Hence, deviations from this ideal situation are considered to be noise. Actually, the sources and receivers may have varying characteristics over different experiments. The main cause of irregular behavior is attributed to the coupling of sources and receivers to the borehole walls. The coupling influences the amplitude and directivity behavior and, for the source, it influences the kinds of elastic waves that are emitted into the subsurface. In the migration step it is assumed that the coupling is the same for all shots and receivers. A correction for this effect is outlined in section A.2.1, below. In addition to coupling effects, in a fluid filled borehole it is likely that the source generates tube waves which bounce up and down in the borehole. In regions where the wave propagation velocity of the surrounding medium

is less than the tube-wave propagation velocity, the tube-wave will radiate waves into the sub-surface, away from the actual source position. Similarly, in the receiver borehole tube waves may be generated by waves that arrive at the receiver borehole. Especially tube waves in the receiver borehole are an important source of noise. These may be suppressed by using f-k and median filtering techniques. Another source of borehole related noise is the incorrect positioning of sources and receiver in the borehole. A related issue is the deviation of the boreholes from the vertical axis, while in the processing vertical boreholes are assumed.

3. Wave propagation related effects.

The migration scheme uses a scalar, isotropic lossless representation of the wavefield and aims at imaging primary reflected energy. In reality, wave propagation may be fully elastic, anisotropic and effects such as multiple scattering and attenuation may be present. The primary crosswell (reflected) pressure waves (P) and shear waves (S) generally arrive at different times. In that case, separation in the time domain is possible, and the primary P and S waves may again be handled as separate scalar wavefields. Note that when using this approach, mode converted waves are not treated correctly. Other wave modes that may exist are guided waves, interface waves, headwaves and P-S converted waves. For the determination of first arrival traveltimes, the existence of head waves is especially important, since they may arrive before the arrival of the primary P wave. In the migration step, only the scattered and reflected energy is imaged, which means that the direct wave field must be removed first. This actually is the main pre-processing step, which is found in all crosswell wavefield imaging schemes. The approach taken in this thesis is sketched in section A.2.3, below.

A.2 Approach taken in this thesis

The general flow of the pre-processing approach taken in this thesis is depicted in Figure A.1. The first step is optional, and involves the separation of the elastic wavefield into P and S waves. In this thesis, only P waves are used for further processing. Next, the effect of irregular source and receiver coupling is corrected by energy balancing, and the first break of the direct wave is picked. These picks are used in the next step, which is the removal of the direct wave. Subsequently, tube waves are suppressed by filtering in the spatial frequency domain. The last step, which is optional, involves a deconvolution with the source signature, in order to sharpen the wavelet present in the scattered wavefield. At the right of Figure A.1, the removal of the direct wave is shown in more detail. In the following, the most important steps will be further discussed.

A.2.1 Energy balancing

To correct for the variation of energy emitted by sources and detected by receivers, one could just normalize all traces of the dataset by scaling with the maximum found in each trace. In practice,

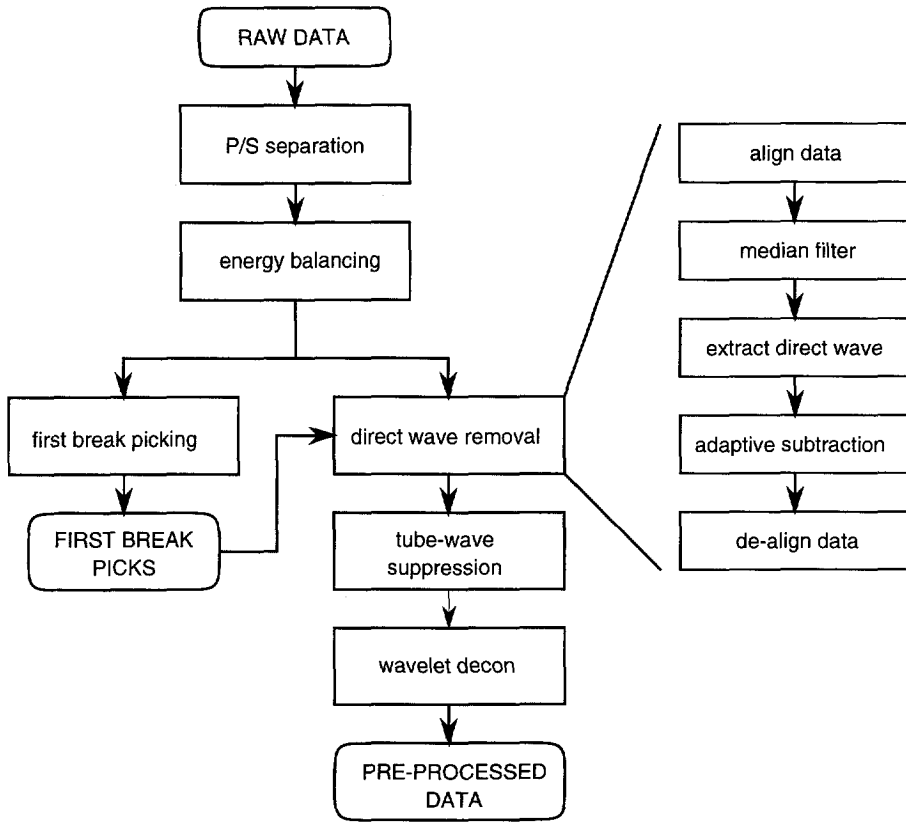


Fig. A.1 Flow diagram of the pre-processing step

this approach blows up noisy traces, and destroys all amplitude information. Therefore, a more subtle approach is proposed.

The assumption is made that if all sources are fired simultaneously, the direct wave as received by the detectors will have a constant energy content over all traces. This is exactly true in a homogeneous medium, and a reasonable assumption in a (near) horizontally layered medium with moderate contrasts. Similarly, if we stacked the data over all detectors for each source, a constant energy over all stacked source traces is expected. The energy in the stacked traces is then used to normalize the individual common source and common receiver gathers. This procedure may be applied in an iterative fashion. For an example, see section 5.2, Figure 5.2 on page 97.

A.2.2 The picking problem

For the macro model estimation step and the direct wave removal step, picks are needed on the traveltimes of the direct wave. In general, the picking (tracking) of events in seismic sections can be a difficult task. Fortunately, crosswell first arrivals are easier to pick than later arriving events which, for complex subsurface geometries, may be obscured by other events. There are several approaches that start with reordering the data into a different domain. In this thesis, no such reordering is done, because of the high quality of first arrival events in both the synthetic data and the field data sets that are used. Instead, a fully automated picking routine has been developed, that detects the first break by determining when the amplitude exceeds a certain threshold. Then, the beginning of the event is searched by looking backwards. No inter-trace information is used at this point. To remove outliers, a 1D alpha-trimmed median filter is used which is applied along the trace direction. This approach proved to be successful for all the data processed in this thesis.

A.2.3 Direct wave removal

The direct wave removal approach aims at preserving the reflected wavefield even if it is obscured by the direct wave. This is especially important for the illumination of the subsurface near the receiver borehole.

At the right of Figure A.1, the steps used in removing the direct wavefield are shown in more detail. First, the data are aligned in the frequency domain using the first arrival picks. Then, a 1D median filter is applied along the spatial direction (i.e. depth), which preserves the aligned events but suppresses the underlying reflected wave events. Then, using an estimate on the signal length of the direct wave, the direct wave is extracted from the aligned data by tapering. Using adaptive subtraction techniques, the tapered direct wave is then subtracted from the original aligned data. Note that in this way that part of the original data which is not obscured by the direct wave is *not* affected. Finally, the data is de-aligned, again using the first break picks.

Appendix B

The common focus point concept

In this Appendix, the concept of crosswell Common Focus Point (CFP) illumination and migration is briefly discussed. This concept follows from looking at the migration process as a *double focussing* operation. Common focus point processing is an emerging technique that provides a new view at the estimation of macro velocity models and the true-amplitude migration of seismic data (see Berkhout (1995)). The CFP approach improves the understanding of crosswell inversion and has the potential to estimate and correct for amplitude errors due to poor illumination. In this Appendix we will show the way in which crosswell migration can be seen as a double focussing procedure. Examples are presented to illustrate the concept.

B.1 Crosswell migration by double focussing

Figure B.1 shows a model consisting of two horizontal reflectors. Sources are placed in the left borehole at $x = x_0$ and detectors in the right borehole at $x = x_M$. The rays drawn from the sources to the focus point at $(x, z) = (x_m, z_n)$ show a focussing of energy in the focus point. Next, the energy is either transmitted or reflected and travels towards the detector borehole where it is detected. In this Appendix only *reflection* at an interface will be considered. This means that it is assumed that the transmission effects have already been eliminated in a pre-processing step. Furthermore, only reflections corresponding to R^+ are considered.

In this section, a different approach to migration is presented by making use of focussing areal arrays at both the source and detector side. Recall that migration consists of the removal of propagation effects from sources to reflection points and from reflection points to the detectors, followed by an imaging step. Using the concept of common focus points, the incident wavefield in each subsurface point is computed by synthetically focussing point sources in each point $(x, z) = (x_m, z_n)$, using the sources at $x = x_0$ according to

$$\mathbf{P}_i^+(x_m) = \mathbf{W}_h^+(x_m, x_0) \mathbf{S}_0^+(x_0) \mathbf{\Gamma}_n^+(x_0), \quad (\text{B.1})$$

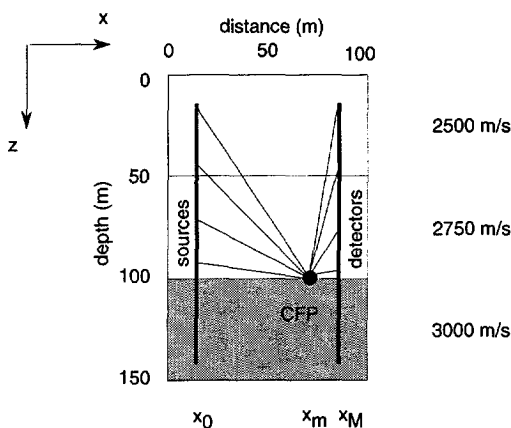


Fig. B.1 Model used in this Appendix to illustrate the concept of crosswell common focus point analysis. The model contains two reflectors, at 50 m and 100 m depth respectively. Sources are placed in the borehole at the left, detectors are placed in the borehole at the right. A focus point at $(x_m, z_n) = (75, 100)$ m is indicated.

where \mathbf{S}_0^+ is the pre-stack source matrix, which for unit point sources is a unity matrix, $\Gamma_n^+(x_0)$ is a so-called *synthesis operator*, $\mathbf{W}_h^+(x_m, x_0)$ describes the downward propagation between x_0 and x_m , and $\mathbf{P}_i^+(x_m)$ is the downgoing incident wavefield at the vertical cross-section $x = x_m$ (see also equation (3.44) at page 57). The synthesis operator is constructed from

$$\mathbf{I}_n^+(x_m) = \mathbf{W}_h^+(x_m, x_0) \mathbf{S}_0^+(x_0) \Gamma_n^+(x_0), \quad (\text{B.2})$$

in such a way that vector $\mathbf{I}_n^+(x_m) = (0, 0, \dots, 0, 1, 0, \dots, 0, 0)^T$, with a unit element at the depth of the focus point $z = z_n$. When only unit sources are used, we have

$$\mathbf{I}_n^+(x_m) = \mathbf{W}_h^+(x_m, x_0) \Gamma_n^+(x_0). \quad (\text{B.3})$$

The synthesis operator $\Gamma_n^+(x_0)$ is computed by taking the n th column of the inverse of $\mathbf{W}_h^+(x_m, x_0)$:

$$\Gamma_n^+(x_0) = [\mathbf{W}_h^+(x_m, x_0)]^{-1} \mathbf{I}_n^+(x_m). \quad (\text{B.4})$$

The synthesized *areal* source wavefield $\mathbf{S}_0^+(x_0) \Gamma_n^+(x_0)$ now optimally illuminates the subsurface at the focus point.

Recall that for one cross-section $x = x_m$ the forward representation for seismic crosswell reflection data is written as

$$\mathbf{P}_s^-(x_M) = \mathbf{W}_h^-(x_M, x_m) \mathbf{R}^+(x_m) \mathbf{W}_h^+(x_m, x_0) \mathbf{S}_0^+(x_0), \quad (\text{B.5})$$

which is the full pre-stack data matrix version of equation (3.46) for one cross-section x_m . Now, taking unit sources and using the focussed source wavefield, we can write

$$\underline{\mathbf{P}}_s^-(x_M)\underline{\mathbf{\Gamma}}_n^+(x_0) = \underline{\mathbf{W}}^-(x_M, x_m)\underline{\mathbf{R}}^+(x_m)\underline{\mathbf{I}}_n^+(x_m). \quad (\text{B.6})$$

For zero-offset reflectivity information only and with a reflector at $z = z_n$, this reduces to

$$\underline{\mathbf{P}}_s^-(x_M, z_n) = \underline{\mathbf{W}}^-(x_M, x_m)[\underline{\mathbf{R}}_n^+(x_m, z_n)\underline{\mathbf{I}}_n^+(x_m)], \quad (\text{B.7})$$

where $\underline{\mathbf{P}}_s^-(x_M, z_n) = \underline{\mathbf{P}}_s^-(x_M)\underline{\mathbf{\Gamma}}_n^+(x_0)$; $\underline{\mathbf{R}}_n^+(x_m, z_n)$ is the scalar reflection coefficient in the focus point. Vector $\underline{\mathbf{P}}_s^-(x_M, z_n)$ is called a *CFP gather*. The CFP gather can be seen as the response of a source placed in the focus point $(x, z) = (x_m, z_n)$, with a source strength proportional to the zero-offset reflectivity, measured at the vertical detector borehole $x = x_M$. Thus, the CFP gather only contains propagation effects from the focus point to the detector array; the propagation effects from the source array to the focus point have been removed.

Similarly, the wavefield can be focussed in detection such that the response from the focus point is optimally detected, by using an *areal* detector array. For unit detectors, we can write

$$\underline{\mathbf{I}}_n^-(x_m) = \underline{\mathbf{\Gamma}}_n^-(x_M)\underline{\mathbf{W}}^-(x_M, x_m), \quad (\text{B.8})$$

where row vector $\underline{\mathbf{I}}_n^-(x_m) = (0, 0, \dots, 0, 1, 0, \dots, 0, 0)$ has a unit element at the depth of the focus point $z = z_n$. The synthesis operator at the detector side $\underline{\mathbf{\Gamma}}_n^-(x_M)$, which is a row vector, equals the n th row of the inverse of matrix $\underline{\mathbf{W}}^-(x_M, x_m)$:

$$\underline{\mathbf{\Gamma}}_n^-(x_M) = \underline{\mathbf{I}}_n^-(x_m)[\underline{\mathbf{W}}_h^-(x_M, x_m)]^{-1}. \quad (\text{B.9})$$

Using the focussing at the detector side in equation (B.6), the double focussing procedure is obtained as:

$$\underline{\mathbf{\Gamma}}_n^-(x_M)\underline{\mathbf{P}}_s^-(x_M)\underline{\mathbf{\Gamma}}_n^+(x_0) = \underline{\mathbf{I}}_n^-(x_m)\underline{\mathbf{R}}^+(x_m)\underline{\mathbf{I}}_n^+(x_m), \quad (\text{B.10})$$

or, for zero offset reflectivity and a reflector at $z = z_n$ only:

$$\underline{\mathbf{\Gamma}}_n^-(x_M)\underline{\mathbf{P}}_s^-(x_M)\underline{\mathbf{\Gamma}}_n^+(x_0) = \underline{\mathbf{R}}^+(x_m, z_n). \quad (\text{B.11})$$

Thus, we have arrived at an expression in which application of double focussing, at both the source and detector side, results in the estimation of the reflectivity in the focus point. Expressions for $\underline{\mathbf{R}}^-(x_m, z_n)$ can be derived in an analogous manner. The procedure will now be illustrated using synthetic data.

B.2 Examples

Figure B.2 shows the raw and pre-processed shot records for three shot positions, obtained by using the model of Figure B.1. In the top row, the full data is shown, while at the bottom the pre-processed data is visualized. For the CFP examples, 64 shots have been used.

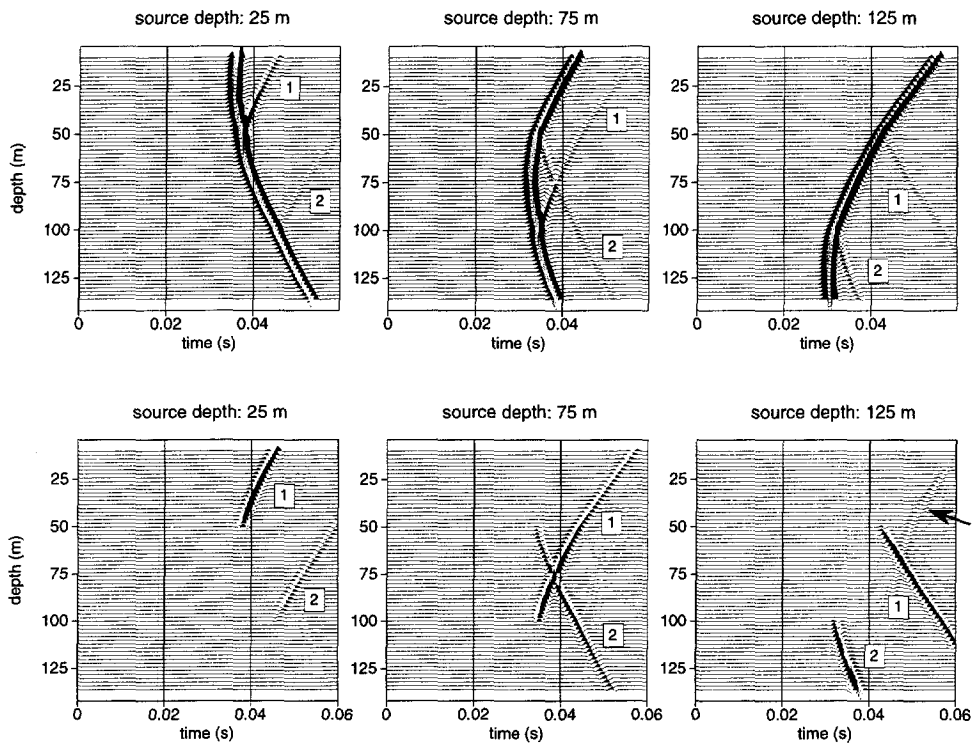


Fig. B.2 Selected shot records for three different source depths. Top row: raw shot records. Bottom row: pre-processed shot records. The (1) indicates reflections from the top reflector, the (2) indicates reflections from the bottom reflector. The data is generated using finite-difference techniques. Some weak artificial reflections from the boundary of the model are visible, as indicated by the arrow.

Figure B.3 shows the application of the focussing operator on the source array. The synthesized source wavefield is forward-extrapolated in time. Three snapshots are shown, for three different time-steps. At the top, all sources have been used. In the middle row, only the sources above the reflector at 100 m depth have been used. This source wavefield effectively illuminates the reflector at 100 m from the top. When applied to the data, a CFP gather is constructed which only contains reflected energy from the top of the reflector (R^+). At the bottom, only the sources below 100 m depth have been used. A CFP gather constructed with this operator will only contain reflected energy emerging from the bottom of the layer (R^-).

Finally, in Figure B.4 the results are shown of the application of the focussing operators at both

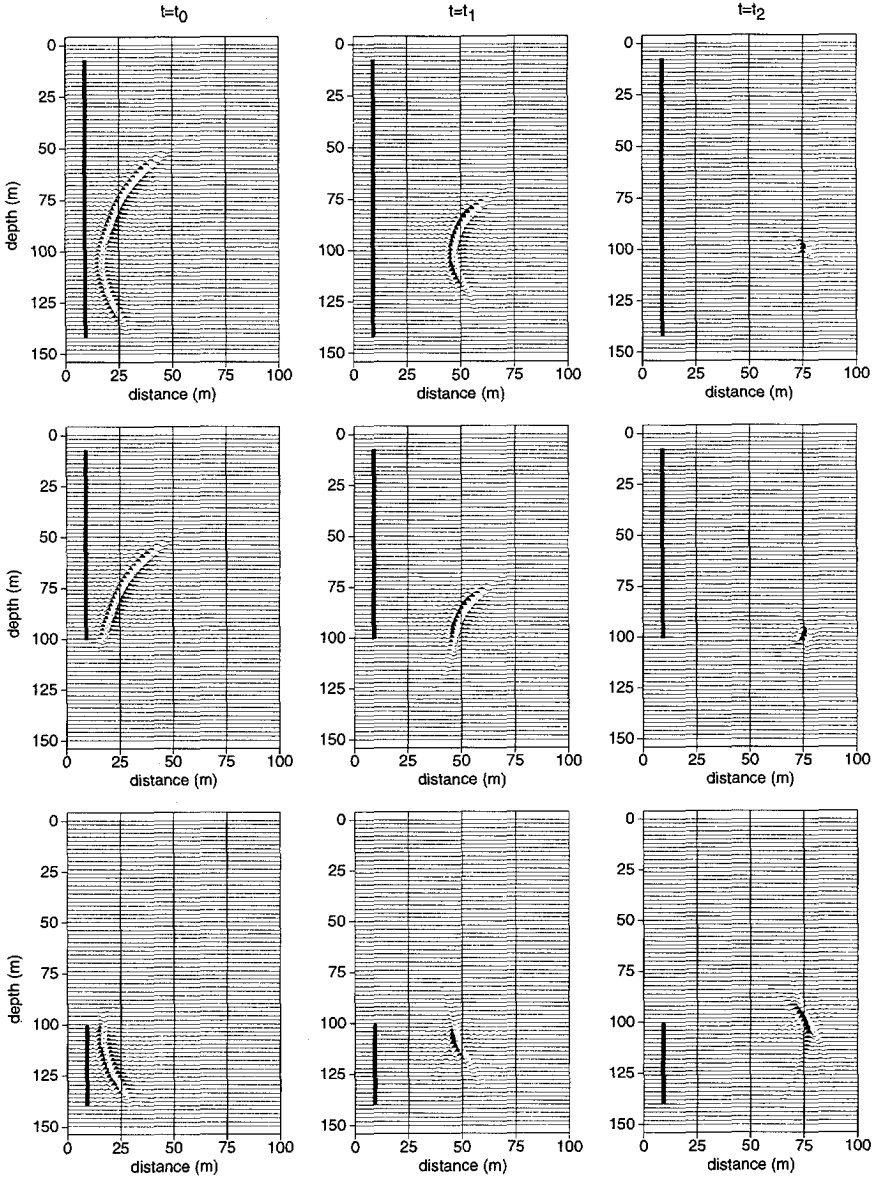


Fig. B.3 Snapshots showing the focussing of the synthesis operator at the source side. The synthesis operator is designed to focus in the focus point as indicated in Figure B.1. From left to right, three snapshots are shown for increasing time steps, which corresponds to forward extrapolation of the synthesis operator. In the top row, all shots are used; in the middle row only the shots up to 100 m depth are used; in the bottom row only the shots deeper than 100 m are used.

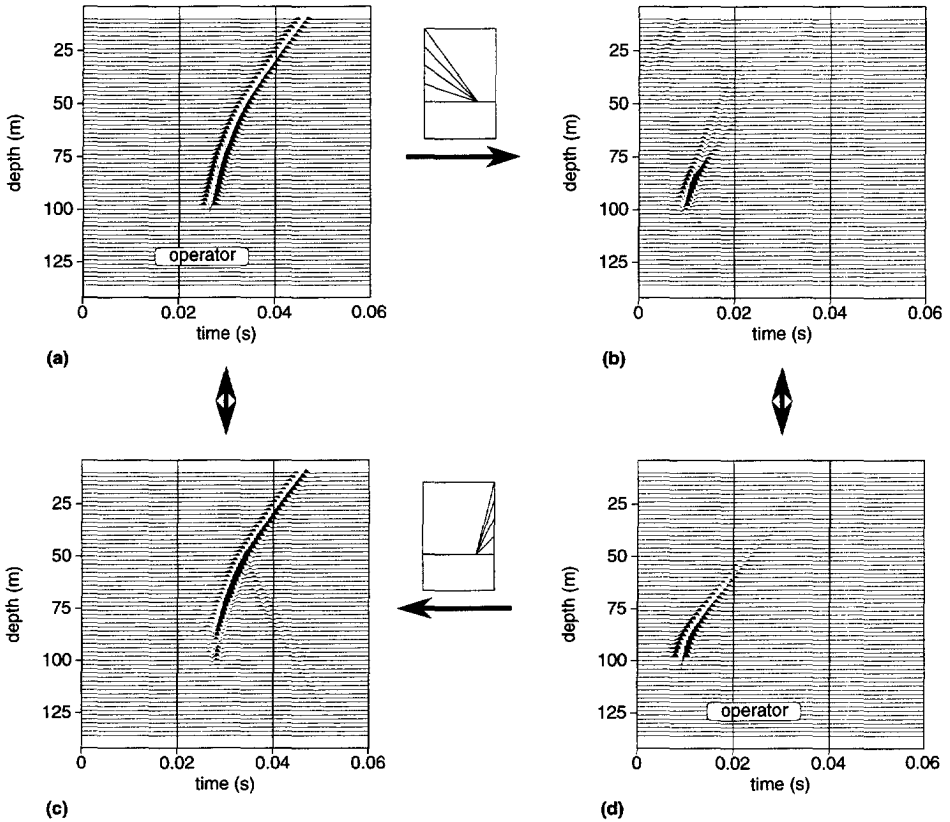


Fig. B.4 Focussing of the data in a common focus point using synthesis at the source side and at the detector side. (a) Focussing operator at the source side. (d) Focussing operator at the detector side. (b) Synthesized data after application of (a). (c) Synthesized data after application of (d).

the source and detector side of the pre-processed data. In the focussing operator at the source side, displayed in Figure B.4.a, only the sources down to 100 m are used. This corresponds to the snapshots shown in the middle row of Figure B.3. Similarly, in the focussing operator at the detector side, as displayed in Figure B.4.d, only the detectors down to 100 m are used. Figure B.4.b shows the application of the synthesis operator at the source side (a) to the data. The synthesized data (b) only contains propagation effects from the focus point at (75,100) m to the detectors. Figure B.4.c shows the application of the synthesis operator at the detector side

(d) to the data. Now, the synthesized response (c) only contains propagation effects from the source array to the focus point. Also, a multiple reflection from the top reflector is visible.

Next, the reflectivity in the focus point can be computed along two ways, yielding the same result. First, the operator in (a) may be used to deconvolve the data in (c) on a trace-by-trace basis, and then the resulting traces are stacked. Similarly, the operator in (d) may be used to deconvolve (b), after which the resulting traces are stacked. The stacked trace yields the band-limited reflectivity around the focus point.

B.3 Concluding remarks

From Figure B.4 it can be observed that (a) resembles (c), and (b) resembles (d). Actually, if the macro velocity model is correct, the traveltime curves of the corresponding responses must be the same. Thus, the CFP technique provides a measure for the correctness of the macro velocity model, and may be used to update the model.

The most important aspect of the CFP technique with respect to crosswell migration is the double-focussing procedure. CFP migration actually is pre-stack migration carried out on a point-by-point basis. This means that we have full control over both the illumination of the subsurface and the characteristics of the detection process, in every individual subsurface point. A current problem of the shot record migration approach presented in this thesis is that due to irregular illumination of the subsurface, which is unavoidable for crosswell acquisition geometries, a final stacked migrated section exhibits large artificial (lateral) amplitude variations. By using the energy contained in the illuminating and detecting focussed beams, it is possible to normalize the sections in a consistent way before stacking them. This will improve the lateral continuity of stacked crosswell seismic sections, without complying to ad-hoc normalization methods such as AGC.

Bibliography

- Bayes, T. (1763). Essay towards solving a problem in the doctrine of chances, *republished in Biometrika*, 1958 **45**: 293–315.
- Berkhout, A. J. (1982). *Seismic migration*, Elsevier Science Pub. Co., Inc.
- Berkhout, A. J. (1984a). Multidimensional linearized inversion and seismic migration, *Geophysics* **49**(11): 1881–1895.
- Berkhout, A. J. (1984b). *Seismic resolution*, Geophysical press.
- Berkhout, A. J. (1987). *Applied seismic wave theory*, Elsevier Science Pub. Co., Inc.
- Berkhout, A. J. (1995). Pushing the limits of seismic imaging, part 2: Prestack migration in terms of double dynamic focusing, *will appear in Geophysics*.
- Berkhout, A. J. and Van Wulfften Palthe, D. W. (1979). Migration in terms of spatial deconvolution, *Geophysical Prospecting* **27**: 261–291.
- Berryman, J. G. (1990). Stable iterative reconstruction algorithm for nonlinear travelt ime tomography, *Inverse Problems* **6**: 21–42.
- Beylkin, G. (1985). Imaging of discontinuities in the inverse scattering problem by inversion of a causal generalized radon transform, *J. Math. Phys.* **26**: 99–108.
- Bishop, T. N., Bube, K. P., Cutler, R. T., Langan, R. T., Love, P. L., Resnick, J., Shuey, R., Spindler, D. and Wyld, H. (1985). Tomographic determination of velocity and depth in laterally varying media, *Geophysics* **50**: 903–923.
- Blacquièrè, G. (1989). *3D wave field extrapolation in seismic depth migration*, PhD thesis, Delft University of Technology, the Netherlands.
- Bleistein, N. (1987). On the imaging of reflectors in the earth, *Geophysics* **52**(7): 931–942.
- Bois, P., La Porte, M., Lavergne, M. and Thomas, G. (1972). Well-to-well seismic measurements, *Geophysics* **37**(3): 471–480.
- Bregman, N. D., Bailey, R. C., and Chapman, C. H. (1989a). Crosshole seismic tomography, *Geophysics* **54**: 200–215.
- Bregman, N. D., Hurley, P. A. and West, G. F. (1989b). Seismic tomography at a fire-flood site, *Geophysics* **54**(9): 1082–1090.
- Brzostowski, M. A. and McMechan, G. A. (1991). 4-d Tomographic monitoring of enhanced oil recovery, *61st Annual Internat. Mtg., Soc. Expl. Geophys., Expanded Abstracts*, 367–370.

- Carrion, P., Costa, J., Pinheiro, J. E. F. and Schoenberg, M. (1992). Cross-borehole in anisotropic media (short note), *Geophysics* **57**(9): 1194–1198.
- Chen, S.-T. and Miller, M. (1994). Single-well profiling tool with a variable downhole source/receiver spacer, *64th Annual Internat. Mtg., Soc. Expl. Geophys., Expanded Abstracts*, DP3.6.
- Chiu, S. K. L. and Stewart, R. R. (1987). Tomographic determination of three-dimensional seismic velocity structure using well logs, vertical seismic profiles, and surface seismic data, *Geophysics* **52**: 1085–1098.
- Claerbout, J. (1971). Towards a unified theory of reflector mapping, *Geophysics* **36**(3): 476–481.
- Corones, J. (1975). Bremmer series that correct parabolic approximations, *J. Math. Analysis and Applications* **50**: 361–372.
- Cotten, S. A. and Geldmacher, I. M. (1990). Cross-hole tomography and in-seam seismic techniques to locate an abandoned coal mine, *60th Annual Internat. Mtg., Soc. Expl. Geophys., Expanded Abstracts*, 737–739.
- Crampin, S. (1984). Anisotropy in exploration seismics, *First Break* **2**(3): 19–21.
- De Bruin, C. (1992). *Linear AVO inversion by prestack depth migration: Imaging angle dependent reflectivity as a tool for litho-stratigraphic inversion*, PhD thesis, Delft University of Technology, the Netherlands.
- De Hoop, M. (1992). *Near-surface seismic imaging*, PhD thesis, Delft University of Technology, the Netherlands.
- Devaney, A. J. (1982). A filtered backpropagation algorithm for diffraction tomography, *Ultrasonic Imaging* **4**: 336–350.
- Devaney, A. J. (1984). Geophysical diffraction tomography, *IEEE Trans. on Geoscience and Remote Sensing* **22**(1): 3–13.
- Dillon, P. (1990). A comparison between Kirchhoff and GRT migration on VSP data, *Geophysical Prospecting* **38**: 757–777.
- Dines, K. and Lytle, R. (1979). Computerised geophysical tomography, *Proc. IEEE* **76**: 1065–1073.
- Duijndam, A. J. W. (1988a). Bayesian estimation in seismic inversion part I - principles, *Geophys. Prosp.* **36**(8): 878–898.
- Duijndam, A. J. W. (1988b). Bayesian estimation in seismic inversion part II - uncertainty analysis, *Geophys. Prosp.* **36**(8): 899–918.
- Findlay, M. J., Gouly, N. R. and Kragh, J. E. (1991). The crosshole seismic reflection method in opencast coal exploration, *First Break* **9**(11): 509–514.
- Friedel, M. J., Tweeton, D. R., Jackson, M. J., Jessop, J. A., Cumerlato, C. L. and Billington, S. (1992). Mining applications of seismic tomography, *62nd Annual Internat. Mtg., Soc. Expl. Geophys., Expanded Abstracts*, 58–62.
- Geyer, R. L. (1993). Spindletop cross-borehole survey, 1961, *The Leading Edge* **12**(1): 26–31.
- Giling, E. J. M., P. P. van 't, V., Vos, H. C. L. and Berkhout, A. J. (1992). Model-driven cross-well travel-time tomography, *62nd Annual Internat. Mtg., Soc. Expl. Geophys., Expanded Abstracts*, 737–740.
- Gill, P. E., Murray, W. and Wright, M. H. (1981). *Practical Optimization*, Academic Press, London.

- Gouly, N. (1993). Controlled-source tomography for mining and engineering applications, in H. Iyer and K. Hirahara (eds), *Seismic Tomography*, Chapman & Hall, 797–813.
- Gray, S. and Lines, L. (1992). Cross-borehole tomographic migration, *Jrnl. Seism. Expl.* **1**: 315–324.
- Guiziou, J. and Haas, A. (1988). Three-dimensional travelt ime inversion in anisotropic media, *58th Annual Internat. Mtg., Soc. Expl. Geophys., Expanded Abstracts*, 1089–1091.
- Hardage, B. (1992). *Crosswell seismology & reverse VSP*, Geophysical Press.
- Harris, J. M. (1987). Diffraction tomography with arrays of discrete sources and receivers, *IEEE Trans. on Geoscience and Remote Sensing* **25**: 448–455.
- Harris, J. M., Dahlhaus, L. and Michelena, R. (1994). P-wave anisotropy in shales from crosswell data, *64th Annual Internat. Mtg., Soc. Expl. Geophys., Expanded Abstracts*, 1125–1128.
- Harris, J. M., Nolen-Hoeksema, R., Rector III, J. W., van Schaack, M. and Lazaratos, S. K. (1992). High resolution cross-well imaging of a est texas carbonate reservoir: part 1. data acquisition and project overview, *62nd Annual Internat. Mtg., Soc. Expl. Geophys., Expanded Abstracts*, 53.
- Harris, J. M., Tan, H., Lines, L., Pearson, C., Treitel, S., Marko, G., Moos, D. and Hoeksma, R. N. (1990). Cross-well tomographic imaging of geological structures in gulf coast sediments, *60th Annual Internat. Mtg., Soc. Expl. Geophys., Expanded Abstracts*, 37–40.
- Hawkins, L. V., Whiteley, R. J., Holmes, W. H. and Dowle, R. (1982). Downhole-crosshole high resolution seismic reflection profiling to resolve detailed coal seam structure, *52nd Annual Internat. Mtg., Soc. Expl. Geophys., Expanded Abstracts*.
- Hu, L., McMechan, G. A. and Harris, J. M. (1988). Acoustic prestack migration of cross-hole data, *Geophysics* **53**: 1015–1023.
- Ivansson, S. (1986). Seismic borehole tomography - theory and computational methods, *Proc. IEEE* **74**(2): 328–338.
- Jung, Y., Ibrahim, A. and Borns, D. (1991). Mapping fracture zones in salt: High-resolution, cross-gallery seismic tomography, *The Leading Edge* **10**(4): 37–39.
- Justice, J. H., e. a. (1989). Acoustic tomography for monitoring enhanced oil recovery, *The Leading Edge* **8**(2): 12–19.
- Justice, J. H., Mathisen, M. E., Vassiliou, A. A. and Shiao, I. (1992). Crosshole seismic tomography - recent case histories, *62nd Annual Internat. Mtg., Soc. Expl. Geophys., Expanded Abstracts*, 67–69.
- Justice, J. H., Mathisen, M. E., Vassiliou, A. A., Shiao, I., Alameddine, B. R. and Guinzy, N. J. (1993). Crosswell seismic tomography in improved oil recovery, *First Break* **11**(6): 229–239.
- Kak, A. (1979). Computerized tomography with x-ray, emission, and ultrasound sources, *Proc. IEEE* **67**: 1245–1272.
- Kelly, K. R., Ward, R. W., Treitel, S. and Alford, R. M. (1976). Synthetic seismograms - a finite-difference approach, *Geophysics* **41**(1): 2–27.
- Krohn, C. (1992). Cross-well continuity logging using guided seismic waves, *The Leading Edge* **11**(7): 39–45.
- Lazaratos, S. K., Langan, R., Harris, J. M. and Marion, B. P. (1994). Shear-wave crosswell reflection imaging in West Texas, *64th Annual Internat. Mtg., Soc. Expl. Geophys., Expanded Abstracts*, 289–293.

- Lazaratos, S. K., Rector III, J. W., Harris, J. M. and van Schaack, M. (1993). High-resolution, cross-well, reflection imaging: Potential and technical difficulties, *Geophysics* **58**(9): 1270–1280.
- Lindman, E. L. (1975). Free space boundaries for the scalar wave equation, *J. Comp. Phys.* **18**: 66–78.
- Lines, L. (1992). Poor man's anisotropic travelttime tomography, *62nd Annual Internat. Mtg., Soc. Expl. Geophys., Expanded Abstracts*, 83–86.
- Lines, L. R. and LaFehr, E. D. (1989). Tomographic modeling of a cross-borehole data set, *Geophysics* **54**: 1249–1257.
- Lines, L. R. and Tan, H. (1990). Cross-borehole analysis of velocity and density, *60th Annual Internat. Mtg., Soc. Expl. Geophys., Expanded Abstracts*, 34–36.
- Lo, T., Toksoz, M. N., Xu, S. and Wu, R. S. (1988). Ultrasonic laboratory tests of geophysical tomographic reconstruction, *Geophysics* **53**: 947–956.
- Lou, M. and Crampin, S. (1993). Modelling guided waves in cross-hole surveys in uncracked and cracked rock, *Geophys. Prosp.* **41**(3): 241–266.
- Michelena, R. J., Muir, F. and Harris, J. M. (1993). Anisotropic travelttime tomography, *Geophys. Prosp.* **41**(4): 381–412.
- Miller, D., Oristaglio, M. and Beylkin, G. (1987). A new slant on seismic imaging: Migration and integral geometry, *Geophysics* **52**: 943–964.
- Mufti, I. R. (1992). Tomographic seismic imaging of reservoirs in three dimensional environments, *62nd Annual Internat. Mtg., Soc. Expl. Geophys., Expanded Abstracts*, 79–82.
- NAG (1990). *The NAG Fortran Library Manual - Mark 12*, Numerical Algorithms Group, Oxford, United Kingdom.
- Nolet, G. (ed.) (1987). *Seismic tomography with applications in global seismology and exploration geophysics*, D. Reidel Publ. Co.
- Parra, J. O. and Bangs, J. H. (1992). High-resolution reverse VSP and interwell seismic experiments at the Buckhorn test site in Illinois, *62nd Annual Internat. Mtg., Soc. Expl. Geophys., Expanded Abstracts*, 103–107.
- Paulsson, B. N. P., Smith, M. E., Tucker, K. E. and Fairborn, J. W. (1992). Characterization of a steamed oil recovery using cross-well seismology, *The Leading Edge* **11**(7): 24–32.
- Phillips, W. S. and Fehler, M. C. (1991). Travelttime tomography: A comparison of popular methods, *Geophysics* **56**(10): 1639–1649.
- Pratt, R. G. and Goulty, N. R. (1991). Combining wave-equation imaging with travelttime tomography to form high-resolution images from crosshole data, *Geophysics* **58**: 208–224.
- Pratt, R. G., McLaughy, W. G. and Chapman, C. H. (1993). Anisotropic velocity tomography: A case study in a near-surface rock mass, *Geophysics* **58**(12): 1748–1763.
- Pratt, R. G., West, G. F., Hurley, P. A. and Zeng, X. (1992). Crosshole seismology in the Athabasca tar sands, *62nd Annual Internat. Mtg., Soc. Expl. Geophys., Expanded Abstracts*, 63–66.
- Pratt, R. G. and Worthington, M. H. (1988). The application of diffraction tomography to cross-hole seismic data, *Geophysics* **53**: 1284–1294.

- Rietveld, W. E. A. (1995). *Controlled illumination in prestack seismic migration*, PhD thesis, Delft University of Technology, the Netherlands.
- Rowbotham, P. and Gouly, N. R. (1994). Wavefield separation by 3-d filtering in crosshole seismic reflection processing, *Geophysics* **59**(7): 1065–1071.
- Scheffers, B. C. (1993). *Near-surface seismic imaging*, PhD thesis, Delft University of Technology, the Netherlands.
- Shannon, C. (1948). A mathematical theory of communication, *Bell System Technical Journal* **27**: 379–423 and 623–656.
- Shima, H. and Imamura, S. (1991). An application of high resolution resistivity tomography to a small oil reservoir: Field test at Buckhorn Test Facility at Illinois, *61st Annual Internat. Mtg., Soc. Expl. Geophys., Expanded Abstracts*, 391–394.
- Stewart, R. R. (1985). Median filtering: Review and a new f/k analogue design, *J. Can. Soc. Expl. Geophys.* **21**: 54–63.
- Stewart, R. R. (1991). *Course notes: Exploration seismic tomography*, Soc. Expl. Geophys.
- Tarantola, A. (1987). *Inverse problem theory; methods for data fitting and model parameter estimation*, Elsevier Science Pub. Co., Inc.
- Tura, M. A. C., Greaves, R. J. and Beydoun, W. B. (1994). Crosswell seismic reflection/diffraction tomography: A reservoir characterization application, *Geophysics* **59**(3): 351–361.
- Tura, M. A. C., Johnson, L. R., Majer, E. L. and Peterson, J. E. (1992). Application of diffraction tomography to fracture detection, *Geophysics* **57**(2): 245–257.
- Van der Made, P. M. (1988). *Determination of macro subsurface models by generalized inversion*, PhD thesis, Delft University of Technology, the Netherlands.
- Vassiliou, A. A., Savage, C. W., Liner, C. L., Bozkurt, G. and Lines, L. R. (1994a). Glenn pool project: Initial tomographic results, *64th Annual Internat. Mtg., Soc. Expl. Geophys., Expanded Abstracts*, 302.
- Vassiliou, A. A., Thomsen, L. A., Treitel, S., Queen, J. H. and Harlan, W. S. (1994b). Crosswell tomography in anisotropic media - case studies, *56th Mtg. Eur. Assoc. Expl. Geophys., Extended Abstracts*, Eur. Assoc. Expl. Geophys.
- Virieux, J. (1986). P-SV wave propagation in heterogeneous media - velocity-stress finite-difference method, *Geophysics* **51**(4): 889–901.
- Vos, H. C. L., Veen, P., Wal, L. and Berkhout, A. J. (1990). Spatial resolution in well-to-well seismic experiments, *52nd Mtg. Eur. Assoc. Expl. Geophys., Abstracts*, Eur. Assoc. Expl. Geophys.
- Wapenaar, C. P. A. (1993). Representation of seismic reflection data; part 1: state of affairs, *Jrnl. Seis. Expl.* **2**(3): 123–131.
- Wapenaar, C. P. A. (1995a). Inversion vs migration - a new perspective to an old discussion, *submitted to: Geophysics*.
- Wapenaar, C. P. A. (1995b). Representation of one-way wave fields, *submitted to the Geoph. J. Int.*
- Wapenaar, C. P. A. and Berkhout, A. J. (1989). *Elastic wave field extrapolation*, Elsevier Science Pub. Co., Inc.

- Williamson, P. R. (1991). A guide to the limits of resolution imposed by scattering in ray tomography, *Geophysics* **56**: 202–207.
- Wilt, M., Schenkel, C., Torres-Verdin, C., Lee, K. and Tseng, H. (1994). Crosshole for oil field characterization and eor monitoring: Field examples, *64th Annual Internat. Mtg., Soc. Expl. Geophys., Expanded Abstracts*, 1676–1679.
- Wong, J., Bregman, N., West, G. and Hurley, P. (1987). Cross-hole seismic scanning and tomography, *The Leading Edge* **6**(11): 36–41.
- Wong, J., Hurley, P. and West, G. (1983). Crosshole seismology and seismic imaging in crystalline rocks, *Geophys. Res. Lett.* **10**: 686–689.
- Worthington, M. H. (1984). An introduction to geophysical tomography, *First Break* **11**: 20–26.
- Wu, R. and Toksoz, M. N. (1987). Diffraction tomography and multisource holography applied to seismic imaging, *Geophysics* **52**(1): 11–25.
- Zhu, X. and McMechan, G. A. (1988). Acoustic modeling and migration of stacked cross-hole data, *Geophysics* **53**(4): 492–500.

Acknowledgments

First of all I would like to thank my promotor, professor Berkhout, for supervising and directing this research, giving me the freedom to explore, and for teaching me the importance of the "helicopter view". Much thanks also goes to my toegevoegd promotor, Kees Wapenaar, for all the discussions we had, his clear theoretical observations, his scrutinizing way of proof-reading my draft thesis, and for all the cigars.

The crosswell research project was put on its tracks in 1990 by three of my colleagues at TNO Institute of Applied Physics: Len van der Wal, Hugo Vos and Peter-Paul van 't Veen. I want to thank them for all the help. Furthermore, TNO-TPD is greatly acknowledged for sponsoring this research.

In the early years of the project, the crosswell traveltime inversion scheme of Chapter 2 has been developed, which is founded on software written by Berend Scheffers from TNO-IGG. I would like to thank Berend for letting me use his software, and for the pleasant cooperation.

Most of the work has been carried out within the DELPHI consortium project, conducted at the Laboratory of Seismics and Acoustics at Delft University. I want to thank my fellow PhD students, the "Delphi Boys" (including Eric Verschuur), for the time we had together and the fruitful discussions on science, the universe and everything. Furthermore, the members of the DELPHI consortium project are acknowledged for their support. Especially AMOCO is thanked for providing me the synthetic data used in Chapter 4. Thanks also go to Dr. Gouly of Durham University for sending me the field data set used in Chapter 5.

During this research, the constant availability of computing power has always been very important. Therefore, I want to thank the support people for keeping the computers running and for providing the laboratory with the latest and improved software.

I finally have the opportunity to thank all those software developers and institutions that put computer software into the public domain. I am convinced that a lot of researchers in the world benefit from your work. Me included. Thanks for all the good work.

The bottom line is that without Jolien I could not have completed this thesis. You are thanked last, but for me you are the first!

Summary

Seismic methods employ elastic waves to extract information on the subsurface of the earth. In particular, the crosswell seismic method employs seismic sources in one borehole, and detectors in another borehole. Contrary to surface seismic data, crosswell data may contain transmitted waves, and waves reflected from both the top and bottom of interfaces. The prime advantage of crosswell surveying is that frequencies up to several kHz may be used. Therefore, the crosswell seismic method has the potential to resolve details in the order of 1 m, whereas for the surface seismic method the maximum resolution typically is about 20 m.

The objective of this thesis is to develop an improved processing scheme for the transformation of crosswell seismic data into a detailed structural model of the subsurface. A two-step approach is proposed. First, the arrival times of the direct waves are used to estimate a macro velocity model, by means of a travelttime tomography technique. This yields a low resolution image of the subsurface velocity field. Second, using the estimated macro velocity model, the scattered energy is imaged, yielding a detailed structural image of the interwell space.

Classical cell-based crosswell travelttime methods tend to suffer from non-uniqueness due to the fact that the inverse problem is ill-posed. It is shown that the classical approach gives better results when a priori knowledge is used, but the results are still not satisfactory. Therefore, a new approach is presented, by parameterizing the forward model in a geologically oriented way. The actual travelttime tomography step is then implemented as a nonlinear travelttime inversion procedure, using a geometric ray-tracer. To incorporate a priori knowledge, the Bayesian approach is adopted. Examples show that by using a priori knowledge, the method effectively limits the number of parameters that must be estimated, increasing the overall accuracy.

After estimation of the macro velocity model, the scattered wavefield is used to image the detail that is present in the data. A migration approach is taken, which aims at resolving the reflectivity information of the subsurface. At the basis of the newly developed crosswell migration scheme, one-way wave theory is used, which has already successfully been applied to develop a surface seismic migration scheme. Based on one-way theory, a representation for crosswell data is derived. The reflectivity is defined as an intrinsic property of the subsurface and as such it is independent of the acquisition geometry. Using the representation, a migration scheme is

derived to image zero-offset reflectivity. A method to distinguish between reflections from the top and bottom of interfaces is presented. The resolution of the scheme is analyzed. Finally, the typical characteristics of crosswell illumination are addressed.

The method is applied to both synthetic and real data and examples are presented. From the synthetic data examples it can be concluded that accurate images of reflectors can be obtained, with a resolution in the order of 1 m. A comparison is made with a published synthetic data experiment, where a Kirchhoff migration scheme has been used. For this example, the developed migration scheme gives overall comparable results, with some features resolved better than with the Kirchhoff scheme.

A field data set has been processed which has also been processed with a Kirchhoff-type of migration scheme. The Kirchhoff migration results have been published by others. The resolution of the two methods is comparable. The published results do however exhibit more lateral continuity, with the main events all having about the same amplitudes. It is concluded that contrary to synthetic data, for real data the results depend more on the way in which the data is pre-processed and on the way of normalizing the final migrated images.

Samenvatting

Boorgat-naar-boorgat seismische tomografie en migratie

Seismologie heeft als doel het onderzoeken van de geologische structuur en samenstelling van de aarde. Hierbij wordt gebruik gemaakt van elastische golven die zich door de aarde voortplanten. Een belangrijke seismische methode is de "exploratie seismiek", die ondermeer wordt gebruikt voor het zoeken naar en in kaart brengen van gas- en oliereservoirs. Daarbij worden de elastische golven opgewekt door artificiële seismische bronnen, zoals bijvoorbeeld dynamiet. Deze golven kunnen tot enkele kilometers diepte in de aardkorst doordringen. De aanwezigheid van inhomogeniteiten in de ondergrond, zoals gelaagdheid en breuken, zorgt ervoor dat de seismische energie wordt gereflecteerd en verstrooid. Bij oppervlakte seismiek wordt een gedeelte van deze verstrooide golven aan het oppervlak geregistreerd door geofoons (op het land) of hydrofoons (op het water). Hierna worden seismische afbeeldingstechnieken toegepast die uit de gemeten verstrooide golven een *afbeelding* van de aardse ondergrond kunnen reconstrueren.

Bij het afbeelden van seismische signalen correspondeert een hoge signaalfrequentie met een hoge resolutie. Daarom wordt naar een zo hoog mogelijke maximale frequentie in het gedetecteerde signaal gestreefd. Maar wanneer golven zich door een medium voortplanten, treden er in de praktijk altijd signaalverliezen op, doordat het medium de golven verzwakt. Een belangrijke eigenschap van verzwakking is dat hogere frequenties meer worden verzwakt dan lagere frequenties. Tevens is de absolute verzwakking evenredig met de afstand die de golven af moeten leggen. De maximale signaalfrequentie die bij seismische exploratie nog kan worden gebruikt is derhalve ongeveer 100 Hz, waarbij tot enkele kilometers diep een afbeelding wordt verkregen. De maximale resolutie is dan ongeveer 20 m.

Indien er een boorgat in de aarde beschikbaar is, is het mogelijk om seismische bronnen of ontvangers in het boorgat te plaatsen. Als er twee naburige boorgaten aanwezig zijn is het mogelijk om bronnen in het ene boorgat, en ontvangers in het andere boorgat te plaatsen. Dit is de configuratie die "boorgat-naar-boorgat seismiek" wordt genoemd. De seismische golven planten zich nu voort van het ene boorgat naar het andere. De afstand tussen de boorgaten kan enkele tientallen tot enkele honderden meters zijn. Omdat de afstand tussen bronnen en ontvangers in

vergelijking tot de situatie bij oppervlakte seismiek relatief klein is, kunnen er bij boorgat-naar-boorgat seismiek hogere frequenties gebruikt worden. Dit is dan ook het belangrijkste voordeel. In de praktijk worden signaalfrequenties tot enkele kilo-Hertzen gebruikt. Daarom heeft boorgat-naar-boorgat seismiek een potentiële afbeeldingsresolutie van ongeveer 1 m, wat 10-20x beter is dan de resolutie verkregen met oppervlakteseismiek. Boorgat-naar-boorgat seismiek is verder aantrekkelijk omdat het doelgebied, bijvoorbeeld een oliereservoir, van dichtbij "bekeken" kan worden. Ook resulteert de afwijkende configuratie van bronnen en ontvangers (in een verticaal boorgat in plaats van aan het horizontale oppervlak) erin dat andere informatie over de ondergrond kan worden verkregen dan bij oppervlakte seismiek. Wel is, vergeleken met oppervlakte seismiek, de inversie van boorgat-naar-boorgat seismische metingen gecompliceerder omdat er in de data een groter aantal golftypen aanwezig kan zijn.

Doelstelling

Uit boorgat-naar-boorgat seismische metingen is het mogelijk om een afbeelding te maken van de aardse ondergrond nabij de boorgaten. Dit *inverse probleem* is het onderwerp van dit proefschrift. De doelstelling is om een nieuwe en betere manier van afbeelden te ontwikkelen die het mogelijk maakt om hoge resolutie afbeeldingen van de aarde te reconstrueren uit boorgat-naar-boorgat seismische metingen.

Probleembenadering

Aan de ontvangerzijde worden verschillende golftypen geregistreerd. Er is een onderscheid te maken tussen zogenaamde P- en S-golven. In dit proefschrift worden alleen de P-golven beschouwd. De P-golven zijn te decomponeren in directe golven en verstrooide golven. De directe golven hebben qua looptijd het kortst mogelijke pad afgelegd van bron naar ontvanger (het Fermat minimum tijd pad). Zij bevatten voornamelijk informatie over de *transmissie* eigenschappen van het medium. De verstrooide golven kunnen daarentegen gereflecteerd zijn en bevatten dan ook informatie over de *reflectie* eigenschappen van het medium.

Vanwege het onderscheid dat mogelijk is tussen directe en verstrooide golven is in dit proefschrift gekozen voor een probleembenadering in twee stappen:

1. In de eerste stap wordt uit de eerste aankomsttijd van de directe golven, door middel van *looptijd tomografie*, de *trend* van de mediumparameters geschat. Dit levert een model op met een relatief lage resolutie: het *macro snelheidsmodel*.
2. In de tweede stap wordt uit de verstrooide en gereflecteerde golven, door middel van *seismische migratie*, het *detail* afgebeeld. Hierbij wordt het macro snelheidsmodel gebruikt. Migratie beeldt het detail in de ondergrond af in de vorm van *reflectiviteit*.

Looptijd tomografie

Traditionele looptijd tomografie technieken maken gebruik van een parameterisatie bestaande uit een groot aantal "cellen". Uit de gemeten looptijden wordt dan voor elke cel een golfvoortplantingssnelheid geschat. Omdat wordt gestreefd naar een hoge resolutie moeten er kleine cellen worden gebruikt. Het grote aantal parameters leidt er dan toe dat de nauwkeurigheid van de geschatte parameters niet erg groot is.

In dit proefschrift is gekozen voor een andere aanpak. Er wordt niet gestreefd naar het schatten van detail-informatie uit de looptijden, daar dit in een latere migratiestap wordt afgebeeld. In plaats van een cellen model wordt daarom gekozen voor een parameterisatie die meer aansluit op de geologie. Het te onderzoeken medium wordt verdeeld in een aantal gebieden waarvan verondersteld wordt dat ze homogeen zijn. De randen van de gebieden worden geparаметeriseerd met behulp van derde orde polynomen. In de tomografische inversiestap kunnen de golfsnelheden van de gebieden worden afgeschat, en kunnen de steunpunten van de polynomen zich verplaatsen. Voor het berekenen van de looptijden worden geometrische stralen door het model geschoten ("ray-tracing"). Om de schatting nauwkeuriger te maken, wordt gebruik gemaakt van alle mogelijke voorkennis van de ondergrond. Bayesiaanse theorie zorgt ervoor dat de voorkennis op een statistisch verantwoorde manier wordt behandeld. De tomografische inversie is niet-linear en levert een schatting met bijbehorende covariantiematrix, waaruit onder andere voor elke parameter een standaard-deviatie wordt berekend. Met behulp van voorbeelden wordt aangetoond dat de methode nauwkeurigere schattingen kan geven dan de traditionele cellen methode. Een voorbeeld laat zien dat het mogelijk is om de positie van overgangen tussen gebieden met een verschillende golfsnelheid te schatten. De horizontale resolutie blijkt echter relatief slecht te zijn, hetgeen een inherente eigenschap van boorgat-naar-boorgat seismiek is.

Migratie

In het voorwaartse model voor migratie kunnen drie processen onderscheiden worden: propagatie van bronnen naar de ondergrond, reflectie in de ondergrond en propagatie van de ondergrond naar de ontvangers. Seismische migratie houdt in het verwijderen van de beide propagatie-effecten en het afbeelden van de reflectiviteit. Met behulp van één-weg golftheorie is een migratieschema ontwikkeld voor het afbeelden van reflectiviteit uit boorgat-naar-boorgat metingen. De reflectiviteit is gedefinieerd als een intrinsieke eigenschap van het medium, onafhankelijk van de acquisitie geometrie. Bij traditionele, op hoogfrequente stralentheorie gebaseerde migratieschema's (bijvoorbeeld Kirchhoff migratie) is dit niet het geval.

In tegenstelling tot het migratieschema voor oppervlakte seismiek moet bij boorgat-naar-boorgat seismiek een onderscheid worden gemaakt tussen golven die aan de bovenkant en aan de onderkant van een laagovergang reflecteren. Om tot een efficiënt algoritme te komen, wordt de beschrijving van de propagatie benaderd. Het migratie probleem is gesteld als een randvoor-

waardeprobleem, waarbij lokale korte geoptimaliseerde convolutie-operatoren worden gebruikt om op een recursieve manier de propagatie door het medium te berekenen. Op deze manier wordt een efficiënt rekenschema bereikt. Bovendien mag met deze aanpak het medium ook inhomogeen zijn.

Een belangrijk verschil met de situatie bij oppervlakte seismiek is het feit dat de apertuur van de gebruikte bron en ontvanger "arrays" relatief klein is. Dit zorgt ervoor dat zelfs een horizontale reflector in de praktijk maar over een relatief kleine laterale afstand goed belicht kan worden. Om toch tot een structureel juiste interpretatie te kunnen komen, is het noodzakelijk om achteraf te corrigeren voor deze onregelmatige belichting. Het CFP ("Common Focus Point") concept is geïntroduceerd, waarmee een normalisatieproces te definiëren is tijdens het afbeelden, in plaats van na het afbeelden.

Resultaten

Het migratieschema is getest op een representatieve synthetische dataset, gegenereerd met een eindige differentie modellering. De resultaten van de migratie zijn vergeleken met gepubliceerde resultaten, verkregen met een Kirchhoff migratieschema. De conclusie is dat, voor deze dataset, de resultaten van beide schema's van een vergelijkbare kwaliteit zijn. Op enkele punten, zoals de positionering van reflectoren en de laterale resolutie, geeft het nieuw ontwikkelde schema betere resultaten. De behaalde resolutie is ongeveer 1 m.

De complete macromodel schattings- en migratieprocedure is toegepast op een veld-dataset. Deze dataset is geschoten met een relatief klein aantal bronnen en ontvangers. Tijdens het schatten van het macromodel blijkt er een ambiguïteit te bestaan tussen een schatting waarbij de meer verticaal lopende golven zijn gebruikt en de schatting waarbij de meer horizontaal lopende golven zijn gebruikt. Dit duidt op de aanwezigheid van anisotropie. De migratiestap beeldt tenslotte de reflectiviteit af. De resultaten zijn weer vergeleken met reeds gepubliceerde resultaten die met een Kirchhoff migratie zijn verkregen. De resolutie van de twee methoden is vergelijkbaar, maar de gepubliceerde resultaten vertonen een grotere laterale continuïteit. Het is echter niet duidelijk hoe de gepubliceerde resultaten zijn voor- en nabewerkt. Een belangrijke conclusie is dat bij echt gemeten data, de voorbereidingsstap ("pre-processing") een grote rol speelt.

Curriculum vitae

PERSONALIA

Naam : Erwin Johannes Martinus Giling
Geboortedatum : 5 november 1964
Geboorteplaats : Den Burg (Texel)

OPLEIDING

8/77 - 8/83 : VWO-B aan de Rijksscholengemeenschap te Den Burg
9/83 - 8/84 : Studie Elektrotechniek aan de Technische Universiteit Delft
9/84 - 8/90 : Studie Technische Natuurkunde aan de Technische Universiteit Delft

WERKERVARING

9/90 - 4/95 : Wetenschappelijk medewerker/promovendus bij de Technisch
Fysische Dienst TNO TU-Delft
5/95 - heden : Wetenschappelijk medewerker bij de Technisch Fysische Dienst TNO
TU-Delft

